



**POLITECNICO  
DI TORINO**



**САМАРСКИЙ УНИВЕРСИТЕТ**  
SAMARA UNIVERSITY

**Corso di Laurea Magistrale in Ingegneria Aerospaziale**

---

# Optimization of a low pressure compressor stage

**Relatori:**

**Francesco Larocca**

**Evgenii Goryachkin**

**Studente:**

**Salvatore Asaro**

---

**ANNO ACCADEMICO 2017/2018**

## **Abstract**

The purpose of this work is to find a variant of the blade shapes of the axial compressor "Stage 37" that provides an increase in efficiency while maintaining their strength state by joint use of optimization programs and CAE software. Objectives of the work:

1. Creation of a numerical CFD model of the axial compressor "Stage 37" and search for optimal parameters ensuring the best match with the experimental data.
2. Creation of a numerical parametric model of the blades of the axial compressor stage.
3. Joint gas-dynamic and strength optimization of the working process of the axial compressor in order to increase its efficiency.

# Contents

<b>1</b>	<b>Introduction</b>	<b>4</b>
<b>2</b>	<b>Compressor</b>	<b>5</b>
2.1	Aerodynamics . . . . .	6
2.2	Stage pressure ratio . . . . .	7
2.3	Efficiency . . . . .	7
2.4	Surge Margin . . . . .	8
2.5	Nasa Stage 37 . . . . .	8
<b>3</b>	<b>Mesh Generator</b>	<b>10</b>
3.1	Influence of Flow Pass . . . . .	10
3.2	Influence of Blade to Blade . . . . .	13
<b>4</b>	<b>Computational Fluid Dynamics</b>	<b>16</b>
4.1	Fluid model . . . . .	16
4.2	Flow model . . . . .	16
4.2.1	Navier-Stokes Equations . . . . .	16
4.2.2	Time Averaging of Navier-Stokes Equations . . . . .	18
4.2.3	Treatment of Turbulence in the RANS Equations . . . . .	19
4.2.4	Formulation in Rotating Frame for the Relative Velocity . . . . .	20
4.3	Boundary Condition . . . . .	21
4.3.1	Cylindrical Inlet Boundary Conditions . . . . .	21
4.3.2	Outlet Boundary Conditions for Subsonic Flow . . . . .	21
4.3.3	Solid Wall Boundary Conditions - Adiabatic Walls . . . . .	22

4.4	Numerical Model - Discretization and Solution Theory . . . . .	23
4.4.1	Spatial Discretization . . . . .	23
4.4.2	Time Discretization . . . . .	25
4.4.3	Multigrid Strategy . . . . .	26
4.4.4	Full Multigrid Strategy . . . . .	28
4.4.5	Implicit residual smoothing . . . . .	28
4.5	Rotor/Stator Interaction . . . . .	29
4.5.1	Full Non-matching Technique for Mixing Planes . . . . .	29
4.6	Turbulence Models . . . . .	30
4.6.1	Spalart-Allmaras Model . . . . .	31
4.6.2	k- $\epsilon$ Model . . . . .	32
<b>5</b>	<b>Performance Curves</b>	<b>34</b>
5.1	Numeca Fine . . . . .	34
5.2	Performance Curves Comparison . . . . .	36
5.3	Radial distribution . . . . .	40
5.4	Flow Visualization . . . . .	48
5.4.1	Expansion Ratio influence . . . . .	49
5.4.2	Max Aspect Ratio influence . . . . .	55
5.4.3	$y^+$ influence . . . . .	61
5.4.4	Expansion Ratio influence, Blade to Blade . . . . .	69
5.4.5	O layer influence . . . . .	73
5.4.6	Mesh Density influence . . . . .	77
5.4.7	Turbulence Models . . . . .	87
5.4.8	Conclusions . . . . .	94
<b>6</b>	<b>Optimization Projects</b>	<b>95</b>
6.1	Parametric Model . . . . .	95
6.2	Strength on the Rotor Blade . . . . .	107

<b>7 Optimization Process</b>	<b>110</b>
7.1 IOSO program . . . . .	110
7.2 Optimization Results . . . . .	114
7.3 Post optimization considerations . . . . .	120
<b>8 Conclusion</b>	<b>132</b>
<b>Bibliography</b>	<b>133</b>

# Chapter 1

## Introduction

The first step is to compare different mesh configurations, 27 cases are analyzed. The results obtained from the Reynolds averaged Navier Stokes equations are closely related to the meshes, that have great number of elements and complex structure. The results are compared each other through the compressor performance curves, the radial distribution of some variables at working point and the flow visualizations, i.e. Mach, Total Pressure and Turbulent viscosity distribution.

The second step is the creation of a parametric model. Both rotor and stator are built starting from a lower number of sections. It is done to reduce the number of variables through Bezier curves and other approximations. 14 cases are analyzed. The performance curves of all cases are compared each other and with the case obtained in the first step.

The third step is the strength analysis to calculate the constraints that have to be imposed to the last optimization task.

The last step is to create the 6 optimization tasks. The number of degrees of freedom increase moving from the first to the last task. In this way it is possible to see how the degrees of freedom influence the results.

# Chapter 2

## Compressor

Compressor increases the pressure of the fluid. It can be single stage or multistage depending on the application. A stage consists of a stator/rotor combination. A schematic of the blading and the flow processes occurring within an axial flow compressor blade row is shown in Figure 2.1 [1].

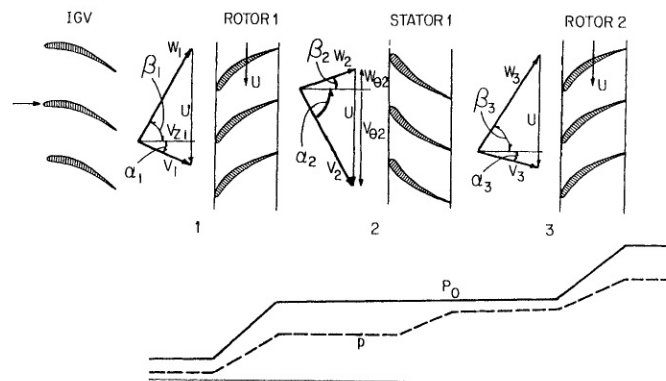


Figure 2.1: Axial flow compressor velocity triangles ( $h_0$  and  $T_0$  distribution are similar to  $P_0$  distribution;  $h$  and  $T$  are similar to  $p$  distribution)

IGV guides air smoothly into a rotor, which is very sensitive to incidence modification or non-uniform velocity. Through the IGV the flow is accelerated and so the static pressure decreases. Rotor blades add energy to the fluid, increasing its stagnation pressure, temperature and kinetic energy. Then the fluid arrive with a proper angle of attack to the stator blades where the static pressure is further increased by flow diffusion. The stagnation pressure is quite the same (except for losses), but static pressure and temperature increase while the kinetic energy decreases. The air

is properly directed to the second-stage rotor, and the process repeats itself. The last stage usually has a guide vane or stator to lead the fluid in the axial direction. Because of changes in velocity, density, pressure, and hub/tip ratio, it is better that all stages do not operate at the same velocity. Therefore, these stages are divided into two segments, the low-pressure compressor and the high-pressure compressor, operating at different speeds.

The characteristic of a compressor is described with its map with shows lines of constant corrected spool speed in the graph pressure ratio over mass flow. This graph is completed by lines with constant efficiency and the surge line [2]:

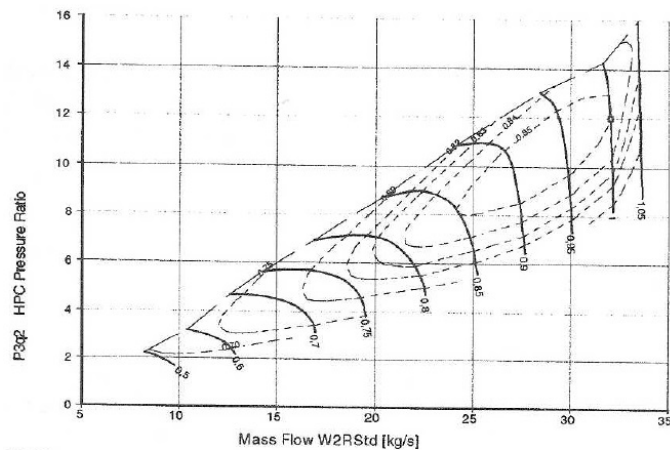


Figure 2.2: Compressor Map

## 2.1 Aerodynamics

For subsonic flow the flow reduces when the throttle downstream is being closed. If the flow is supersonic the speed lines are vertical (constant corrected flow). The peak efficiencies on the supersonic speed lines move towards the surge line, and so it is not possible to operate the compressor where it performs best. When Mach number increases efficiency decreases because shock grow quickly with Mach numbers above 1.3. Also due to the big pressure differences the secondary flows are strengthened and the secondary losses rise significantly.

## 2.2 Stage pressure ratio

The mean stage pressure ratio has been increased mainly by increasing the circumferential speed, only to a minor part by increasing the aerodynamic loading. Consequently blade profiles had to be changed from a subsonic to a transonic design.

On the subsonic blade surface there is nowhere Mach above 1 and such blades are relatively insensitive to incidence.

With a supercritical profiles on the suction side there is a limited supersonic flow region. With a transonic blade the static pressure increases through the gas dynamic shock.

Transonic blade has a low aspect ratio, higher blade width because of the high circumferential speed and it results in high mechanical loading and in heavy disk.

High stage pressure ratios require high solidity (small pitch/chord ratio) because the shocks must be contained within the blade tunnel. If the pitch/cord ratio is not sufficient, the shock is downstream the blade row and the static pressure doesn't increase but only the losses.

## 2.3 Efficiency

The efficiency is dependant on the blade loading and the Mach number level within the compressor. Both increase with stage pressure ratio [3].

$$\psi_{mean} = \frac{c_p * (T_3 - T_2)}{u_{mean}^2 * N_{stages}} \quad (2.1)$$

The stage adiabatic efficiency:

$$\eta_{ad} = \frac{(\overline{P_3/P_1})^{(\gamma-1/\gamma)} - 1}{(\overline{T_3/T_1}) - 1} \quad (2.2)$$

## 2.4 Surge Margin

For any operating condition within the flight envelope sufficient surge margin must remain to guarantee the operability of the engine.

$$\Delta K_y = \left( \frac{\left(\frac{TPR}{G}\right)_{Stall}}{\left(\frac{TPR}{G}\right)_{work}} - 1 \right) \cdot 100\% \quad (2.3)$$

## 2.5 Nasa Stage 37

In the NASA's paper, *Design and Overall Performance of Four Highly Loaded, High-Speed Inlet Stages for an Advanced High-Pressure-Ratio Core Compressor (1978)*, are described the designs and evaluated the overall performances of four single stages that are representative of inlet stage for the advanced-core compressor. These four stages have this design conditions:

Stage	Rotor aspect ratio	Stage pressure ratio
35	1.19	1.82
36	1.63	1.82
37	1.19	2.05
38	1.63	2.05

The stage 37 will be considered in this work.

At design speed the rotor and stage achieved peak efficiencies of 0.876 and 0.840, respectively, at mass flow rate of 20.74 kilograms per second. The rotor and stage pressure ratios at peak efficiency conditions were 2.056 and 2.00, respectively. The mass flow rate at which peak efficiency occurred is about 3 percent higher than the design value. The rotor and stage pressure ratios at design flow rate exceed design values, but the efficiencies were somewhat lower than design. The stall margin at design speed is only 10 percent.

In the paper there are the blades coordinates, respectively 12 and 10 profiles to describe the rotor and the stator. Using the program *Profler* the files for *Numeca*

*IGG-Autogrid5* are created.

In the paper there are also overall performance in a table and the radial distribution of different parameters in graphs, in the latter case the results are extrapolated using the program *Compas*.

# Chapter 3

## Mesh Generator

The purpose of this chapter is to create the mesh files.

The 3D meshes are built stacking 2D blade to blade meshes. For both it is possible to set a certain number of parameters to obtain a coarser or finer grid.

From a monodomain structured approach, three types of grid can be considered:

- An H-grid is suitable to apply far-field and periodicity conditions but is often highly skewed near the leading and trailing edges of the blades.
- A L-grid provides a good resolution around the leading edge and in the wake, but becomes skewed at the inflow and at the periodic boundaries.
- An O-grid allow good resolution of both leading and trailing edges, but induces skewness at inflow outflow and periodic boundaries.

To maintain the advantages and removes the disadvantages a multidomain structured meshes is used [4].

The program used is *Numeca IGG-Autogrid5*.

### 3.1 Influence of Flow Pass

Now they are evaluated the influence of:

- Expansion Ratio, measure of the size variation between two adjacent cells.

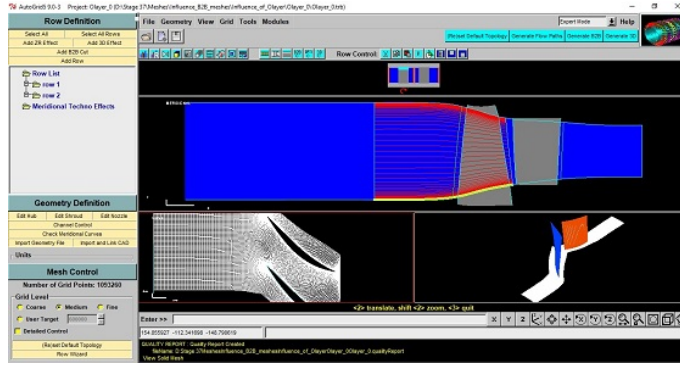


Figure 3.1: Numeca IGG-Autogrid5 - Homepage

- Aspect Ratio, the measure of the cell stretching. The max aspect ratio (MR) is the ratio of the maximum length to the minimum.
- $y^+ = \frac{y u_\tau}{\nu}$ , dimensionless wall distance.  $u_\tau = \sqrt{\tau_w / \rho}$  is the friction velocity. This parameter is changed modifying the value of  $y$ , the width of the first cells.

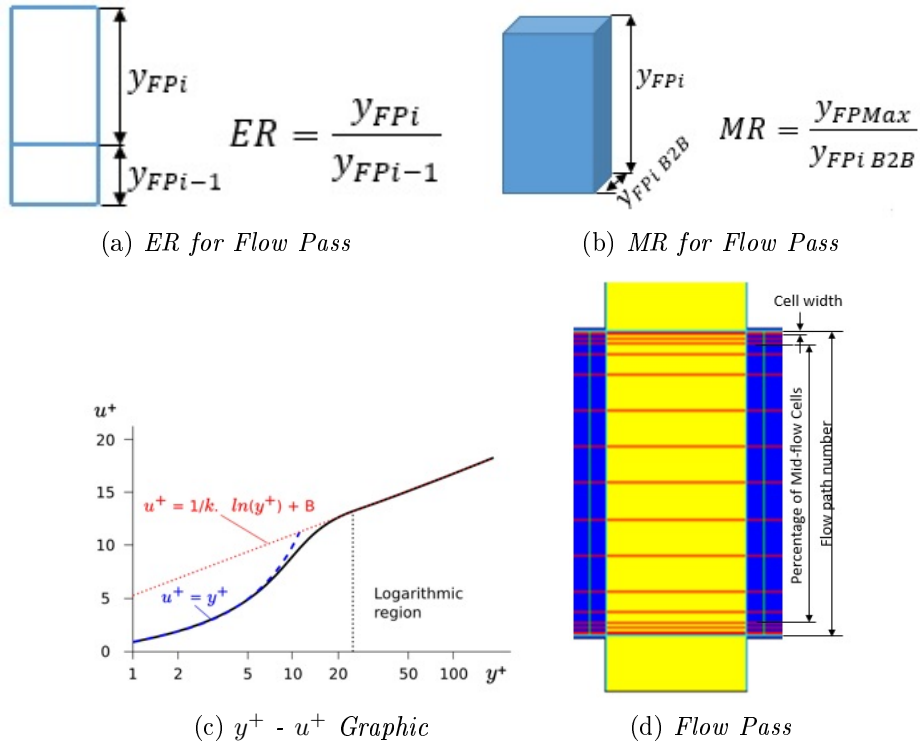


Figure 3.2

Individually the three parameters are evaluated, changing one of them and keeping constant the other two and the distribution in one layer. They can be changed through the percentage of mid-flow and the flow path number.

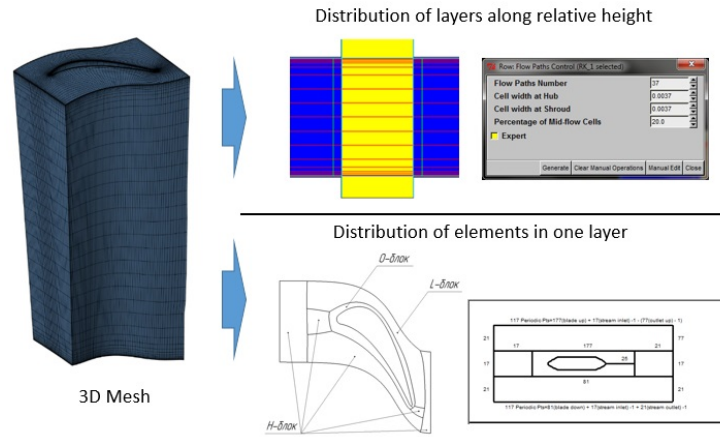


Figure 3.3: 3D Mesh

In tables are reported the 12 meshes considered:

- Influence of ER

Mesh	Pressure S	Suction S	Width1	Width2	Width3	Width1	Width2	Width3	O-layer	Inlet	Outlet	Edge Radi	ER_b2b	MR_FP	ER_FP	y+	Turb	FP	Midle, %	
Mesh_b2b0_ER1.2	53	73	13	17	25	13	17	21	21	21	13	17	1.2	1000	1.2	1	SA	105	11	Rotor
Mesh_b2b0_ER1.4	53	73	13	17	25	13	17	21	21	21	13	17	1.2	1000	1.4	1	SA	77	33	
Mesh_b2b0_ER1.6	53	73	13	17	25	13	17	21	21	21	13	17	1.2	1000	1.6	1	SA	61	40	
Mesh_b2b0_ER1.8	53	73	13	17	25	13	17	21	21	21	13	17	1.2	1000	1.8	1	SA	53	45	
Mesh_b2b0_ER1.2	73	53	13	17	25	9	17	25	21	9	13	17	1.2	1000	1.2	1	SA	89	11	Stator
Mesh_b2b0_ER1.4	73	53	13	17	25	9	17	25	21	9	13	17	1.2	1000	1.4	1	SA	77	13	
Mesh_b2b0_ER1.6	73	53	13	17	25	9	17	25	21	9	13	17	1.2	1000	1.6	1	SA	45	37	
Mesh_b2b0_ER1.8	73	53	13	17	25	9	17	25	21	9	13	17	1.2	1000	1.8	1	SA	41	45	

Figure 3.4: Influence of ER

- Influence of MR

Mesh	Pressure S	Suction S	Width1	Width2	Width3	Width1	Width2	Width3	O-layer	Inlet	Outlet	Edge Radi	ER_b2b	MR_FP	ER_FP	y+	Turb	FP	Midle, %	
Mesh_b2b0_MR1000	53	73	13	17	25	13	17	21	21	21	13	17	1.2	1000	1.2	1	SA	105	11	Rotor
Mesh_b2b0_MR500	53	73	13	17	25	13	17	21	21	21	13	17	1.2	500	1.2	1	SA	121	28	
Mesh_b2b0_MR200	53	73	13	17	25	13	17	21	21	21	13	17	1.2	200	1.2	1	SA	129	40	
Mesh_b2b0_MR2000	53	73	13	17	25	13	17	21	21	21	13	17	1.2	2000	1.2	1	SA	77	4	
Mesh_b2b0_MR1000	73	53	13	17	25	9	17	25	21	9	13	17	1.2	1000	1.2	1	SA	89	11	Stator
Mesh_b2b0_MR500	73	53	13	17	25	9	17	25	21	9	13	17	1.2	500	1.2	1	SA	101	30	
Mesh_b2b0_MR200	73	53	13	17	25	9	17	25	21	9	13	17	1.2	200	1.2	1	SA	121	45	
Mesh_b2b0_MR2000	73	53	13	17	25	9	17	25	21	9	13	17	1.2	2000	1.2	1	SA	53	4	

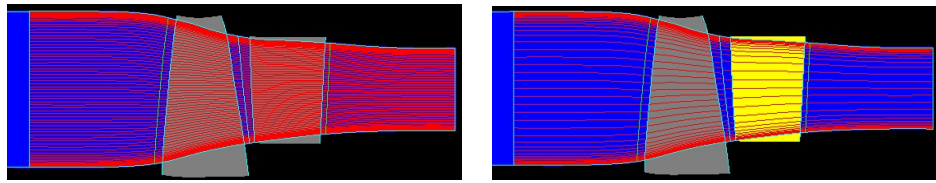
Figure 3.5: Influence of MR

- Influence of  $y^+$

Mesh	Pressure	Suction S	Width1	Width2	Width3	Width1	Width2	Width3	O-layer	Inlet	Outlet	Edge Radi	ER_b2b	MR_FP	ER_FP	y+	Turb	FP	Midle, %		
Mesh_b2b0_y1	53	73	13	17	25	13	17	21	21	21	13	17	1.2	1000	1.2	1	SA		105	15	Rotor
Mesh_b2b0_y3	53	73	13	17	25	13	17	21	21	21	13	17	1.2	1000	1.2	3	SA		97	22	
Mesh_b2b0_y7	53	73	13	17	25	13	17	21	21	21	13	17	1.2	1000	1.2	7	SA		93	17	
Mesh_b2b0_y05	53	73	13	17	25	13	17	21	21	21	13	17	1.2	1000	1.2	0.5	SA		105	20	
Mesh	Suction S	Pressure S	Width1	Width2	Width3	Width1	Width2	Width3	O-layer	Inlet	Outlet	Edge Radi	ER_b2b	MR_FP	ER_FP	y+	Turb	FP	Midle, %		
Mesh_b2b0_y1	73	53	13	17	25	9	17	25	21	9	13	17	1.2	1000	1.2	1	SA		89	6	Stator
Mesh_b2b0_y3	73	53	13	17	25	9	17	25	21	9	13	17	1.2	1000	1.2	3	SA		57	18	
Mesh_b2b0_y7	73	53	13	17	25	9	17	25	21	9	13	17	1.2	1000	1.2	7	SA		53	14	
Mesh_b2b0_y05	73	53	13	17	25	9	17	25	21	9	13	17	1.2	1000	1.2	0.5	SA		89	11	

Figure 3.6: Influence of  $y^+$

In Figure (3.7) there are two examples, on the left Mesh b2b0 MR200, on the right Mesh b2b0 y7.

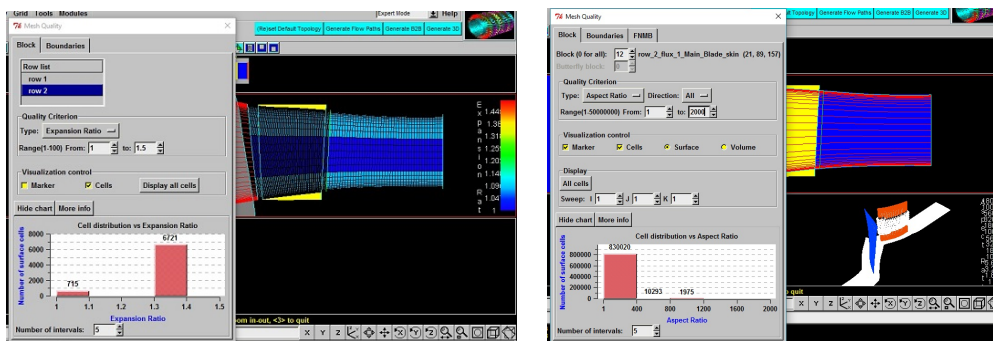


(a) Mesh b2b0 MR200

(b) Mesh b2b0 y7

Figure 3.7

The ER and MR values are checked to verified the values of the three variables imposed for each mesh, Figure (3.8).



(a) ER checking

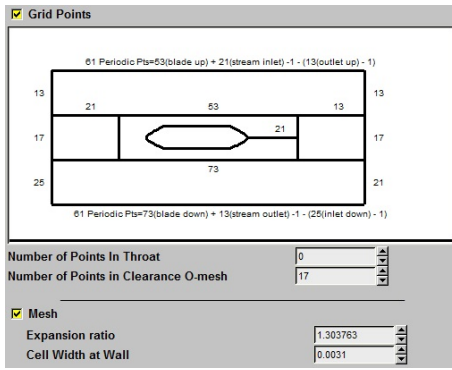
(b) MR checking

Figure 3.8

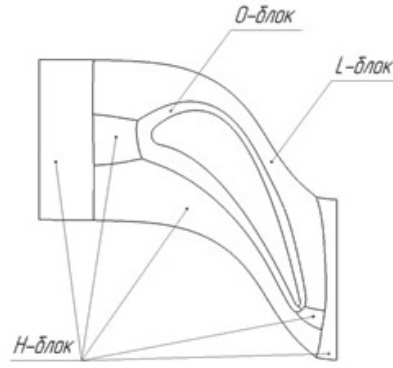
## 3.2 Influence of Blade to Blade

Now the Flow Pass variables are kept constant and it is studied the influence of:

- Influence of Expansion Ratio.
- Influence of O-layer, number of elements in O-block.
- Influence of mesh density, number of elements in L- and H-blocks.



(a) Blade to Blade Meshes



(b) Three blocks

Figure 3.9

In tables are reported the 15 meshes considered:

- Influence of ER

	Pressure Sid	Suction Side	Width1	Width2	Width3	Width1	Width2	Width3	O-layer	Inlet	Outlet	Edge Radius	ER_b2b	MR_FP	ER_FP	y+	Turb	FP	Midie, %	
Mesh_b2b0_ER_b2b1.2	73	53	13	17	25	21	17	13	21	21	13	17	1.2	1000	1.2	1	SA	105	11	Rotor
Mesh_b2b0_ER_b2b1.1	73	53	13	17	25	21	17	13	21	21	13	17	1.1	1000	1.2	1	SA	105	11	
Mesh_b2b0_ER_b2b1.3	73	53	13	17	25	21	17	13	21	21	13	17	1.3	1000	1.2	1	SA	105	11	
Mesh_b2b0_ER_b2b1.4	73	53	13	17	25	21	17	13	21	21	13	17	1.4	1000	1.2	1	SA	105	11	
Mesh_b2b0_ER_b2b1.2	73	53	13	17	25	9	17	25	21	9	13	17	1.2	1000	1.2	1	SA	89	11	Stator
Mesh_b2b0_ER_b2b1.1	73	53	13	17	25	9	17	25	21	9	13	17	1.1	1000	1.2	1	SA	89	11	
Mesh_b2b0_ER_b2b1.3	73	53	13	17	25	9	17	25	21	9	13	17	1.3	1000	1.2	1	SA	89	11	
Mesh_b2b0_ER_b2b1.4	73	53	13	17	25	9	17	25	21	9	13	17	1.4	1000	1.2	1	SA	89	11	

Figure 3.10: Influence of ER

- Influence of O-layer

Mesh	Pressure Sid	Suction Side	Width1	Width2	Width3	Width1	Width2	Width3	O-layer	Inlet	Outlet	Edge Radius	ER_b2b	MR_FP	ER_FP	y+	Turb	FP	Midie, %		
Mesh_b2b0_O_0	53	73	13	17	25	13	17	25	21	21	21	13	17	1.2	1000	1.2	1	SA	105	11	Rotor
Mesh_b2b0_O_-1	53	73	13	17	25	13	17	25	21	17	21	13	17	1.2	1000	1.2	1	SA	105	11	
Mesh_b2b0_O_-2	53	73	13	17	25	13	17	25	21	13	21	13	17	1.2	1000	1.2	1	SA	105	11	
Mesh_b2b0_O_1	53	73	13	17	25	13	17	25	21	25	21	13	17	1.2	1000	1.2	1	SA	105	11	
Mesh_b2b0_O_2	53	73	13	17	25	13	17	25	21	29	21	13	17	1.2	1000	1.2	1	SA	105	11	
Mesh_b2b0_O_0	73	53	13	17	25	9	17	25	21	9	13	17	1.2	1000	1.2	1	SA	89	11	Stator	
Mesh_b2b0_O_-1	73	53	13	17	25	9	17	25	17	9	13	17	1.2	1000	1.2	1	SA	89	11		
Mesh_b2b0_O_-2	73	53	13	17	25	9	17	25	13	9	13	17	1.2	1000	1.2	1	SA	89	11		
Mesh_b2b0_O_1	73	53	13	17	25	9	17	25	25	9	13	17	1.2	1000	1.2	1	SA	89	11		
Mesh_b2b0_O_1	73	53	13	17	25	9	17	25	29	9	13	17	1.2	1000	1.2	1	SA	89	11		

Figure 3.11: Influence of O-layer

- Influence of mesh density

Mesh	Pressure Side	Suction Side	Width1	Width2	Width3	Width1	Width2	Width3	O-layer	Inlet	Outlet	Edge Radius	ER_b2b	MR_FP	ER_FP	y+	Turb	FP	Midle.%	
Mesh_b2b-1	41	57	9	17	17	9	17	17	21	17	9	17	1.2	1000	1.2	1	SA	105	11	Rotor
Mesh_b2b0	53	73	13	17	25	13	17	21	21	21	13	17	1.2	1000	1.2	1	SA	105	11	
Mesh_b2b1	89	109	21	25	37	25	25	29	21	29	21	25	1.2	1000	1.2	1	SA	105	11	
Mesh_b2b2	137	165	29	33	49	33	33	41	21	41	29	33	1.2	1000	1.2	1	SA	105	11	
Mesh_b2b3	197	249	41	41	73	41	41	61	21	61	41	41	1.2	1000	1.2	1	SA	105	11	
Mesh_b2b4	289	373	61	57	109	57	57	93	21	93	61	57	1.2	1000	1.2	1	SA	105	11	
Mesh	Suction Side	Pressure Side	Width1	Width2	Width3	Width1	Width2	Width3	O-layer	Inlet	Outlet	Edge Radius	ER_b2b	MR_FP	ER_FP	y+	Turb	FP	Midle.%	
Mesh_b2b-1	57	41	9	17	17	9	17	17	21	9	13	17	1.2	1000	1.2	1	SA	89	11	Stator
Mesh_b2b0	73	53	13	17	25	13	17	25	21	9	13	17	1.2	1000	1.2	1	SA	89	11	
Mesh_b2b1	109	77	21	25	29	13	25	29	21	13	17	25	1.2	1000	1.2	1	SA	89	11	
Mesh_b2b2	165	105	33	33	33	29	33	33	21	29	29	33	1.2	1000	1.2	1	SA	89	11	
Mesh_b2b3	249	165	49	41	41	37	41	41	21	37	41	41	1.2	1000	1.2	1	SA	89	11	
Mesh_b2b4	373	245	73	57	61	57	57	61	21	57	61	57	1.2	1000	1.2	1	SA	89	11	

Figure 3.12: Influence of mesh density

# Chapter 4

## Computational Fluid Dynamics

The scope of this chapter is to calculate maps of compressor for each meshes, to compare each other and with experimental data and to choose the best one.

### 4.1 Fluid model

A real gas is considered or more precisely a thermally perfect gases, in which  $c_P$  and  $\gamma$  depend on temperature. This model is based on two equation: perfect gas model and enthalpy equation. Considering a specified constant gas R it is possible to calculate  $c_P$  and  $\gamma$ . Also the dynamic viscosity and the heat conductivity depend on temperature [5].

### 4.2 Flow model

A steady time configuration is used for all the analyses.

#### 4.2.1 Navier-Stokes Equations

The set of equation used are the Navier-Stokes equations, in a Cartesian frame:

$$\frac{\partial}{\partial t} \int_{\Omega} U d\Omega + \int_S \vec{F}_I \cdot d\vec{S} + \int_S \vec{F}_V \cdot d\vec{S} = \int_{\Omega} S_T d\Omega \quad (4.1)$$

where  $\Omega$  is the volume,  $S$  is the surface,  $U$  is the vector of the conservative variables,  $\vec{F}_I$  and  $\vec{F}_V$  are the inviscid and viscous flux vectors:

$$U = \begin{bmatrix} \rho \\ \rho v_1 \\ \rho v_2 \\ \rho v_3 \\ \rho E \end{bmatrix}, \quad \vec{F}_I = \begin{bmatrix} \rho v_i \\ \rho v_1 v_i + p \delta_{1i} \\ \rho v_2 v_i + p \delta_{2i} \\ \rho v_3 v_i + p \delta_{3i} \\ \rho(\rho E + p)v_i \end{bmatrix}, \quad -\vec{F}_V = \begin{bmatrix} 0 \\ \tau_{i1} \\ \tau_{i2} \\ \tau_{i3} \\ q_i + v_j \tau_{ij} \end{bmatrix}$$

where the total energy and the heat flux components are defined as:

$$E = e + \frac{1}{2}v_i v_j, \quad q_i = k \frac{\partial T}{\partial x_i} \quad (4.2)$$

$k$  is the laminar thermal conductivity.

In  $S_T$  there are the source terms:

$$S_T = \begin{bmatrix} 0 \\ \rho f_{e1} \\ \rho f_{e2} \\ \rho f_{e3} \\ W_f \end{bmatrix}$$

where the external forces have components  $f_{e1}$ ,  $f_{e2}$  and  $f_{e3}$ .

To close the system, it is necessary to specify the constitutive laws and the definition of the shear stress tensor in function of the other variables. For Newtonian fluids, the shear stress tensor is given by:

$$\tau_{ij} = \mu \left[ \left( \frac{\partial v_j}{\partial x_i} + \frac{\partial v_i}{\partial x_j} \right) - \frac{2}{3} \left( \vec{\nabla} \cdot \vec{v} \right) \delta_{ij} \right] \quad (4.3)$$

where  $\mu$  is the dynamic molecular viscosity [6].

## 4.2.2 Time Averaging of Navier-Stokes Equations

The Navier-Stokes equations describe both laminar and turbulent flows. However, turbulence is a nonlinear process with a wide range of spatial and temporal scales. The direct simulation of complex turbulent flows in most engineering applications is not possible. Averaged Navier-Stokes (RANS) equations are obtained by averaging the viscous conservation laws over a time interval  $T$ , large enough with respect to all other time scales of the turbulent fluctuations, but small enough with respect to all other time-dependent effects.

The quantity  $A$  in the Navier-Stokes equations is time averaged related to the instantaneous value through [7]:

$$A = \bar{A} + A' \quad (4.4)$$

where the time averaged value is

$$\bar{A}(\vec{x}, t) = \frac{1}{T} \int_{-T/2}^{T/2} A(\vec{x}, t + \tau) d\tau \quad (4.5)$$

and the fluctuating part  $A'$ , for which  $\overline{A'} = 0$ .

The corresponding density weighted average is defined through:

$$\tilde{A} = \frac{\overline{\rho A}}{\bar{\rho}} \quad (4.6)$$

with

$$A = \tilde{A} + A'', \quad \overline{\rho A''} = 0 \quad (4.7)$$

Density and pressure are time averaged, whereas energy, velocity components and temperature are density weighted time averaged.

The averaged form of the Navier-Stokes equations is the same as the previous one,

but with:

$$U = \begin{bmatrix} \bar{\rho} \\ \bar{\rho}\tilde{v}_1 \\ \bar{\rho}\tilde{v}_2 \\ \bar{\rho}\tilde{v}_3 \\ \bar{\rho}\tilde{E} \end{bmatrix}, \quad \vec{F}_I = \begin{bmatrix} \bar{\rho}\tilde{v}_i \\ \bar{\rho}\tilde{v}_1\tilde{v}_i + \overline{\rho v_1'' v_i''} + \bar{p}\delta_{1i} \\ \bar{\rho}\tilde{v}_2\tilde{v}_i + \overline{\rho v_2'' v_i''} + \bar{p}\delta_{2i} \\ \bar{\rho}\tilde{v}_3\tilde{v}_i + \overline{\rho v_3'' v_i''} + \bar{p}\delta_{3i} \\ (\bar{\rho}\tilde{E} + \bar{p})\tilde{v}_i + \overline{\rho E'' v_i''} + \overline{p v_i''} \end{bmatrix}, \quad -\vec{F}_V = \begin{bmatrix} 0 \\ \bar{\tau}_{i1} \\ \bar{\tau}_{i2} \\ \bar{\tau}_{i3} \\ \bar{q}_i + \overline{v_i \tau_{ij}} \end{bmatrix}$$

where the density averaged total energy is given by:

$$\tilde{E} = \tilde{e} \left| \frac{1}{2} \tilde{v}_i \tilde{v}_i \right| k \quad (4.8)$$

$k$  the turbulent kinetic energy is defined:

$$k = \frac{1}{2} (\overline{\rho v_i'' v_i''} / \bar{\rho}) \quad (4.9)$$

### 4.2.3 Treatment of Turbulence in the RANS Equations

This process leads to the introduction of the Reynolds stress tensor and turbulent heat diffusion term, they have to be modeled to close the system. The Reynolds stress tensor is the correlation between the components of the fluctuating velocities, it appears as an additional fictitious stress tensor and it can be interpreted as a volumetric force on the mean flow.

For the linear eddy viscosity turbulence models, a first-order closure model, based on Boussinesq's assumption, is used for the Reynolds stress. This hypothesis involves that the Reynolds-stress-anisotropy tensor is linearly related to the mean rate of strain tensor, via the turbulent eddy viscosity  $\mu_T$  has not general validity [8].

$$-\overline{\rho v_i'' v_j''} = \mu_T \left[ \frac{\partial \tilde{v}_i}{\partial x_j} + \frac{\partial \tilde{v}_j}{\partial x_i} - \frac{2}{3} \left( \vec{\nabla} \cdot \vec{v} \right) \delta_{ij} \right] - \frac{2}{3} \bar{\rho} \tilde{k} \delta_{ij} \quad (4.10)$$

For the turbulent heat diffusion term, a gradient approximation is used,

$$C_P \overline{\rho v_i'' T} = -k_T \frac{\partial \tilde{T}}{\partial x_i} \quad (4.11)$$

where  $k_T$  is the turbulent thermal conductivity and is connected to  $\mu_T$  through a turbulent Prandtl number  $Pr_T$ ,  $k_T = \frac{\mu_T C_P}{Pr_T}$ . The resulting system of governing equations with the assumptions above is the same as previous one, with:

$$U = \begin{bmatrix} \bar{\rho} \\ \bar{\rho} \tilde{v}_1 \\ \bar{\rho} \tilde{v}_2 \\ \bar{\rho} \tilde{v}_3 \\ \bar{\rho} \tilde{E} \end{bmatrix}, \quad \vec{F}_I = \begin{bmatrix} \bar{\rho} \tilde{v}_i \\ \bar{\rho} \tilde{v}_1 \tilde{v}_i + \bar{p}^* \delta_{1i} \\ \bar{\rho} \tilde{v}_2 \tilde{v}_i + \bar{p}^* \delta_{2i} \\ \bar{\rho} \tilde{v}_3 \tilde{v}_i + \bar{p}^* \delta_{3i} \\ (\bar{\rho} \tilde{E} + \bar{p}^*) \tilde{v}_i \end{bmatrix}, \quad -\vec{F}_V = \begin{bmatrix} 0 \\ \bar{\tau}_{i1} \\ \bar{\tau}_{i2} \\ \bar{\tau}_{i3} \\ \bar{q}_i + \tilde{v}_i \bar{\tau}_{ij} \end{bmatrix}$$

where the Reynolds stress and the heat flux components are given by:

$$\bar{\tau}_{ij} = (\mu + \mu_T) \left[ \frac{\partial \tilde{v}_i}{\partial x_j} + \frac{\partial \tilde{v}_j}{\partial x_i} - \frac{2}{3} \left( \vec{\nabla} \cdot \vec{v} \right) \delta_{ij} \right], \quad \bar{q}_i = (\bar{k} + k_t) \frac{\partial \tilde{T}}{\partial x_i} \quad (4.12)$$

$\mu_T$  and  $k_T$  have to be solved by the turbulence models.

The static pressure and the total energy contain contributions from the turbulent kinetic energy  $k$  and are defined as:

$$\bar{p}^* = \bar{p} + \frac{2}{3} \bar{\rho} \tilde{k}, \quad \tilde{E} = \tilde{e} + \frac{1}{2} \tilde{v}_i \tilde{v}_i + \tilde{k} \quad (4.13)$$

#### 4.2.4 Formulation in Rotating Frame for the Relative Velocity

In turbomachinery problem is necessary to describe the flow behaviour in the relative system and solve the governing equations for the relative velocity components. In

this case, with  $w_i$  the  $x_i$  component of the relative velocity  $\vec{w}$ :

$$U = \begin{bmatrix} \bar{\rho} \\ \bar{\rho}\tilde{w}_1 \\ \bar{\rho}\tilde{w}_2 \\ \bar{\rho}\tilde{w}_3 \\ \bar{\rho}\tilde{E} \end{bmatrix}, \quad \vec{F}_I = \begin{bmatrix} \bar{\rho}\tilde{w}_i \\ \bar{\rho}\tilde{w}_1\tilde{w}_i + \bar{p}^*\delta_{1i} \\ \bar{\rho}\tilde{w}_2\tilde{w}_i + \bar{p}^*\delta_{2i} \\ \bar{\rho}\tilde{w}_3\tilde{w}_i + \bar{p}^*\delta_{3i} \\ (\bar{\rho}\tilde{E} + \bar{p}^*)\tilde{w}_i \end{bmatrix}, \quad -\vec{F}_V = \begin{bmatrix} 0 \\ \bar{\tau}_{i1} \\ \bar{\tau}_{i2} \\ \bar{\tau}_{i3} \\ \bar{q}_i + \tilde{w}_i\bar{\tau}_{ij} \end{bmatrix}$$

The source term vector  $S_T$  contains contributions of Coriolis and centrifugal forces and is given by:

$$S_T = \begin{bmatrix} 0 \\ (-\bar{\rho})[2\vec{\omega}x\vec{w} + (\vec{\omega}x(\vec{\omega})x\vec{r})] \\ \bar{\rho}\vec{w} \cdot \vec{\nabla}(0.5\omega^2r^2) \end{bmatrix}$$

with  $\omega$  the angular velocity of the relative frame of reference [9].

## 4.3 Boundary Condition

### 4.3.1 Cylindrical Inlet Boundary Conditions

Total quantities are imposed, supersonic case. It is possible to set total pressure ( $p^0 = 101325$  Pa), absolute total temperature ( $T^0 = 288.15$  K), absolute Mach number. The orientation of the velocity is set to be normal to the inlet surface. [10]

### 4.3.2 Outlet Boundary Conditions for Subsonic Flow

It is possible to impose one of the two following conditions:

- **Pressure imposed**

The static pressure at the outlet boundary is specified. In the standard cases the following pressure are set to the design point and the first six performance curve points (9000, 110000, 130000, 140000, 150000, 160000, 1650000 Pa).

The remaining dependent variables on the outlet boundary are obtained from

the interior field through extrapolation. The backflow control checks the total temperature distribution along the exit boundary. In case the flow partially re-enters the domain, its total temperature is controlled so that the entering and outgoing flow globally have the same total temperature [11].

300 iterations are used with converge criteria equal to -6.0.

- **Mass Flow imposed**

This option is used to calculate point near stall because there is not increase in pressure ratio in this region. The mass flow usually set is 19.5 *kg/s* and the initial pressure is equal to the previous point.

The mass flow is fixed at a given control surface by scaling the velocity vector on this surface. As in the pressure imposed case, the other parameters are calculated from the interior field, also pressure so it is imperative that the inlet boundary condition fixes the pressure through the total pressure.

Fixing the mass flow is not as robust as to impose the pressure and this is particularly sensitive with full-multigrid. An initial pressure has to be imposed during the full-multigrid process. Consequently, the mass flow computed at outlet is not exactly the target mass flow during the computation on the coarse grids [12].

3000 iterations are used with converge criteria equal to -6.0.

### 4.3.3 Solid Wall Boundary Conditions - Adiabatic Walls

The velocity vector on the wall vanishes. The angular velocity of the wall (in the absolute frame of reference) has to be specified. For rotor it is 17185 rpm, obviously zero for stator.

The velocity relative to the wall should be zero, leading to:  $\vec{w} = -(\vec{u}_{system} - \vec{u}_{wall})$   
 Projecting the momentum equation onto the wall normal direction  $\vec{n}$ , a relation for pressure is obtained, in the absolute reference frame:

$$\vec{n} \cdot \vec{\nabla} p = -\rho \vec{n} \cdot (\vec{v} \cdot \vec{\nabla}) \vec{v} + \vec{n} \cdot (\vec{\nabla} \cdot \tau) \quad (4.14)$$

The normal pressure gradient can be expressed as a function of pressure derivatives along the coordinates lines:

$$\vec{n} \cdot \vec{\nabla} p = \frac{1}{|\vec{S}_j| \Omega} \left[ \vec{S}_j \cdot \vec{S}_i \frac{\partial p}{\partial \xi} + \vec{S}_j \cdot \vec{S}_j \frac{\partial p}{\partial \eta} + \vec{S}_j \cdot \vec{S}_k \frac{\partial p}{\partial \zeta} \right] \quad (4.15)$$

where  $\xi$ ,  $\eta$ ,  $\zeta$  are the coordinates in the i, j and k directions, it is assumed that j-direction is directed away from the wall (not necessarily perpendicular).  $\vec{S}_{i,j,k}$  are the surface vectors of the corresponding cell faces.

Once  $\partial p / \partial \eta$  is found, the pressure on the wall is:  $p_w = p_1 - \frac{\partial p}{\partial \eta}$  assuming the direction points inside the interior field.  $w$  indicates the wall, 1 the first inner cell [13].

## 4.4 Numerical Model - Discretization and Solution Theory

### 4.4.1 Spatial Discretization

A cell centered control volume approach is used. The general Navier Stokes equation is discretised as:

$$\int_{\Omega} \frac{\partial U}{\partial t} d\Omega + \sum_{faces} \vec{F}_I \cdot \Delta \vec{S} + \sum_{faces} \vec{F}_V \cdot \Delta \vec{S} = \int_{\Omega} S_T d\Omega \quad (4.16)$$

$\vec{F}_I \cdot \Delta \vec{S}$  is the inviscid fluxes and  $\vec{F}_V \cdot \Delta \vec{S}$  the viscous fluxes.

- **Viscous Fluxes**

They are determined in a purely central way. Gradients must be evaluated on the cell faces, this is done applying Gauss theorem[14]:

$$\vec{\nabla} \Phi = \frac{1}{\Omega} \int \vec{\nabla} \Phi d\Omega = \frac{1}{\Omega} \int \Phi d\vec{S} \quad (4.17)$$

- **Inviscid Fluxes**

They are upwind based numerical fluxes, and therefore noted with a \* superscript, expressed as Hirsch (1990) [15]:

$$(\vec{F}\vec{n})_{i+1/2}^* = \frac{1}{2} \left[ (\vec{F}\vec{n})_i + (\vec{F}\vec{n})_{i+1} \right] - d_{i+1/2} \quad (4.18)$$

the term in square brackets is a central evaluation of the flux. The term  $d_{i+1/2}$  represent a numerical dissipation term, it is an artificial dissipation used in combination with central schemes.

In the equation above a flux can be used, based on the averaged unknowns instead of averaging the fluxes:

$$(\vec{F}\vec{n})_{i+1/2}^* = \vec{F}\vec{n} \left( \frac{U_i + U_{i+1}}{2} \right) - d_{i+1/2} \quad (4.19)$$

Using the central scheme this formulation is more robust, especially for high speed flows.

For central schemes a Jameson type dissipation is used with 2nd and 4nd order derivatives of the conservative variables:

$$d_{i+1/2} = \epsilon_{i+1/2}^{(2)} \delta U_{i+1/2} + \epsilon_i^{(4)} \delta^3 U_{i+1} \quad (4.20)$$

The scalar coefficients  $\epsilon$  are:

$$\epsilon_{i+1/2}^{(2)} = \frac{1}{2} \kappa^{(2)} \lambda^* \max(\nu_{i-1}, \nu_i, \nu_{i+1}, \nu_{i+2}), \quad \epsilon_{i+1/2}^{(4)} = \max(0, \frac{1}{2} \kappa^{(4)} \lambda^* - \epsilon_{i+1/2}^{(2)}) \quad (4.21)$$

The coefficient  $\kappa^{(2)}$  and  $\kappa^{(4)}$  are user input.

The cell centered values of  $\epsilon^{(4)}$  are obtained by arithmetic averaging of the cell face values of scalar coefficient  $\epsilon$ . The  $\nu_i$  activate a second-difference dissipation in region of strong gradients, such as shocks. They are based on pressure and

temperature variations:

$$\nu_i = \max \left\{ \left| \frac{p_{i+1} - 2p_i + p_{i-1}}{p_{i+1} + 2p_i + p_{i-1}} \right|, \left| \frac{T_{i+1} - 2T_i + T_{i-1}}{T_{i+1} + 2T_i + T_{i-1}} \right| \right\} \quad (4.22)$$

For the  $k$  and  $\epsilon$  equations,  $\nu_i$  are based on the pressure, the turbulent kinetic energy and the dissipation rate:

$$\nu_i = \max \left\{ \left| \frac{p_{i+1} - 2p_i + p_{i-1}}{p_{i+1} + 2p_i + p_{i-1}} \right|, \left| \frac{k_{i+1} - 2k_i + k_{i-1}}{k_{i+1} + 2k_i + k_{i-1}} \right|, \left| \frac{\epsilon_{i+1} - 2\epsilon_i + \epsilon_{i-1}}{\epsilon_{i+1} + 2\epsilon_i + \epsilon_{i-1}} \right| \right\} \quad (4.23)$$

$\lambda^*$  in the scalar coefficients  $\epsilon$  equations is a measure of the inviscid fluxes and it is chosen as the spectral radius multiplied with the cell face area:

$$\lambda^* = \lambda_{i+1/2}^* = (\vec{v} \cdot \Delta \vec{S} + c\Delta S)_{i+1/2} \quad (4.24)$$

#### 4.4.2 Time Discretization

A separate space and time method is used to solve the Navier-Stokes equations. The time integration is performed using a Runge-Kutta approach. An explicit q-stage Runge-Kutta scheme for the equation  $\frac{dU}{dt} = F(U)$  can be written:

$$U^1 = U^n + \alpha_1 \Delta t F(U^n), U^2 = U^n + \alpha_2 \Delta t F(U^1), \dots, U^q = U^n + \Delta t F(U^{q-1}), U^{n+1} = U^q \quad (4.25)$$

$U^n$  is the value of  $U$  at the time step  $t$  and  $U^{n+1}$  at the time step  $t + \Delta t$ . The coefficients  $\alpha_i$  determine the stability area and the order of accuracy of the Runge-Kutta scheme. Usually 4 or 5 stage Runge-Kutta schemes are used, for central schemes:

1.  $\alpha_1 = 0.125, \alpha_2 = 0.306, \alpha_3 = 0.587, \alpha_4 = 1.$
2.  $\alpha_1 = 0.814, \alpha_2 = 0.191, \alpha_3 = 0.342, \alpha_4 = 0.574, \alpha_5 = 1.$

For inviscid calculation the local inviscid time step (i.e. for each cell) is determined as:

$$\left(\frac{\Delta t}{\Omega}\right)_I = \frac{C_I}{|\vec{w}\vec{S}_i| + |\vec{w}\vec{S}_j| + |\vec{w}\vec{S}_k| + c \left[ |\vec{S}_i| + |\vec{S}_j| + |\vec{S}_k| \right]} \quad (4.26)$$

$C_I$  is the CFL number (it is set equal to 3). The vectors  $S$  are cell normals at the cell center (obtained by averaging the normals on the cell faces). The module indicates the cell face area.

For viscous calculations a local viscous time step in each cell is calculated:

$$\left(\frac{\Delta t}{\Omega}\right)_\nu = \frac{C_V \Omega \rho}{8\mu \left[ |\vec{S}_i|^2 + |\vec{S}_j|^2 + |\vec{S}_k|^2 + 2(|\vec{S}_i\vec{S}_j| + |\vec{S}_i\vec{S}_k| + |\vec{S}_k\vec{S}_j|) \right]} \quad (4.27)$$

$\mu$  is the sum of local laminar and turbulent viscosity. By default  $C_V = -1$  and it is replaced by  $C_I$ . The local time step is obtained by weighting the inviscid and viscous time step:

$$\left(\frac{\Delta t}{\Omega}\right) = \frac{\left(\frac{\Delta t}{\Omega}\right)_I \left(\frac{\Delta t}{\Omega}\right)_\nu}{\left(\frac{\Delta t}{\Omega}\right)_I + \left(\frac{\Delta t}{\Omega}\right)_\nu} \quad (4.28)$$

For steady simulations, a local time stepping is used because it increases the convergence rate. Each cell in the computation domain has its own time step given by the local inviscid time step equation (4.26), for viscous calculations by (4.28) [16].

### 4.4.3 Multigrid Strategy

A multigrid is used for efficiency and fast convergence. It consists of transferring residuals on to coarse grids, solving the modified system on these grids, and interpolating the new residual back to the fine grid. It has the property of smoothing the long wave errors much faster than by using only the fine grid. Three grid levels are used, respectively the number of sweep are 1, 4, 32. This strategy applies the Full Approximation Storage approach (coarse grid are created by agglomerating the cells surrounding a node) [17].

The Navier-Stokes problem for a kind of mesh can be written, with  $l = 1, \dots, L$  from the coarsest to the finest:

$$\frac{\partial U^l}{\partial t} + N_l(U^l) = F_l \quad (4.29)$$

$F_l$  is the forcing function, defined recursively as:

$$F_l = N_l(I_{l+1}^l U^{l+1}) + \hat{I}_{l+1}^l \left[ F_{l+1} - N_{l+1}(U^{l+1}) \right] \quad (4.30)$$

$I_{l+1}^l$  and  $\hat{I}_{l+1}^l$  represent restriction operators of the unknowns and the residuals. They are defined as:

$$\hat{I}_{l+1}^l R^{l+1} = \sum R^{l+1}, \quad I_{l+1}^l U^{l+1} = \frac{\sum \Omega^{l+1} U^{l+1}}{\sum \Omega^{l+1}}, \quad R^{l+1} = F_{l+1} - N_{l+1}(U^{l+1}) \quad (4.31)$$

$\Omega$  is the cell volume. The summation is over the 8 fine cells contained within a coarse cell.

After temporal discretization, the problem approximated on a coarse level becomes:

$$S\Delta U^l + N_l(U^{l(0)}) = F_l \quad (4.32)$$

$U^{l(0)} = I_{l+1}^l U^{l+1}$  is the current solution on mesh  $l$ , where the equations have been linearized (in an implicit method).  $\Delta U^l$  is an update of  $U^{l(0)}$  and is to be calculated.  $S$  is the smoother, the chosen time integration method.

The linear problem (4.32) can be solved for  $\Delta U^l$ . With  $S$  the updated solution  $U^l$  is smoothed and can be restricted to the next coarser level, replacing  $l - 1$  to  $l$  in  $U^{l(0)}$ .

The number of sweeps 1, 4, 32 is the number of times the Runge-Kutta operator is applied.

After that the solution on the coarsest mesh is smoothed, the coarse to fine sweep of the multigrid cycle is initiated. The current solutions on finer grids are updated

with the solution on the next coarser level:

$$U^l = U^l + \underline{I}_{l-1}^l (U^{l-1} - I_l^{l-1} U^l) \quad (4.33)$$

The underline means a prolongation operator of first-order. In the V, W, F cycle the new solution on the finer mesh is smoothed before proceeding to the next finer level, by solving  $I_{l+1}^l$  e  $\hat{I}_{l+1}^l$  with  $U^{l(0)} = U^l$ .

The computational cost of a multigrid cycle is reduced by using simplifying assumptions on coarser meshes. For central spatial discretization scheme a more diffusive central scheme is used [18].

#### 4.4.4 Full Multigrid Strategy

The solution in the coarsest grid is interpolated to the next finer grid, only when it converges to a certain accuracy level. The initial solution on the finest grid is called the solution obtained by a Full Multigrid method. If solutions do not converge on the coarser grid, it may cause divergence on the next finer grid. In addition, an initial solution on coarse grids is less sensitive to multigrid convergence than on the finest grid. A bigger cell size makes solution converge faster. This strategy increases the robustness and efficiency of numerical iterations methods [19].

The maximum number of cycles per grid level is set equal to 400 and the convergence criteria on each grid level is equal to -7.0.

#### 4.4.5 Implicit residual smoothing

An implicit residual smoothing is used in combination with Runge-Kutta to speed up the convergence to steady state. One stage in the explicit Runge-Kutta can be written [20]:

$$u^{m+1} = u^n + \alpha_m \Delta t F(u^m) = u^n + \alpha_m R(u^m) \quad (4.34)$$

The residual  $R$  is smoothed applying a central type operator leading to a smoothed residual  $\tilde{R}$ :

$$(I - \epsilon_i \Delta_i^2)(I - \epsilon_j \Delta_j^2)(I - \epsilon_k \Delta_k^2)\tilde{R} = R \quad \Delta_i^2 \tilde{R} = \tilde{R}_{i-1} - 2\tilde{R}_i + \tilde{R}_{i+1} \quad (4.35)$$

$\Delta_j^2$  and  $\Delta_k^2$  are defined in a similar way.

$\epsilon$  is a smoothing parameter on which the stability criterion is:

$$\epsilon > \frac{1}{4} \left[ \left( \frac{\sigma^*}{\sigma} \right)^2 - 1 \right] \quad (4.36)$$

$\sigma^*$ ,  $\sigma$  are the CFL number of the smoothed and unsmoothed Runge-Kutta schema.

A good practical value is  $\sigma^*/\sigma = 2$ .

## 4.5 Rotor/Stator Interaction

It is a sources of unsteadiness that may affect the turbomachinery flow. It requires an unsteady and viscous flow solver able to manage enormous data storage. It is possible to optimize the process solving the steady flow field on a truncated computational domain. The rotor-stator interaction is done by exchanging circumferentially averaged flow quantities [21].

### 4.5.1 Full Non-matching Technique for Mixing Planes

The full non matching mixing plane module uses the concept of image. An image of the real mesh patches is built on both sides of the interface, the left and right images respecting the above constraints and being in addition matching in the spanwise direction [22].

The communication algorithm between rotors and stators is organised in several steps:

1. Extrapolation of the flow solution from the inner cells to the boundary.
2. Sending of the flow solution from the initial mesh to the image.

3. Application of the mixing plane algorithm between the left and right images, with construction of flux variables to be imposed on the left and right side.
4. Sending of the fluxes from the image to the initial meshes.

## 4.6 Turbulence Models

On Numeca Fine are present the turbulence models in the list below [23]:

1. Linear Eddy Viscosity Turbulence models:
  - Algebraic model:
    - Baldwin-Lomax
  - One equation model:
    - Spalart-Allmaras
    - Spalart-Allmaras (Extended Wall Function)
  - Two equation model:
    - $k$ - $\epsilon$  (Standard wall function)
    - $k$ - $\epsilon$  (Extended wall function)
    - $k$ - $\epsilon$  (Low Re Chien)
    - $k$ - $\epsilon$  (Low Re Yang-Shih)
    - $k$ - $\epsilon$  (Low Re Launder-Sharma)
    - $k$ - $\omega$  (Wilcox)
    - Shear Stress Transport (SST)
    - SST (Extended wall function)
  - Four equation model:
    - $v^2$ -f (code friendly)
2. Nonlinear Eddy Viscosity Turbulence models:
  - Two equation model:

- EARSM
- EARSM (Extended wall function)

### 4.6.1 Spalart-Allmaras Model

It is a one equation turbulence model. The Spalart-Allmaras model has become quite popular in the last years because of its robustness and its ability to treat complex flows. The main advantage over Baldwin-Lomax is that the turbulent eddy viscosity field is always continuous. Its advantage over the k- $\epsilon$  model is its robustness, the lower additional CPU and memory usage.

An additional transport equation for the eddy viscosity is resolved. In the equation there are an advective, a diffusive and a source term and it is implemented in a non conservative manner. The implementation is based on the paper of Spalart and Allmaras (1992) with the improvements described in Ashford and Powell (1996) in order to avoid negative values for the production term ( $\tilde{S}$ ) [24]. The turbulent viscosity is given by

$$\nu_T = \tilde{\nu} f_{\nu 1} \quad (4.37)$$

where  $\tilde{\nu}$  is the turbulent working variable and  $f_{\nu 1}$  a function defined by

$$f_{\nu 1} = \frac{\chi^3}{\chi^3 + c_{\nu 1}^3} \quad (4.38)$$

$\chi$  is the ratio between the working variable  $\tilde{\nu}$  and the molecular viscosity  $\nu$ . The turbulent working variable is described by the transport equation

$$\frac{\partial \tilde{\nu}}{\partial t} + \vec{V} \cdot \nabla \tilde{\nu} = \frac{1}{\sigma} \left\{ \nabla \cdot \left[ (\nu + (1 + c_{b2})\tilde{\nu}) \nabla \tilde{\nu} \right] - c_{b2} \tilde{\nu} \delta \tilde{\nu} \right\} + S_T \quad (4.39)$$

$\vec{V}$  is the velocity vector,  $S_T$  the source term and  $\sigma$ ,  $c_{b2}$  are constants. The source term is splitted in a production term  $P(\tilde{\nu})$  and a destruction term  $D(\tilde{\nu})$

$$S_T = \tilde{\nu} P(\tilde{\nu}) - \tilde{\nu} D(\tilde{\nu}) \quad (4.40)$$

where

$$\tilde{\nu}P(\tilde{\nu}) = c_{b1}\tilde{S}\tilde{\nu}, \quad \tilde{\nu}D(\tilde{\nu}) = c_{w1}f_w\left(\frac{\tilde{\nu}}{d}\right)^2 \quad (4.41)$$

The production term P is constructed with the following functions:

$$\tilde{S} = Sf_{\nu3} + \frac{\tilde{\nu}}{\kappa^2 d^2} f_{\nu2}, \quad f_{\nu2} = \frac{1}{(1 + \chi/c_{v2})^3}, \quad f_{\nu3} = \frac{(1 + \chi f_{v1})(1 - f_{v2})}{\chi} \quad (4.42)$$

$d$  is the distance to the closest wall and  $S$  the magnitude of vorticity.

In the destruction D

$$f_w = g\left(\frac{1 + c_{w3}^6}{g^6 + c_{w3}^6}\right)^{1/6} \quad (4.43)$$

with

$$g = r + c_{w2}(r^6 - r), \quad r = \frac{\tilde{\nu}}{\tilde{S}\kappa^2 d^2} \quad (4.44)$$

The values of the constants in this model are:

$$c_{w1} = \frac{c_{b1}}{\kappa^2} + \frac{(1+c_{b2})}{\sigma}, \quad c_{w2} = 2, \quad c_{w3} = 2, \quad c_{v1} = 7.1, \quad c_{v2} = 5, \quad c_{b1} = 0.1355, \quad c_{b2} = 0.622, \\ \kappa = 0.41, \quad \sigma = 2/3.$$

## 4.6.2 k- $\epsilon$ Model

In the k- $\epsilon$  turbulence model two additional transport equations for the turbulent kinetic energy,  $k$ , and the turbulent dissipation rate,  $\epsilon$ , are solved. The starting point is

$$\nu_T(\vec{x}, t) = u^*(\vec{x}, t) \cdot l^*(\vec{x}, t) \quad (4.45)$$

The reference velocity  $u^*$  is taken as the square root of the turbulent kinetic energy and a length scale can be formed from  $k$  and  $\epsilon$ :

$$u^* \approx k^{1/2}, \quad l^* \approx k^{3/2}/\epsilon \quad (4.46)$$

The turbulent viscosity is then assumed to be:

$$\nu_T = C_\mu \frac{k^2}{\epsilon} \quad (4.47)$$

$C_\mu$  is one of the five model constants.

The model equation for  $k$ :

$$\frac{\partial k}{\partial t} + U_i \frac{\partial k}{\partial x_i} = \Pi - \epsilon - \frac{\partial I_i}{\partial x_i} \quad (4.48)$$

where

$$\Pi = -\overline{u'_i u'_j} \frac{\partial U_i}{\partial x_j}, \quad I_i = -\frac{\nu_T}{\sigma_k} \frac{\partial k}{\partial x_i} \quad (4.49)$$

The exact equation for  $\epsilon$  could be derived, but it is not useful because it would refer to processes in the dissipative range. It is preferred to express  $\epsilon$  as the energy flow rate in the energy cascade, determined by the large scale motions [25].

The empiric model equation for  $\epsilon$ :

$$\frac{\partial \epsilon}{\partial t} + U_i \frac{\partial \epsilon}{\partial x_i} = C_{\epsilon 1} \frac{\epsilon}{k} \Pi - C_{\epsilon 2} \frac{\epsilon^2}{k} + \frac{\partial}{\partial x_i} \left( \frac{\nu_T}{\sigma_\epsilon} \frac{\partial \epsilon}{\partial x_i} \right) \quad (4.50)$$

The values of the constant are:

- Extended wall function [26]

$$C_\mu = 0.09, C_{\epsilon 1} = 1.44, C_{\epsilon 2} = 1.92, \sigma_k = 1.0, \sigma_\epsilon = 1.3.$$

- Chien [26]

$$C_\mu = 0.09, C_{\epsilon 1} = 1.35, C_{\epsilon 2} = 1.80, \sigma_k = 1.0, \sigma_\epsilon = 1.3.$$

# Chapter 5

## Performance Curves

### 5.1 Numeca Fine

*Numeca Fine* is the program used to the CFD calculations. To study the influence of Flow Pass, curves made of 12 points curves are created. To reduce computational cost they are reduced to 8 points in the subsequent calculations. In Figure (5.1) there is an example of points definition.

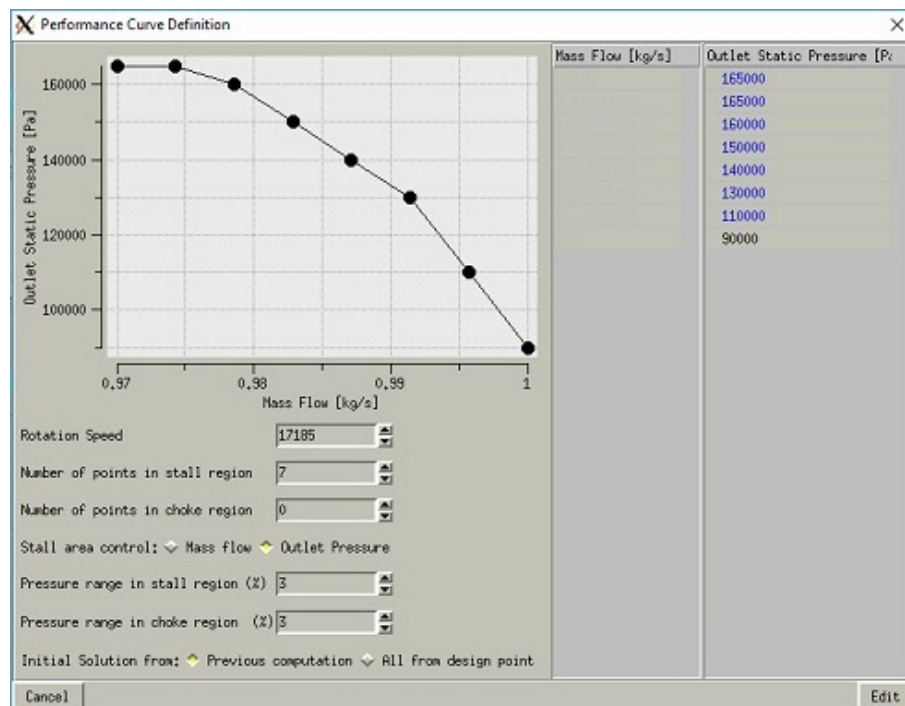


Figure 5.1: Performance Curve Points Definition

In Computation Steering → Convergence History it is possible to check global resid-

ual, inlet mass flow, outlet mass flow, efficiency and pressure ratio value during calculation. For example for the choke point, Figure (5.2).

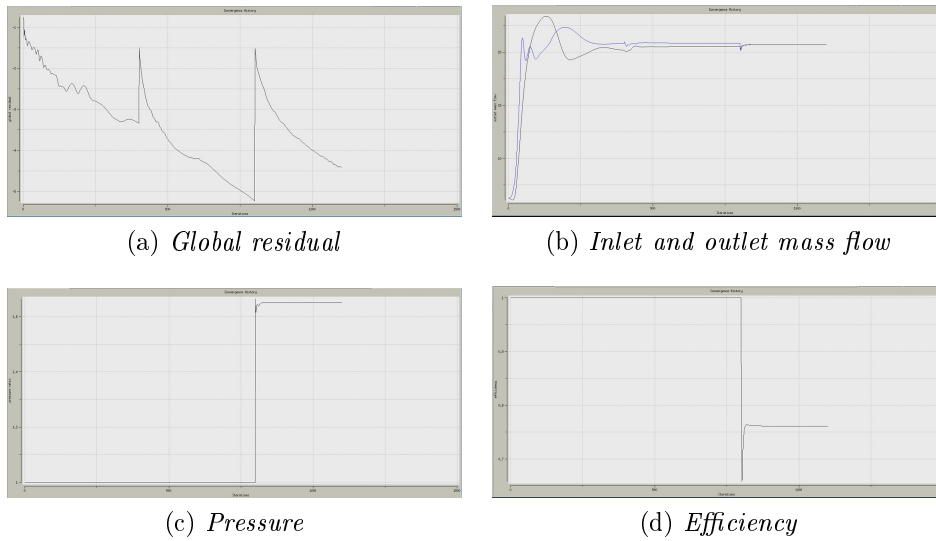


Figure 5.2

Figure (5.3) is an example of a generic point convergence. If the pressure ratio is not constant but decreases, the outlet static pressure of the corresponding point has to be decrease and re-start calculation from that point.

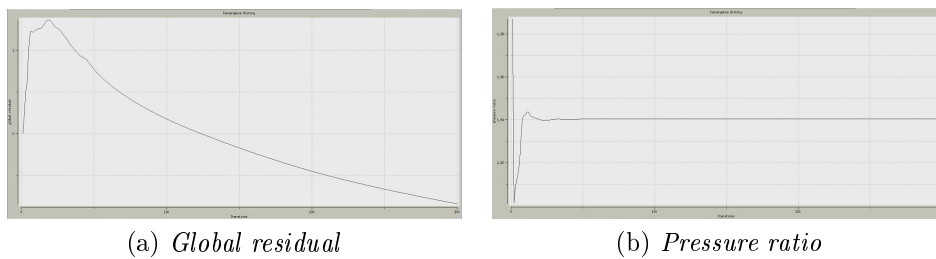


Figure 5.3

Figure (5.4) instead is an example of a point divergence, an outlet static pressure decrease doesn't solve the problem because near the stall region the curve is approximately constant in mass flow-pressure ratio graph. The mass flow value is imposed instead of pressure.

This calculations were ran using a cluster of CPUs (12, 16 or 20), the calculation time was from 2/3 to 5 hours.

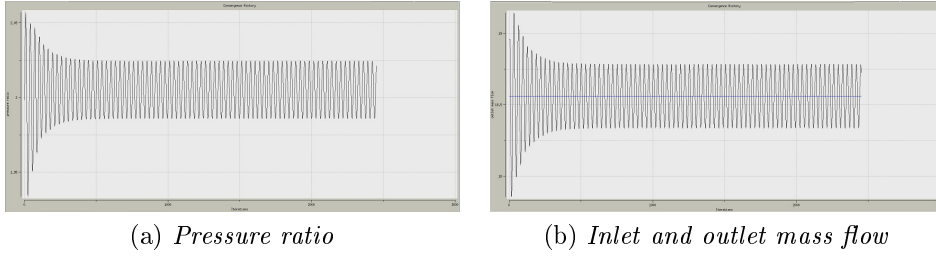


Figure 5.4

## 5.2 Performance Curves Comparison

With the mass flow, the pressure ratio and the efficiency for each point it is possible to create the performance curves and compare them each other and with the experimental data. Starting with the influence of flow pass:

- Expansion Ratio influence

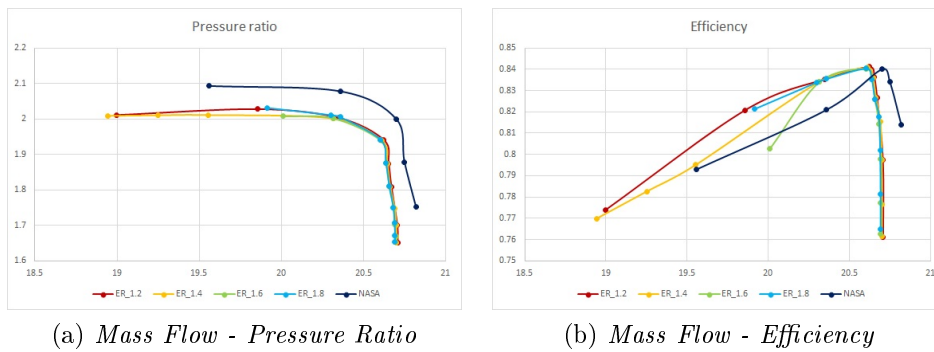


Figure 5.5

The E.R. 1.6 and 1.8 meshes have a smaller stall margin.

- Max Aspect Ratio influence

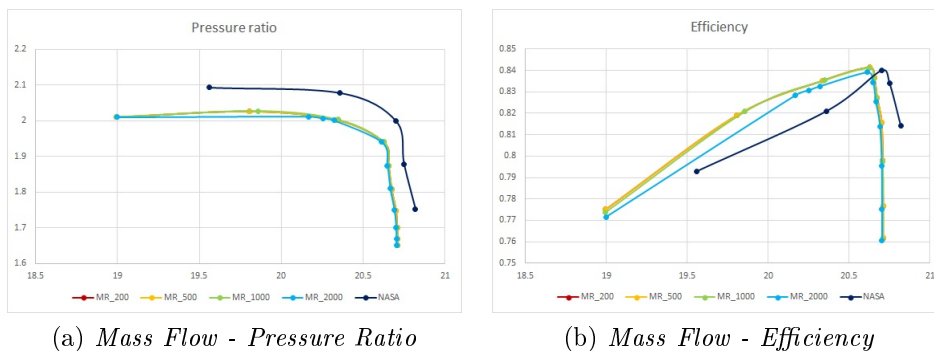


Figure 5.6

The MR 200 and MR 500 meshes are coincident. In efficiency graph, there is a clear difference for lower mass flow between MR 2000 and the others meshes.

- $y^+$  influence

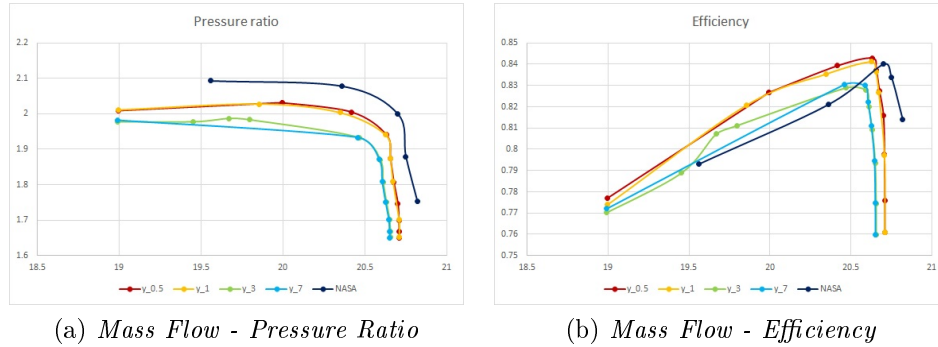


Figure 5.7

In pressure ratio graph there is a clear difference between  $y^+ = 0.5, 1$  and  $y^+ = 3, 7$ . In efficiency graph for lower mass flow the difference between the two groups is lower. Now the influence of blade to blade meshes is evaluated:

- Expansion Ratio influence

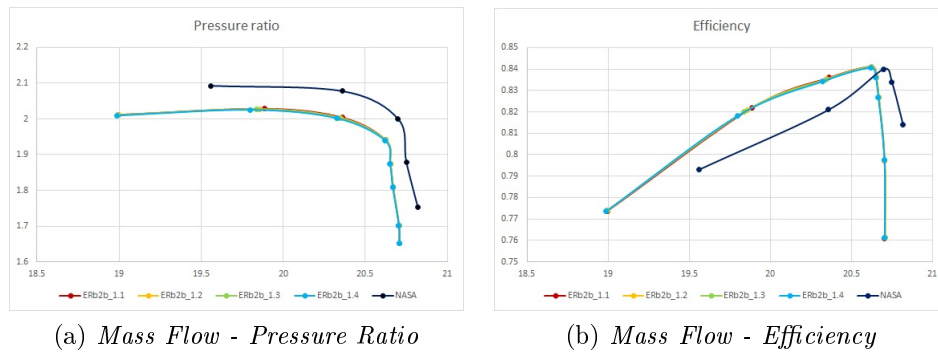


Figure 5.8

There are not appreciable differences.

- O-layer influence

There are not appreciable differences.

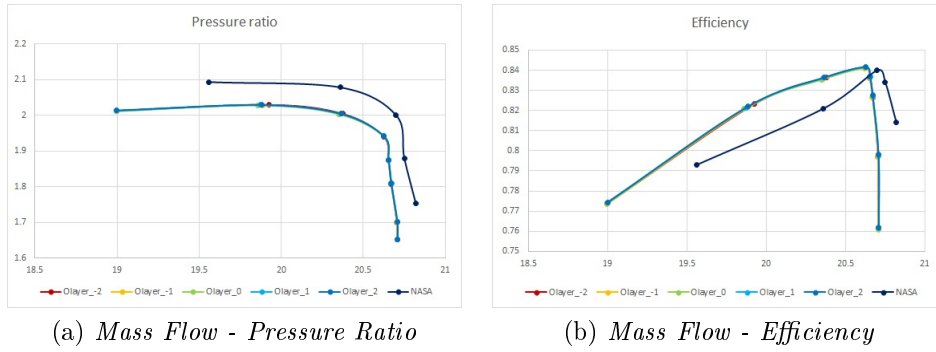


Figure 5.9

- Mesh Density influence

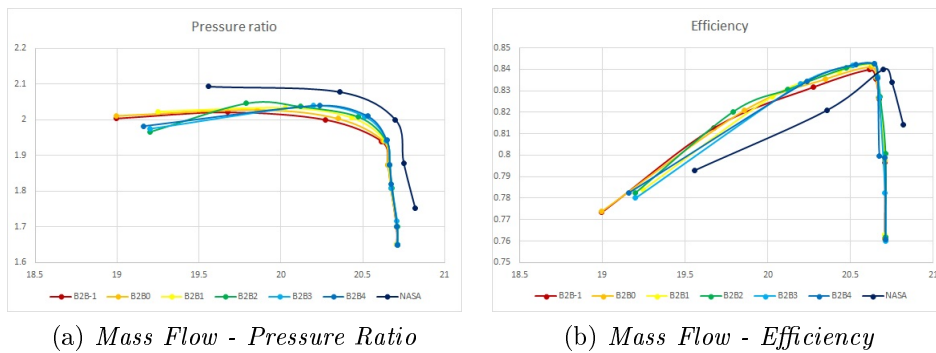


Figure 5.10

The B2B2, B2B3 and B2B4 last point solution has small oscillation, so the average value was taken to compare the flow behavior in stall point. These three meshes present a bigger number of elements, they should describe better the flow.

- Turbulence Models

The turbulence models implemented in *Numeca Fine* are compared each other and with experimental data. Some of them are not suitable to this kind of problem, Figure (5.11).

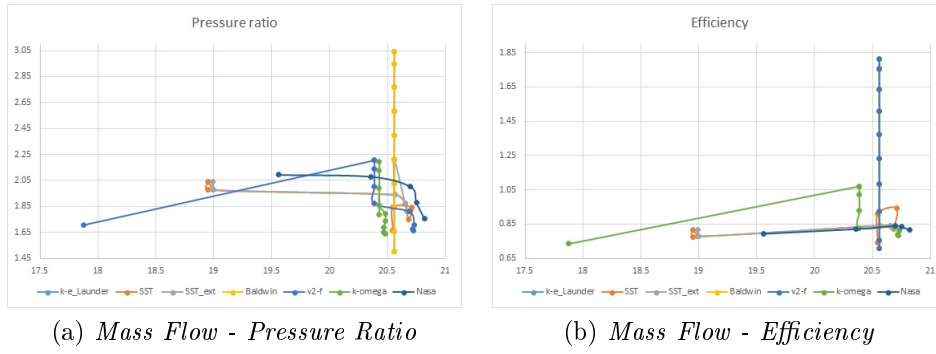


Figure 5.11

In the following comparison  $k-\epsilon_{Chien}$  and  $EARSM$  are not considered because the former is not able to describe flow at lower mass flow (stall point region), the latter in the choke point region.

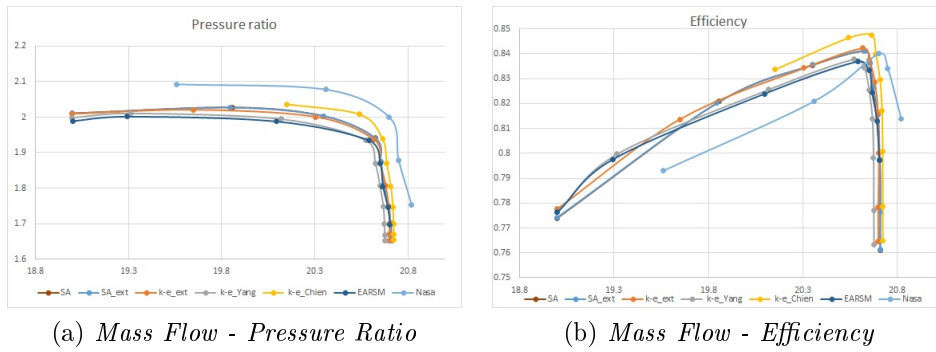


Figure 5.12

## 5.3 Radial distribution

The previous analysis is not sufficient to choose the best mesh. The second step is to compare the radial distribution of six variables at the max efficiency point:

1. Compressor outlet flow angle,  $\alpha$
2. Rotor outlet flow angle,  $\beta$
3. Absolute total temperature ratio,  $\frac{T_2^\circ}{T_1^\circ}$
4. Absolute total pressure ratio,  $\frac{p_2^\circ}{p_1^\circ}$
5. Loss coefficient,  $\psi = \frac{p_2^\circ - p_1^\circ}{p_1^\circ - p_1}$
6. Adiabatic coefficient,  $\eta = T_1^\circ \frac{\left(\frac{p_2^\circ}{p_1^\circ}\right)^{\frac{\gamma-1}{\gamma}} - 1}{T_2^\circ - T_1^\circ}$

- Expansion Ratio influence

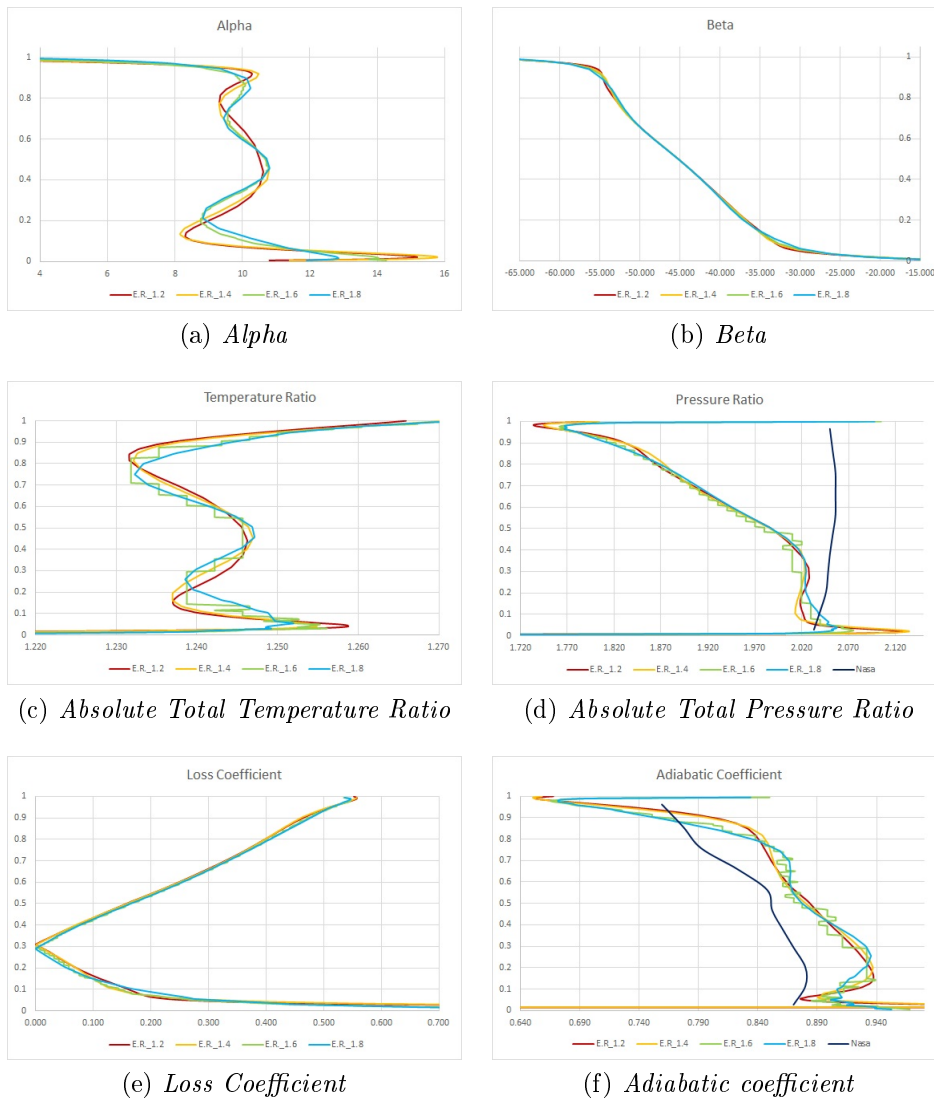


Figure 5.13: Expansion Ratio influence

Increasing the elements number the distribution is smoother, where the curvature is greater the worst meshes approximation is a broke line. The ER 1.2 and ER 1.4 approximation are similar but with not negligible differences.

- Max Aspect Ratio influence

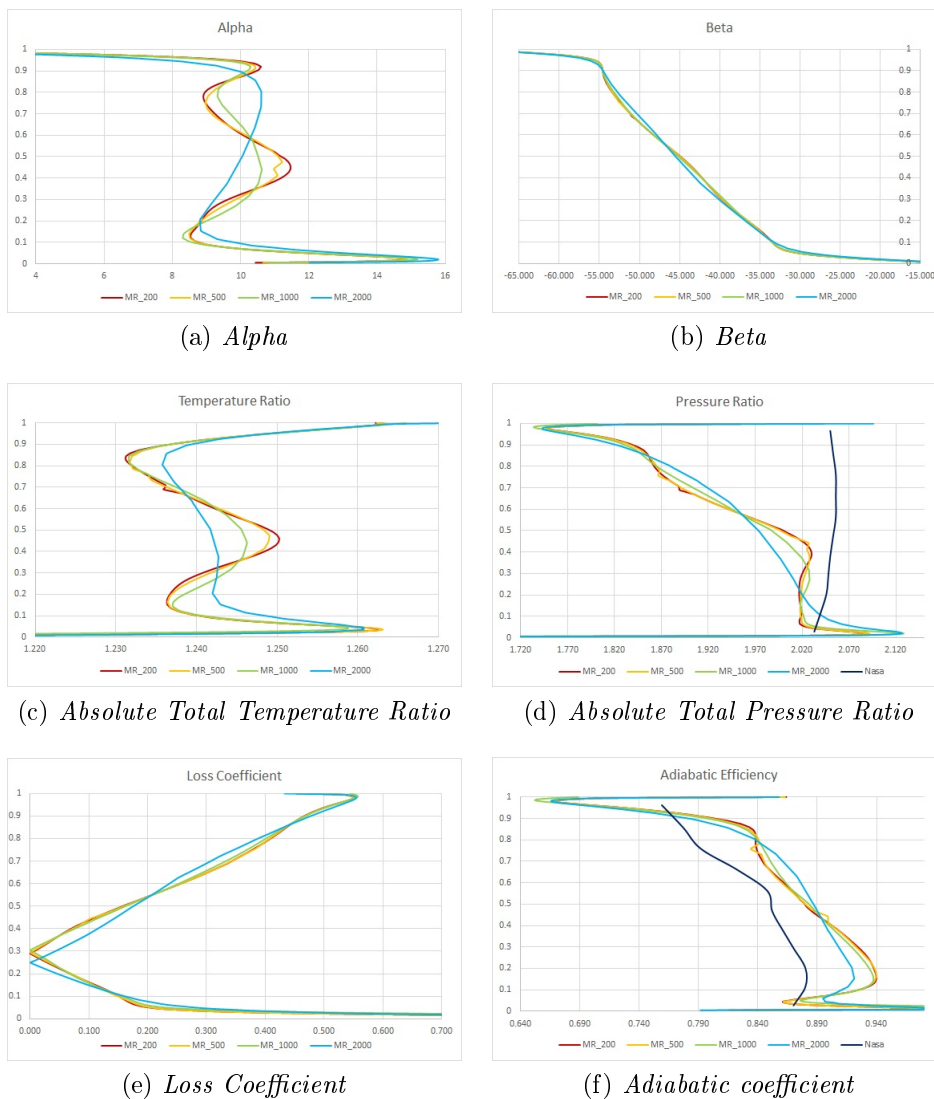


Figure 5.14: Max Aspect Ratio influence

MR 2000 approximation is very different from the others, the elements number is not sufficient. The other meshes approximation are similar but with not negligible differences between MR200-500 and MR1000.

- $y^+$  influence

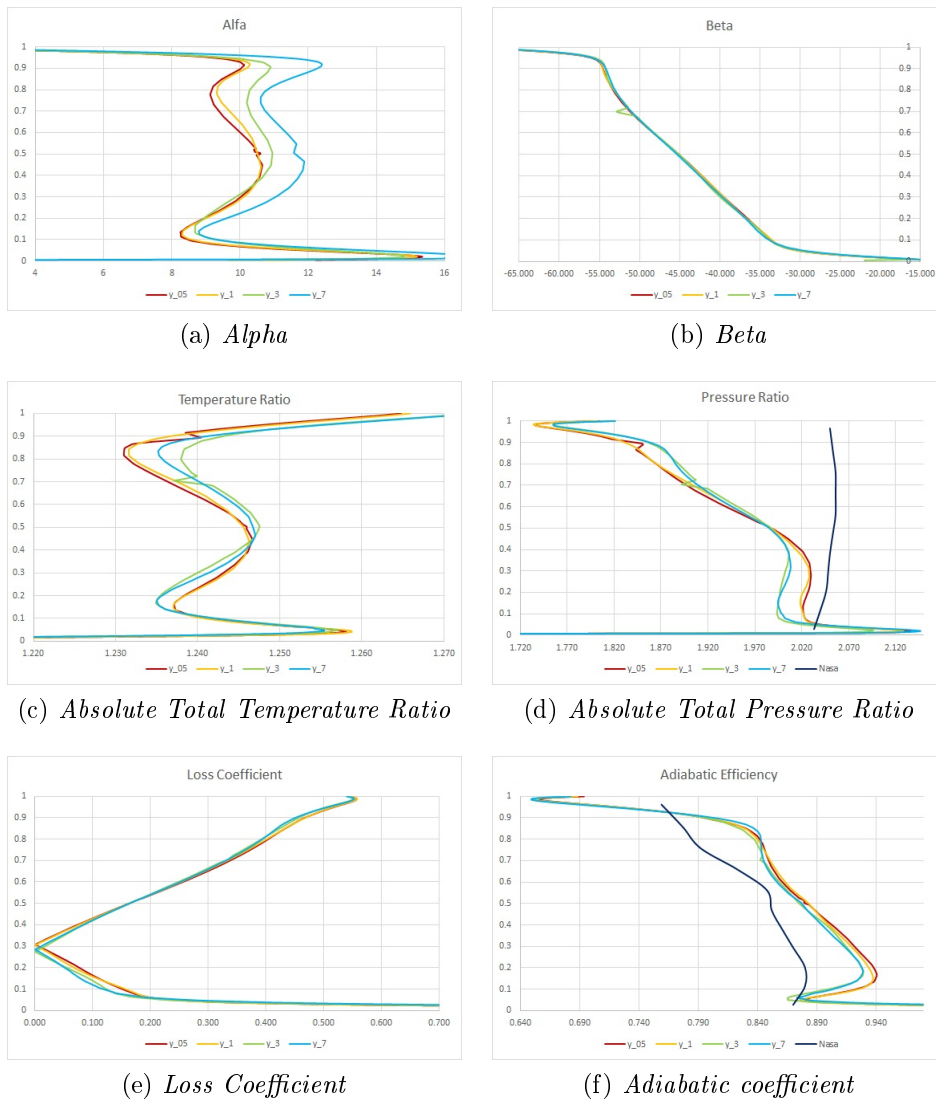


Figure 5.15:  $y^+$  influence

$y^+ = 3$  and  $y^+ = 7$  approximation are different from the other two. The differences between  $y^+ = 0.5$  and  $y^+ = 1$  are not so big.

- Expansion Ratio influence, Blade to Blade

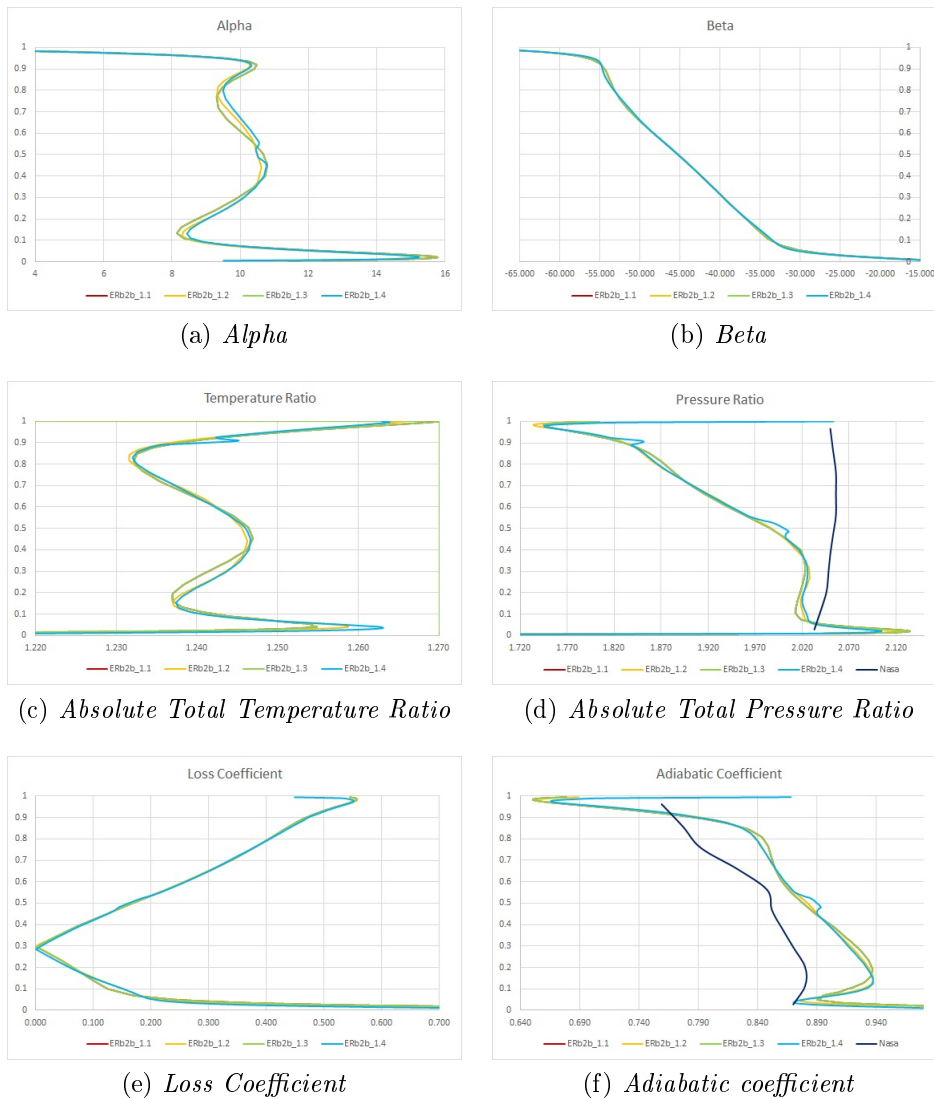


Figure 5.16: Expansion Ratio influence

The differences are smaller in this case. ER 1.1 and ER 1.3 are coincident.

- O-layer influence

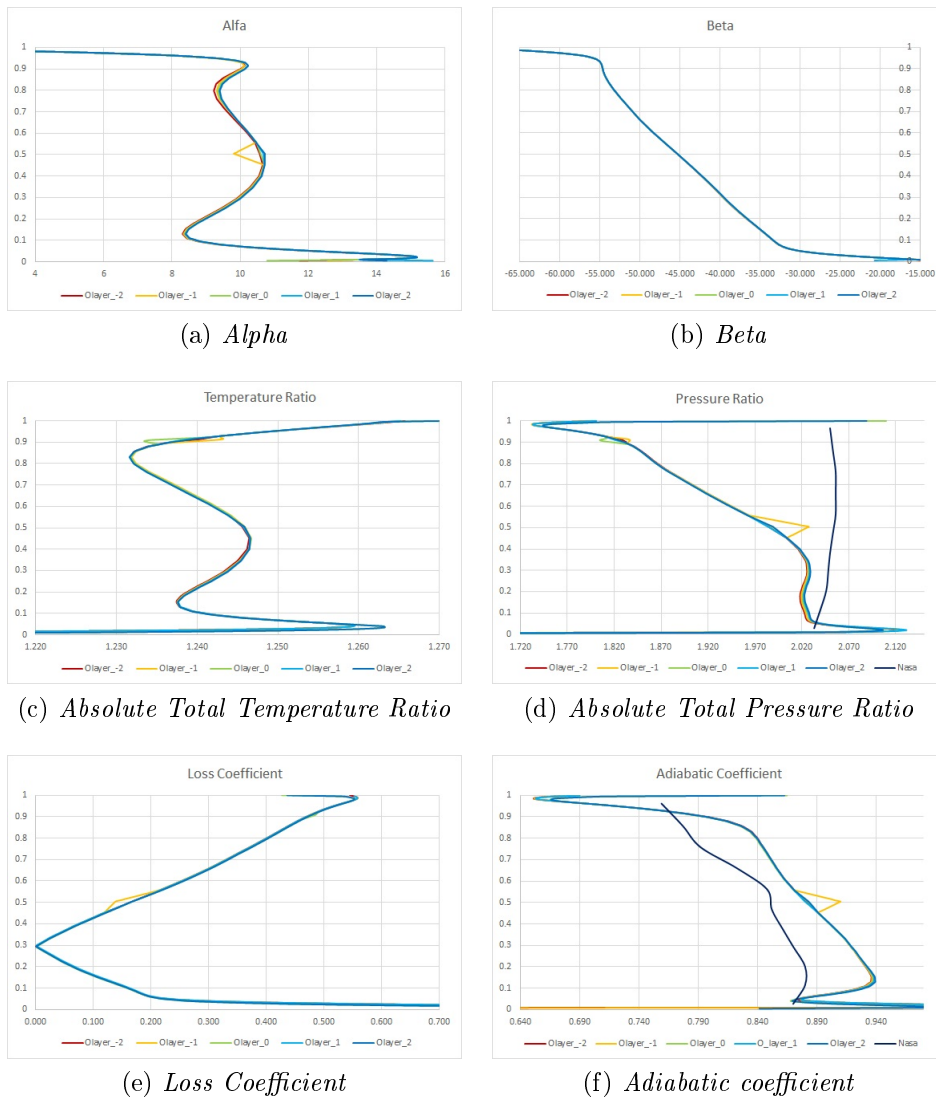


Figure 5.17: O-layer influence

The differences are not important.

- Mesh Density influence

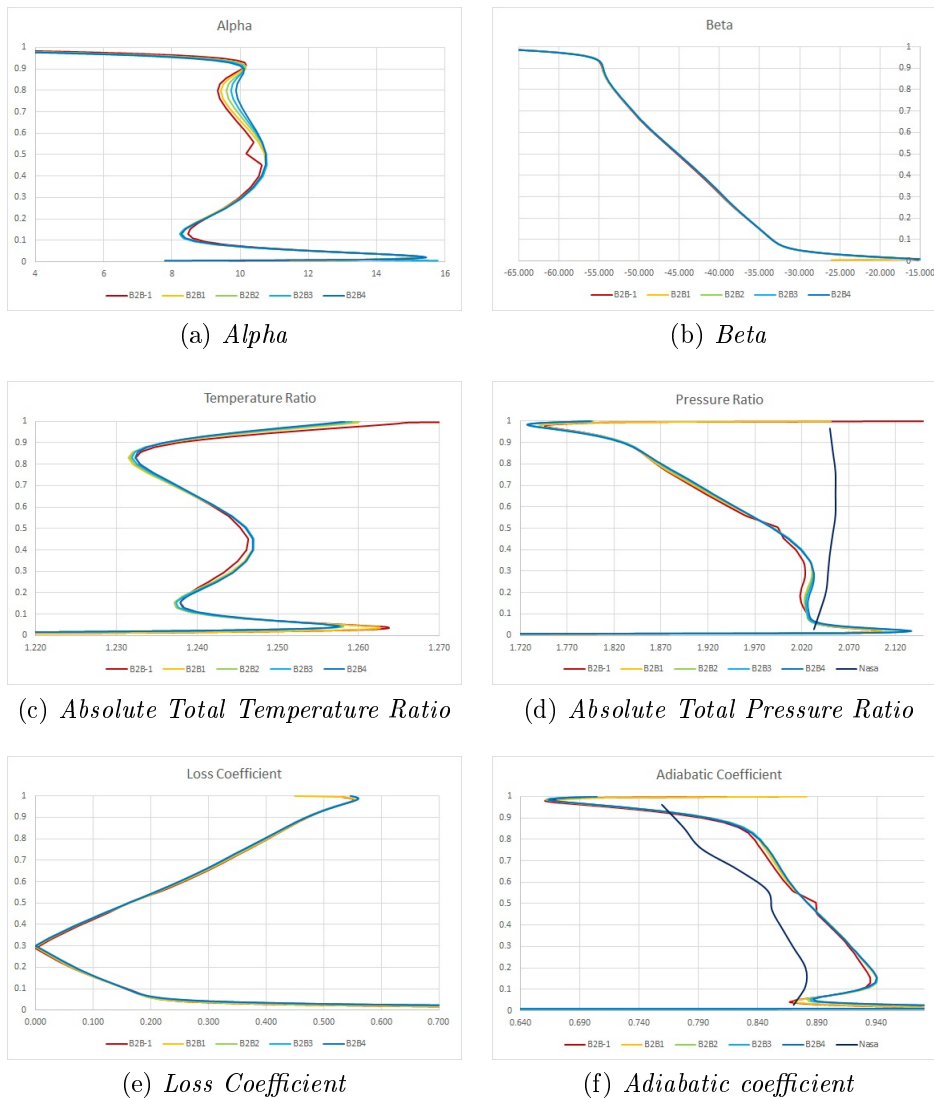


Figure 5.18: Mesh Density influence

The greatest differences are between B2B-1, B2B1 and the other approximations.

- Turbulence Models

Spalart-Allmaras and Spalart-Almaras extended are exactly coincident.  $k - \epsilon$  extended and  $k - \epsilon$  Yang are similar. SA and  $k - \epsilon$  models have considerable differences. Comparing these graphs to the  $y^+$  ones, it is possible to notice some analogies. In particular  $k - \epsilon$  distributions are similar to  $y^+ = 3$  and  $y^+ = 7$ , that are meshes with a lower number of elements.

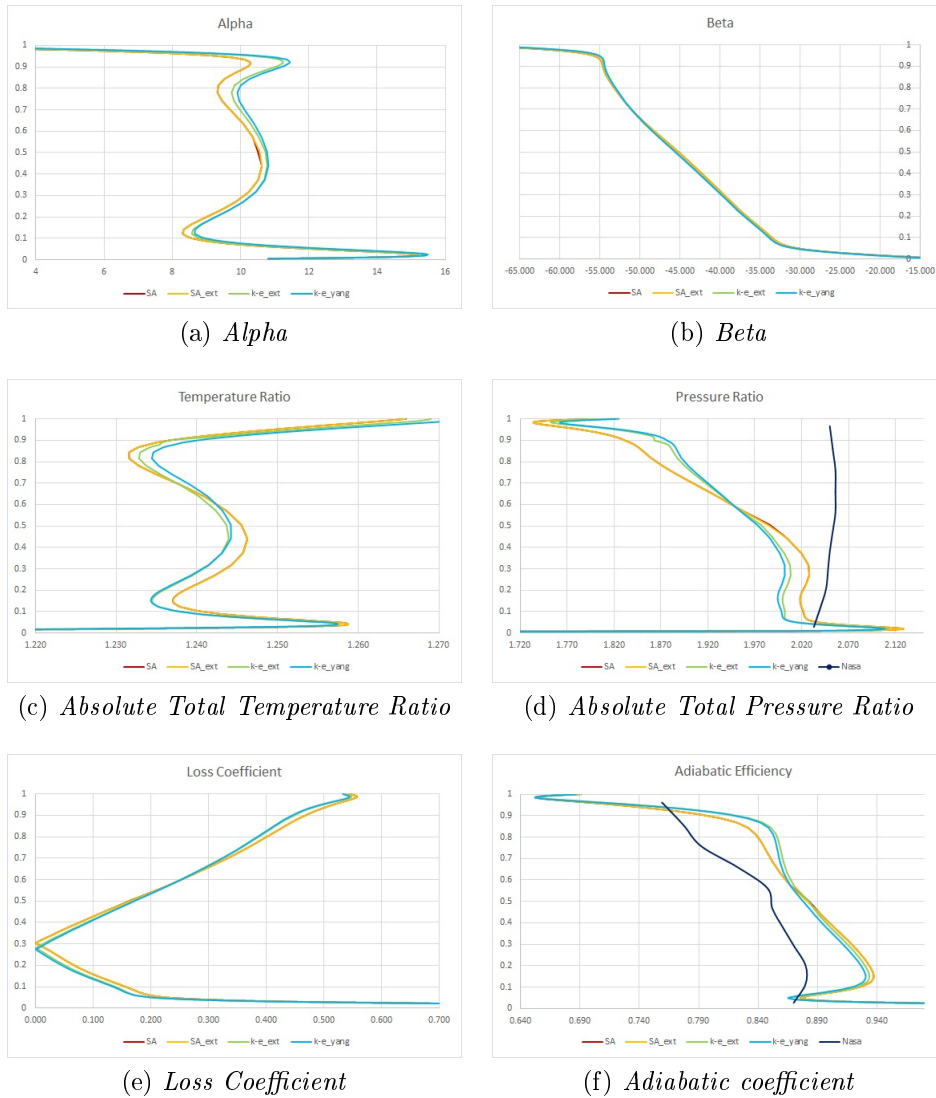


Figure 5.19: Turbulence Model influence

## 5.4 Flow Visualization

Using CFView it is possible to visualize the flow. In particular Mach number, Total Pressure and Turbulent Viscosity are evaluated.

Considering the rotor and stator in figure two plane parallel to x-y are created, the former at the rotor exit and the latter at the stator exit. The influence of b2b is examined with a plane parallel to y-z. The flow is visualized in max efficiency point and, when it is possible, in stall point.

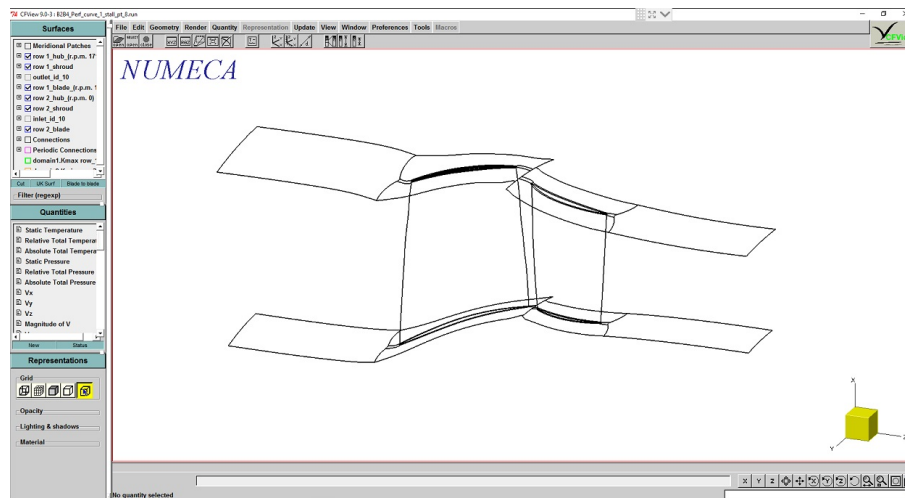


Figure 5.20: Rotor and Stator

## 5.4.1 Expansion Ratio influence

*Max Efficiency Point*

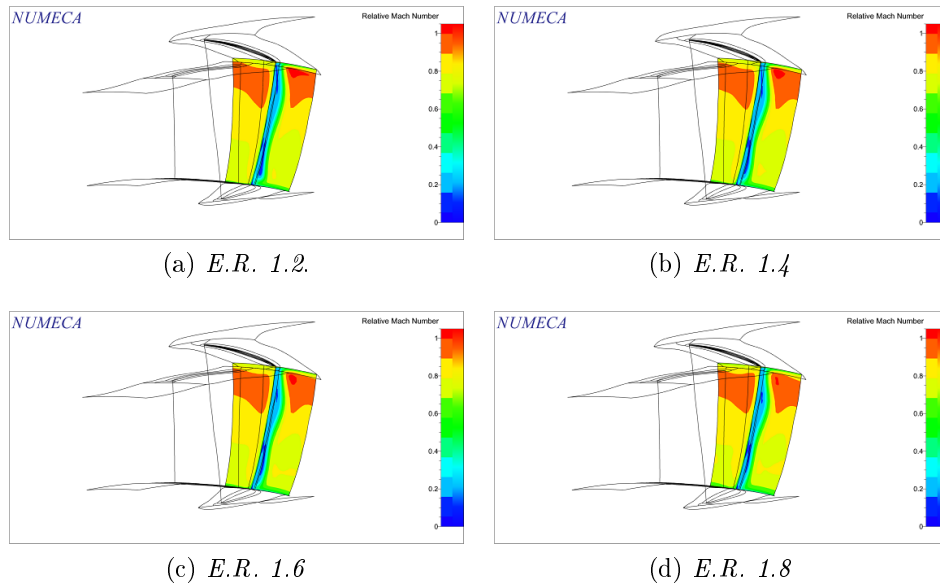


Figure 5.21: Relative Mach - Rotor

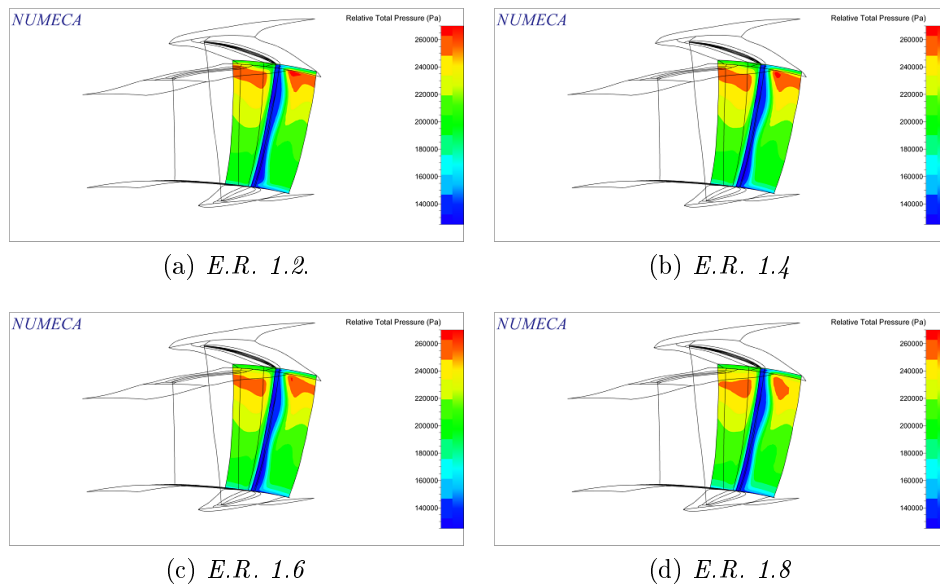


Figure 5.22: Relative Pressure Ratio - Rotor

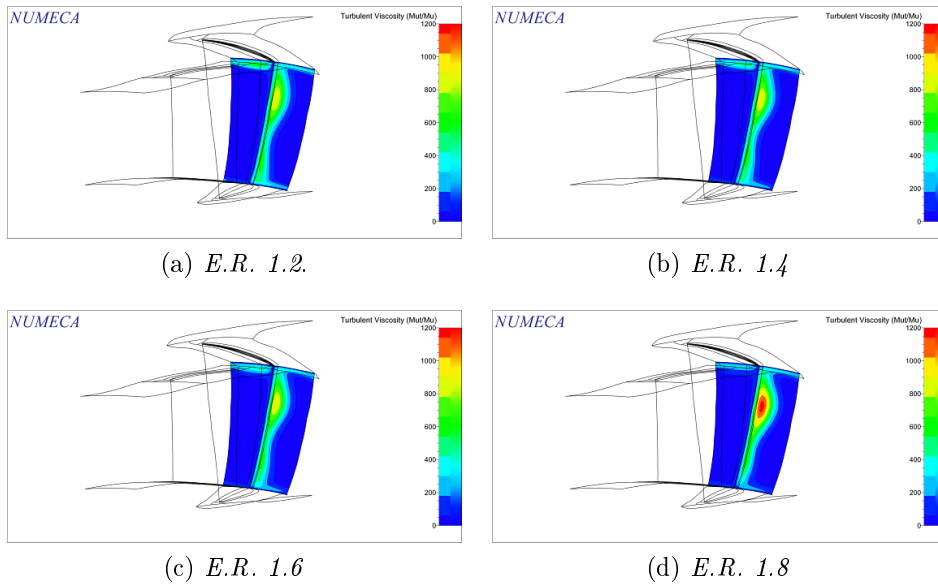


Figure 5.23: Turbulent Viscosity - Rotor

Observations:

- Increasing the meshes elements increase the area with higher Relative Mach number.
- Increasing the meshes elements increase the area with higher Relative Pressure Ratio.
- Increasing the meshes elements decrease the area with higher Turbulent Viscosity.

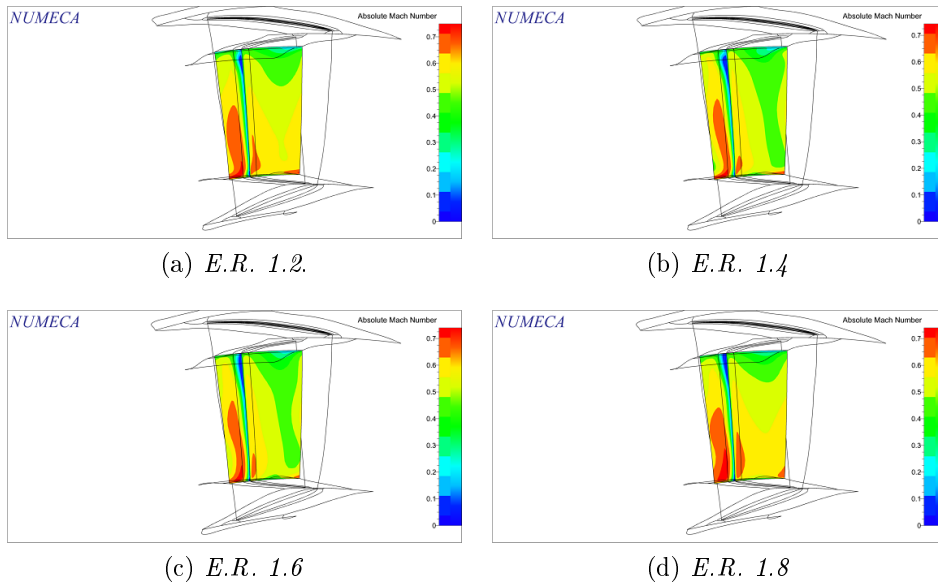


Figure 5.24: Absolute Mach - Stator

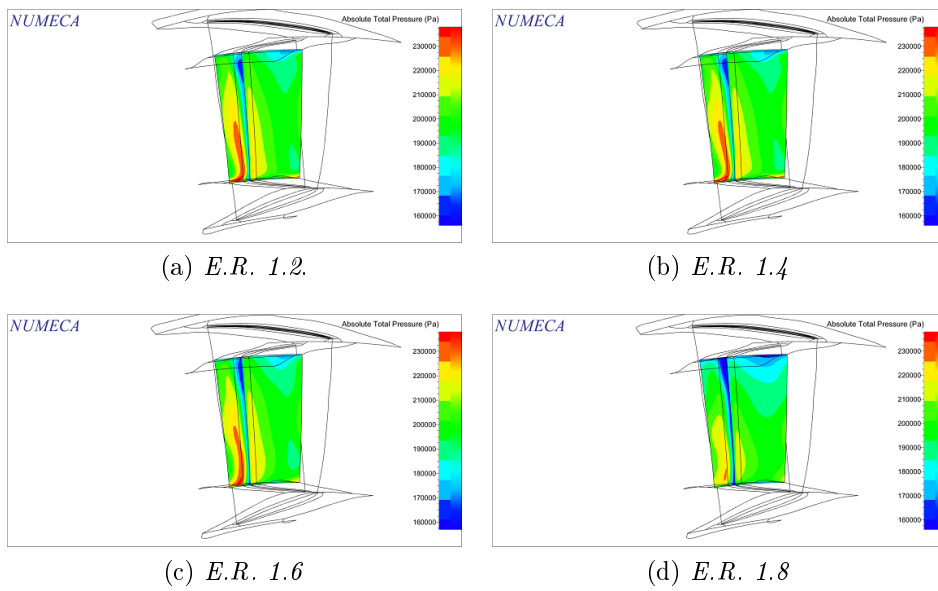


Figure 5.25: Absolute Pressure Ratio - Stator

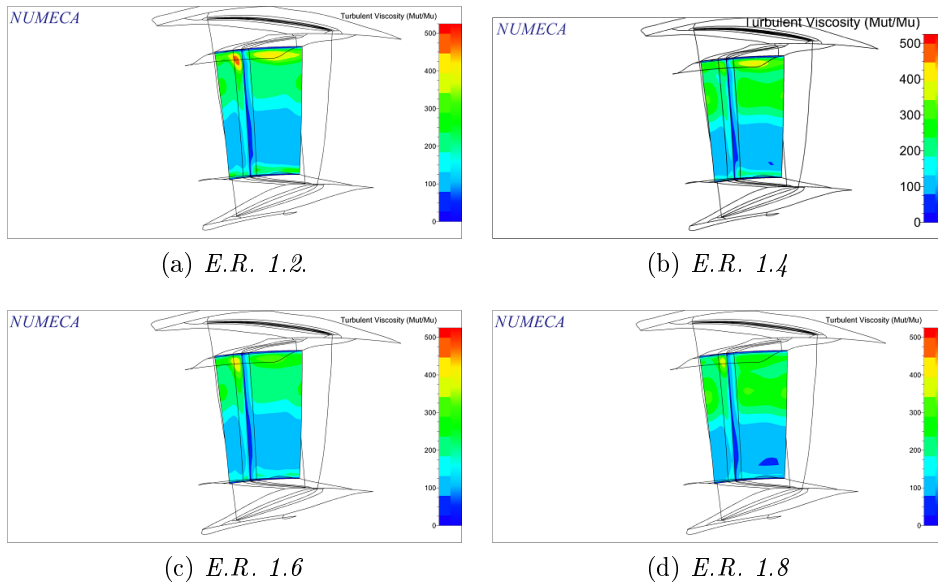


Figure 5.26: Turbulent Viscosity - Stator

Observations:

- Increasing the meshes elements increase the area with higher Absolute Mach number.
- Increasing the meshes elements increase the area with higher Absolute Pressure Ratio.
- Increasing the meshes elements increase the area with higher Turbulent Viscosity.

*Stall Point*

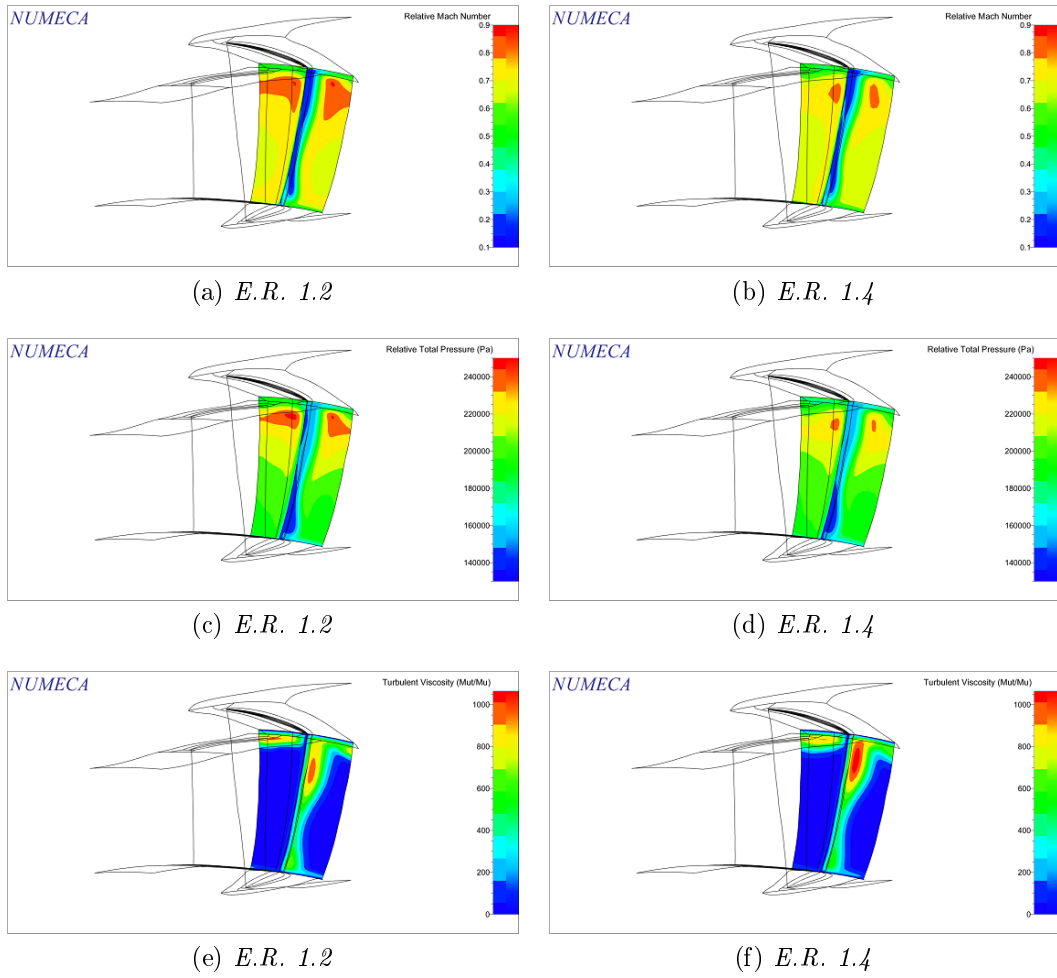


Figure 5.27: Rotor

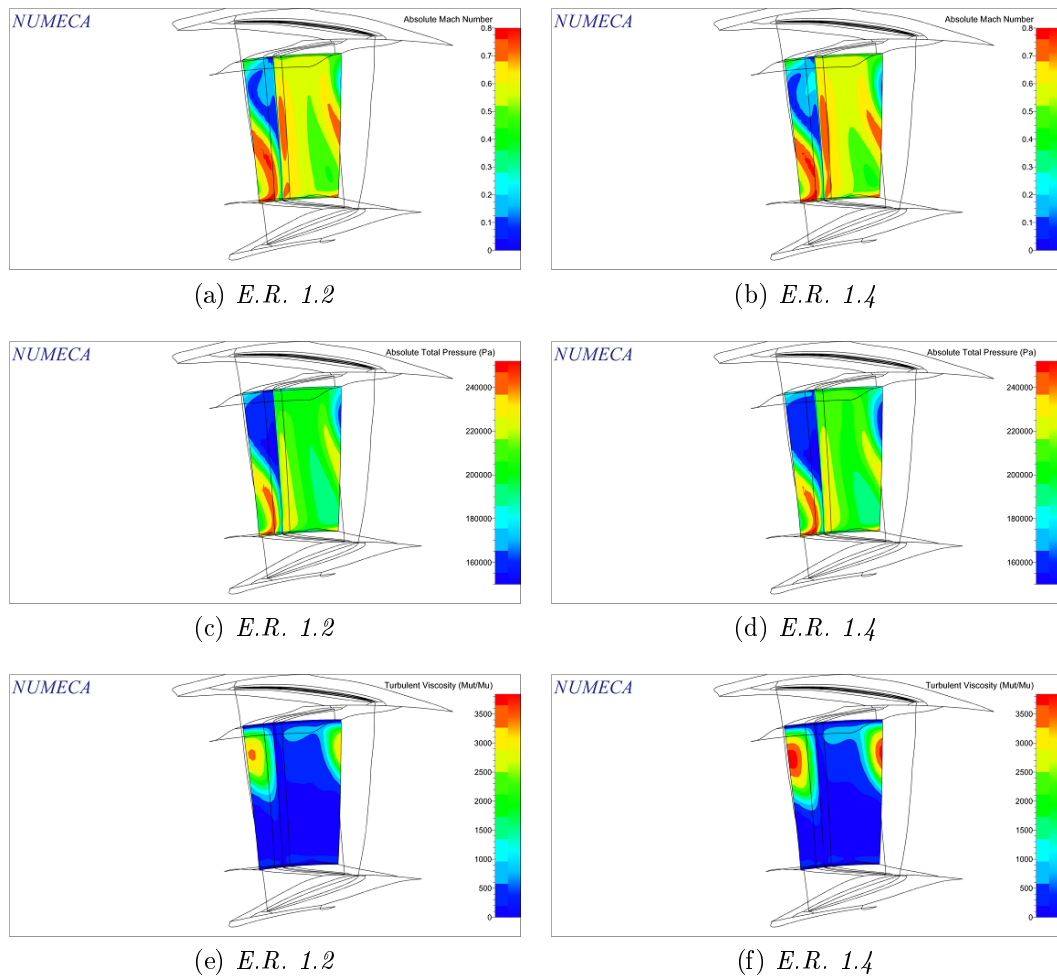


Figure 5.28: Stator

Looking at this graphs it is possible to confirm that the description is greater and greater increasing the elements. In particular in stall point ER 1.2 and ER 1.4 have great differences, so the former is chosen.

## 5.4.2 Max Aspect Ratio influence

*Point of Max Efficiency*

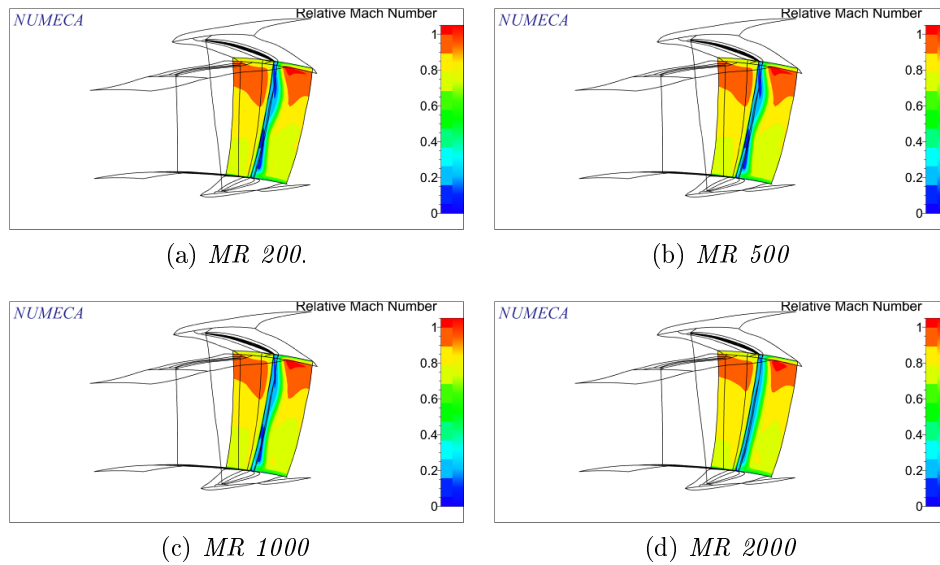


Figure 5.29: Relative Mach - Rotor

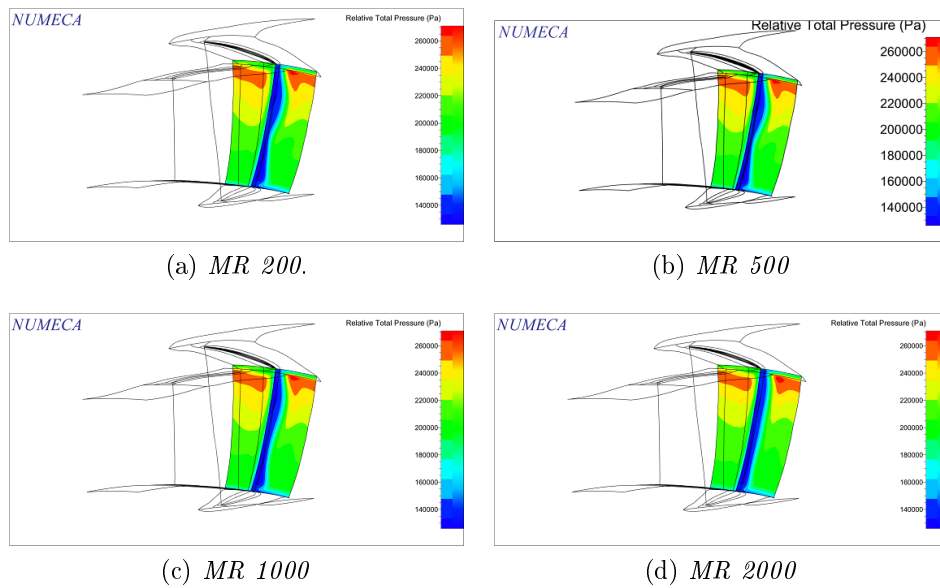


Figure 5.30: Relative Pressure Ratio - Rotor

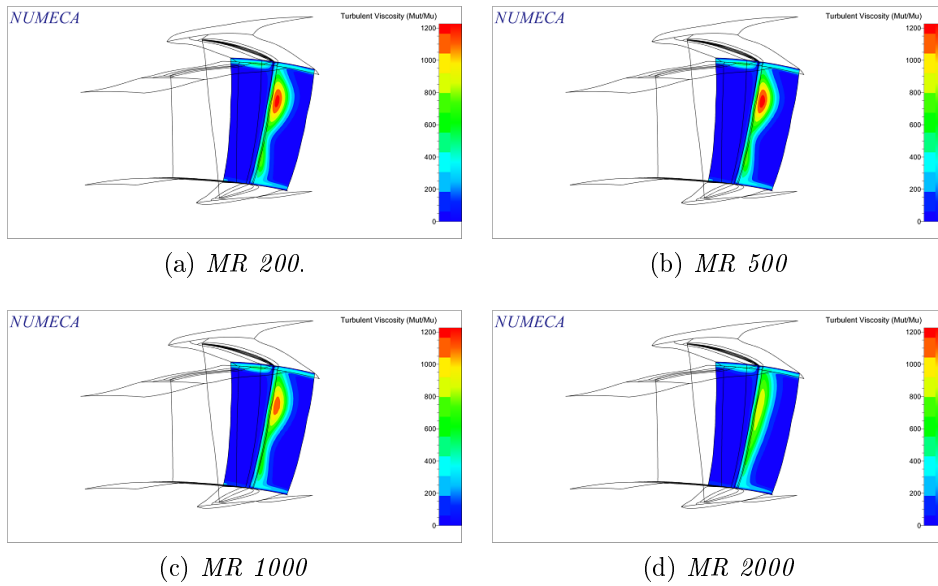


Figure 5.31: Turbulent Viscosity - Rotor

Observations:

- Only the worst mesh has some differences from the others, both for the Relative Mach number and the Relative Pressure Ratio.
- Increasing the meshes elements increase the area with higher Turbulent Viscosity. There are not appreciable differences between MR 200 and 500.

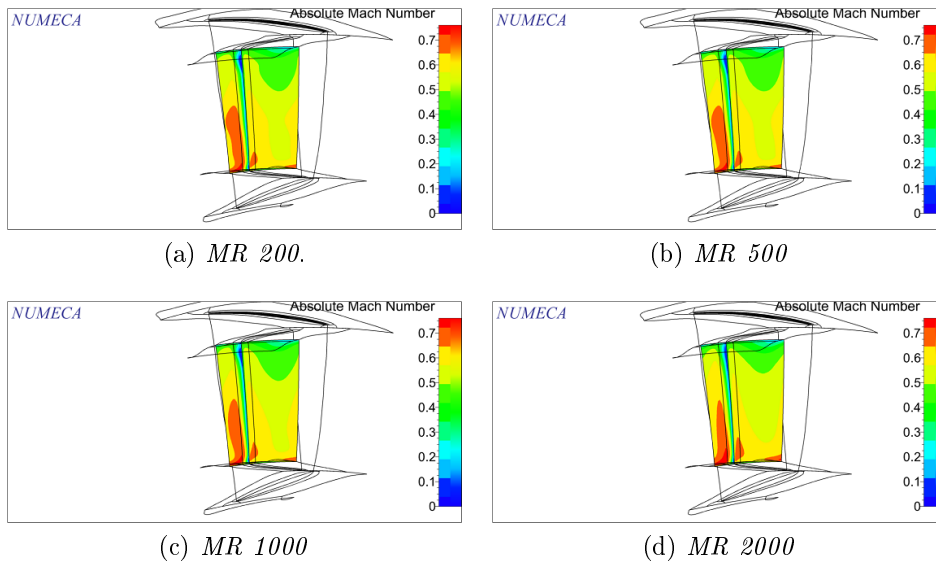


Figure 5.32: Absolute Mach - Stator

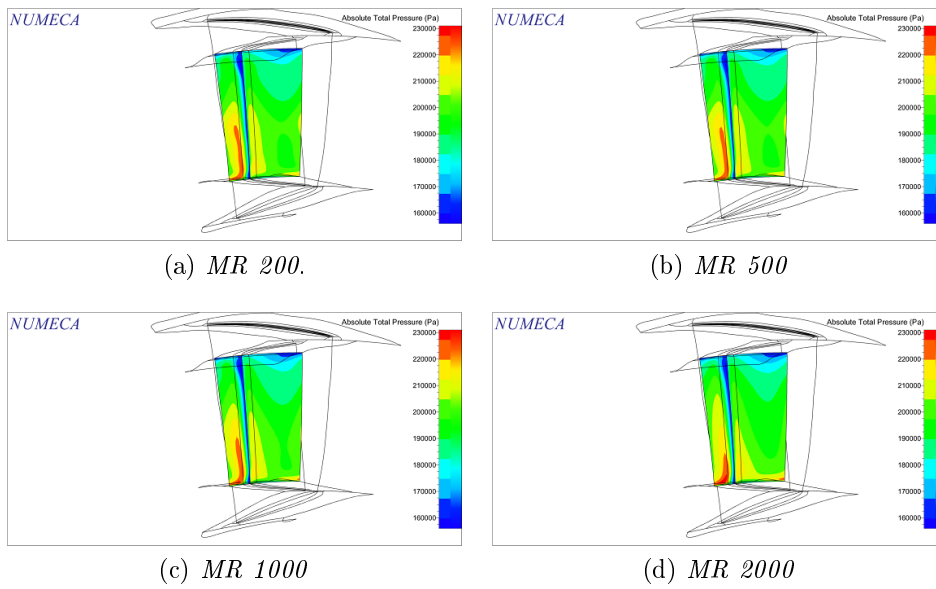


Figure 5.33: Absolute Pressure Ratio - Stator

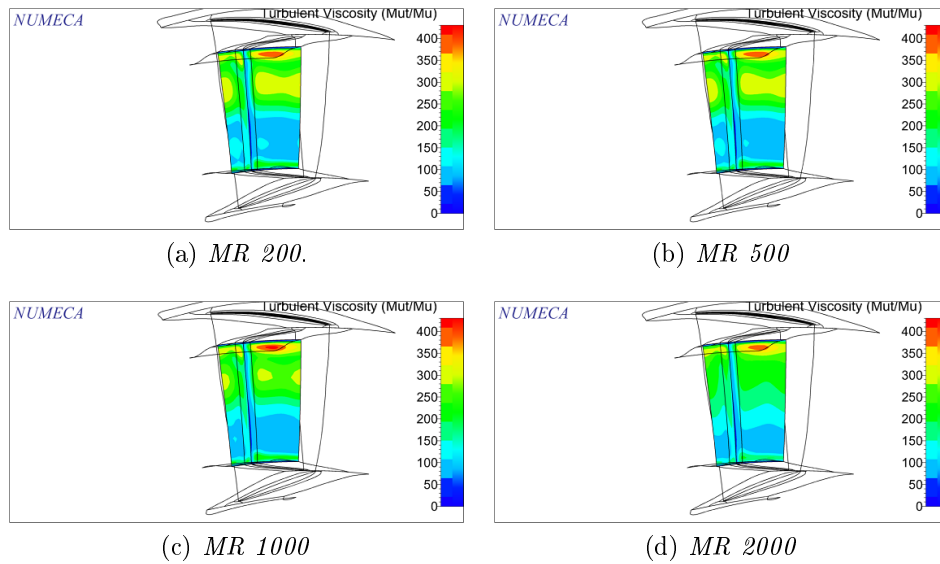


Figure 5.34: Turbulent Viscosity - Stator

Observations:

- Increasing the meshes elements increase the area with higher Absolute Mach number.
- Increasing the meshes elements increase the area with higher Absolute Pressure Ratio.
- Increasing the meshes elements increase the area with higher Turbulent Viscosity.

*Stall Point*

The differences between MR200-500 and MR1000 are still evident in this study. The former are very similar to each other in every analysis. MR 500 is chosen.

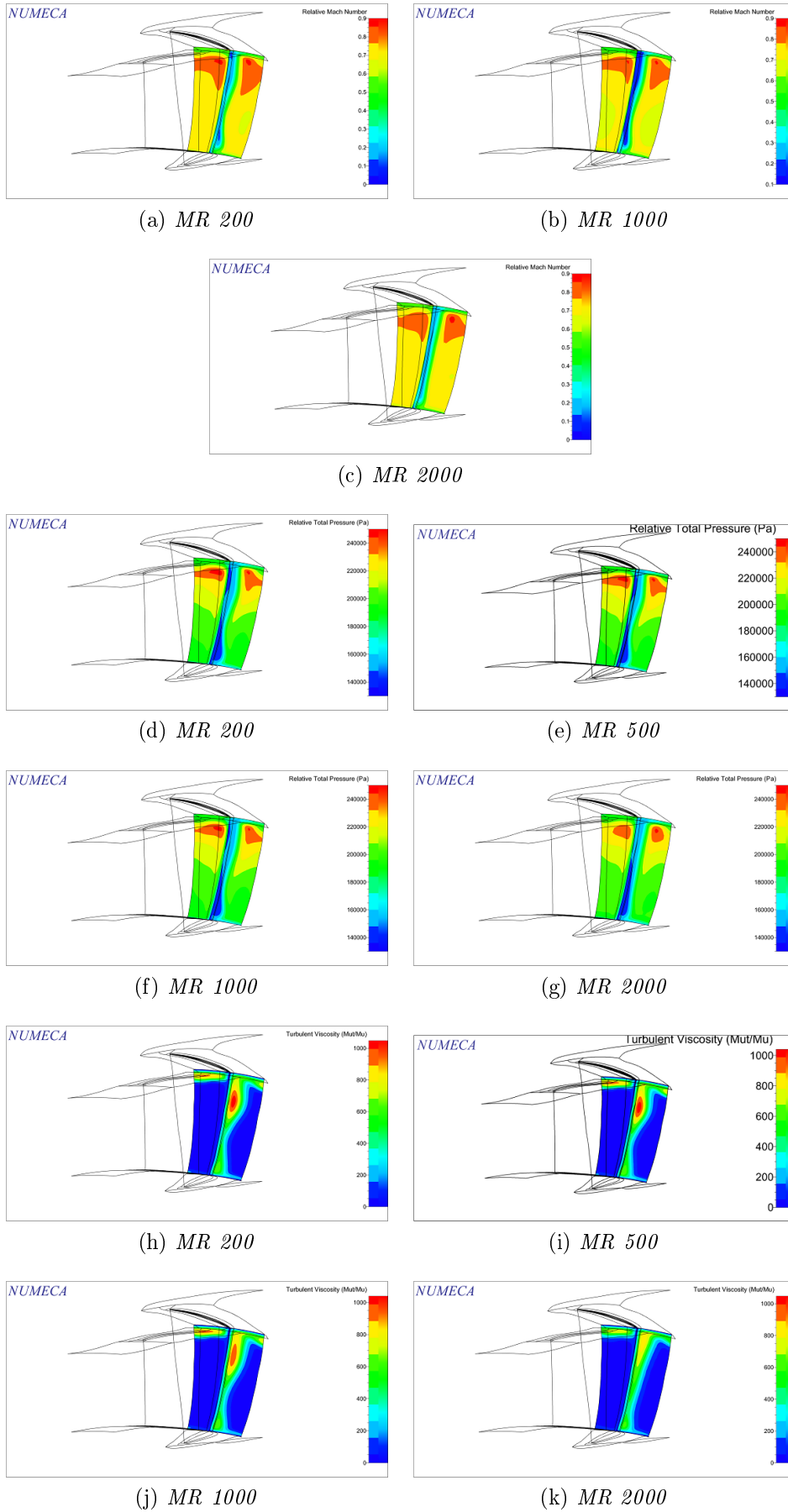


Figure 5.35: Rotor

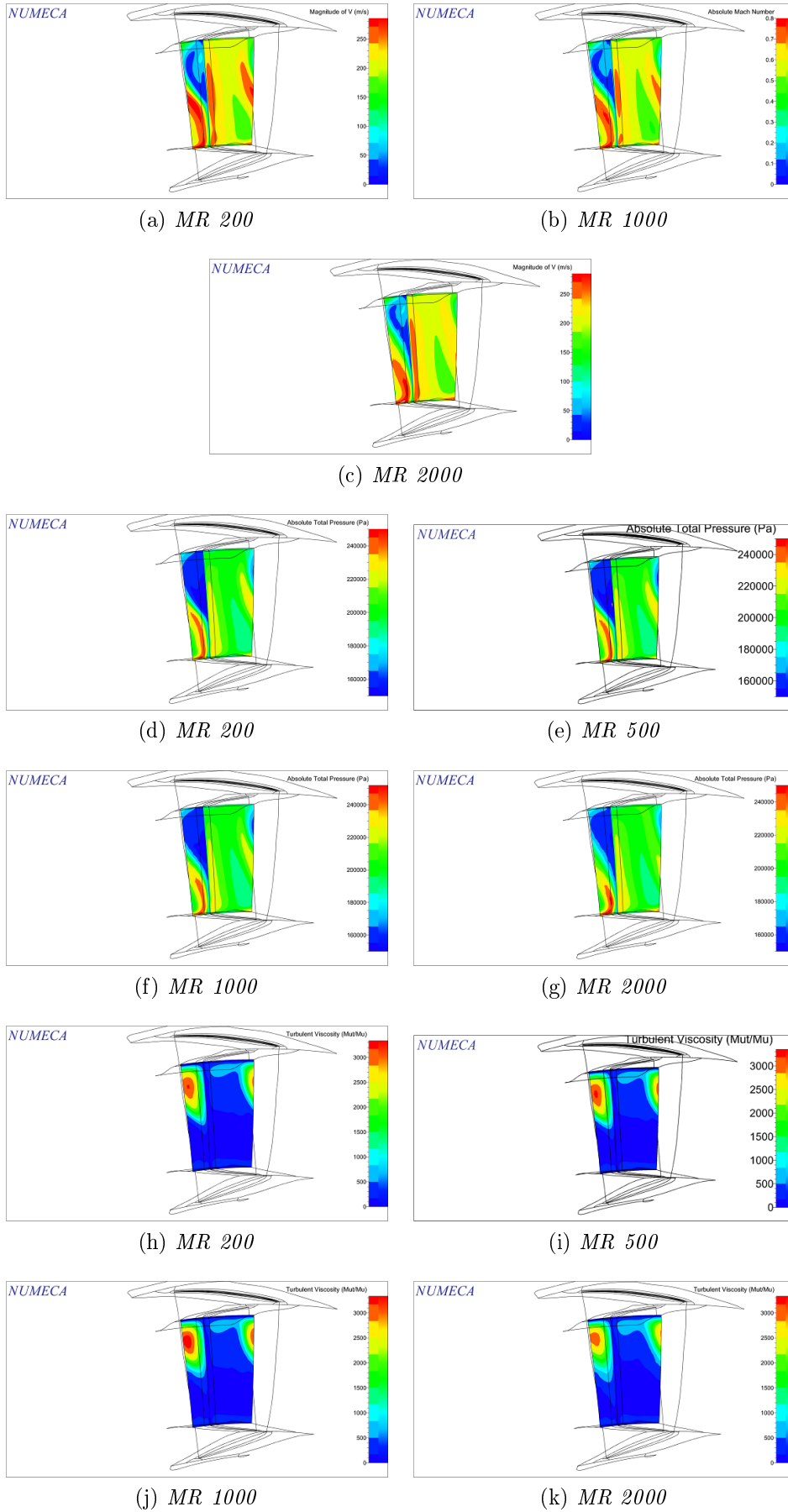


Figure 5.36: Stator

### 5.4.3 $y^+$ influence

*Point of Max Efficiency*

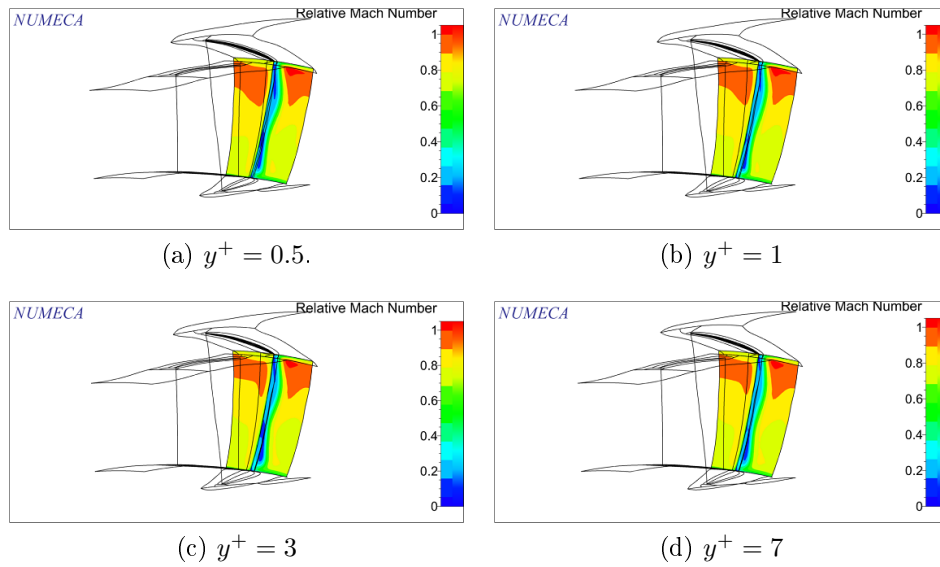


Figure 5.37: Relative Mach - Rotor

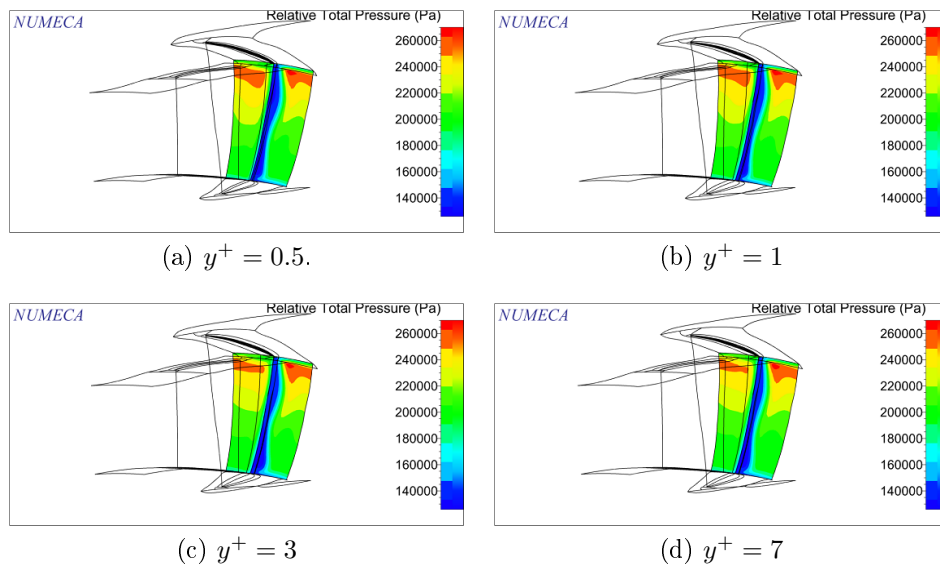


Figure 5.38: Relative Pressure Ratio - Rotor

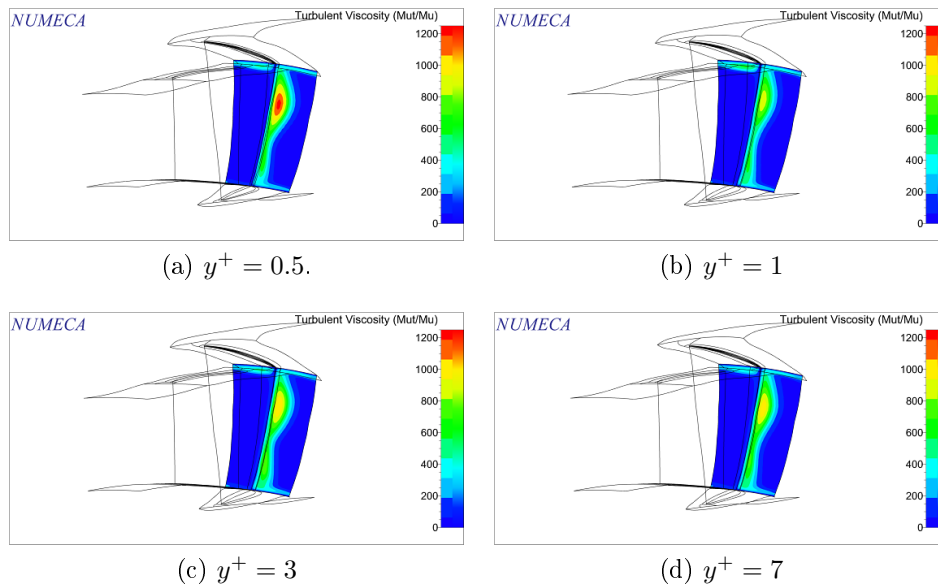


Figure 5.39: Turbulent Viscosity - Rotor

Observations:

- Increasing the meshes elements increase the area with higher Relative Mach number.
- Increasing the meshes elements increase the area with higher Relative Pressure Ratio.
- Increasing the meshes elements increase the area with higher Turbulent Viscosity.

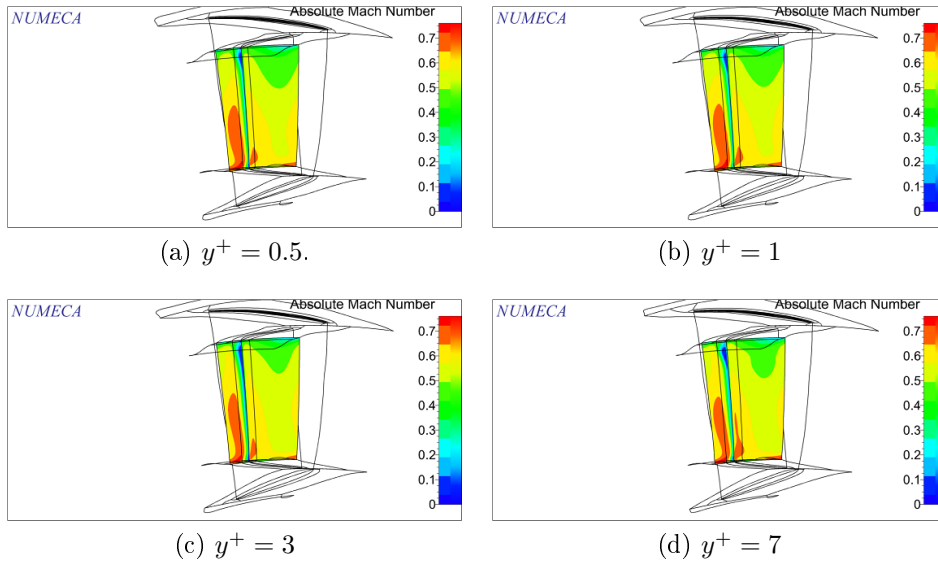


Figure 5.40: Absolute Mach - Stator

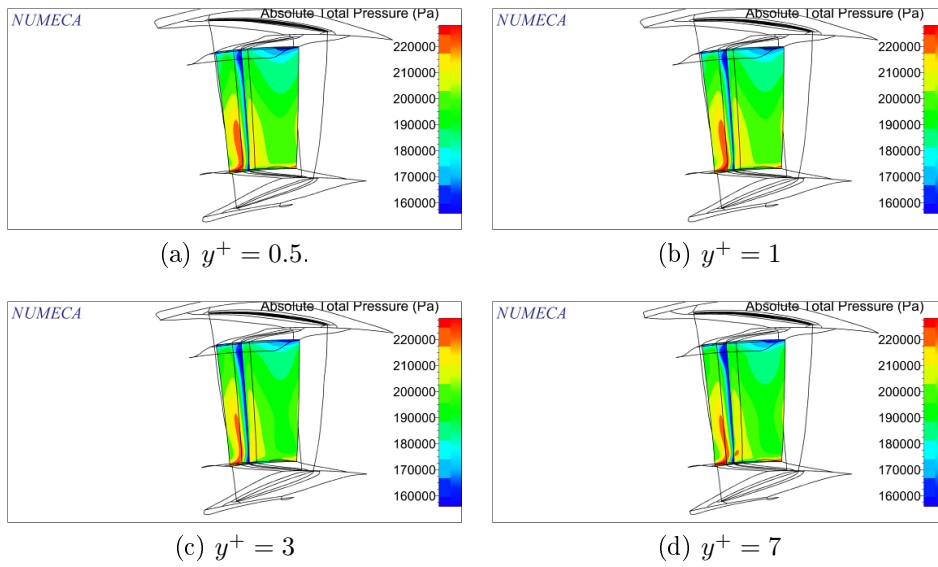


Figure 5.41: Absolute Pressure - Stator

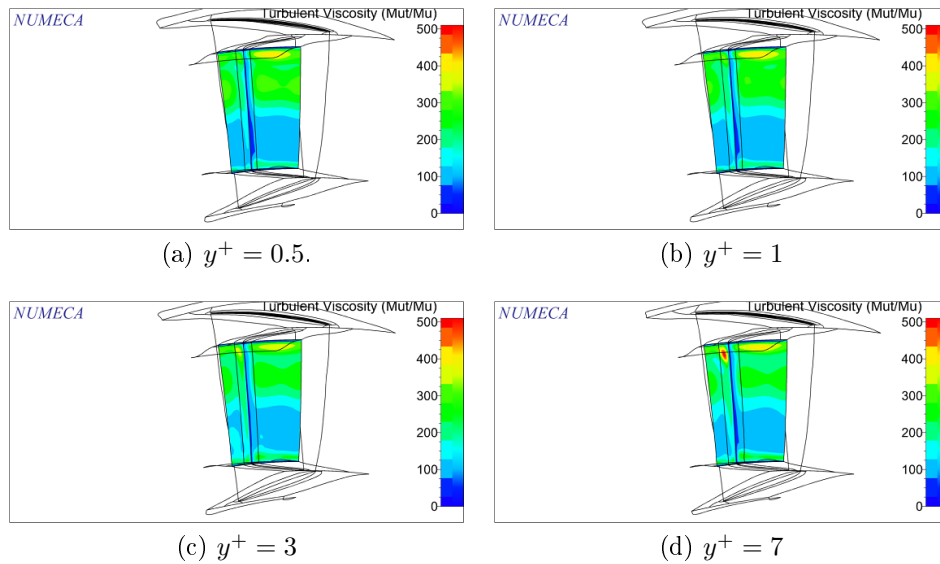


Figure 5.42: Turbulent Viscosity - Stator

Observations:

- Increasing the meshes elements increase the area with higher Absolute Mach number.
- Increasing the meshes elements increase the area with higher Absolute Pressure Ratio.
- Increasing the meshes elements decrease the area with higher Turbulent Viscosity.

*Stall Point*

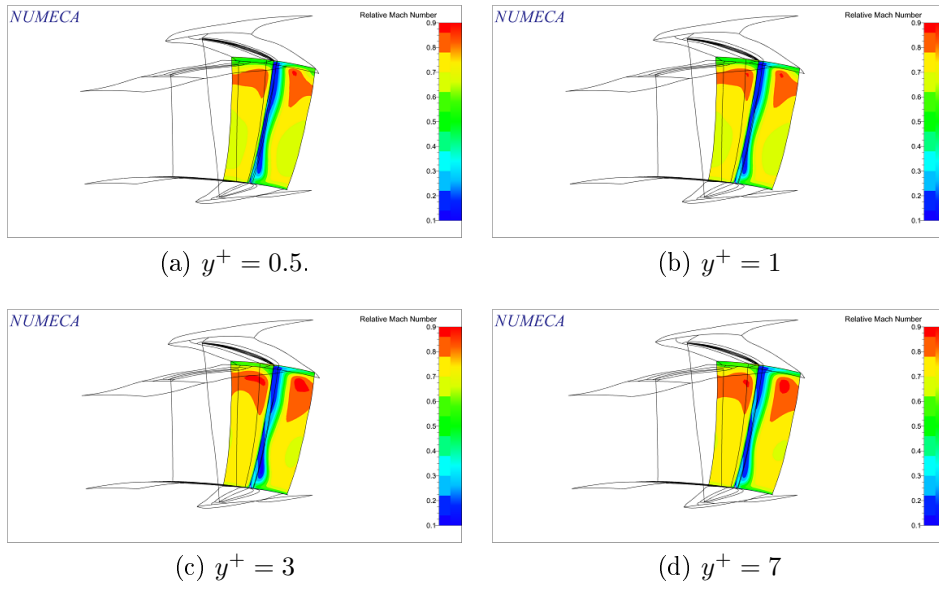


Figure 5.43: Relative Mach - Rotor

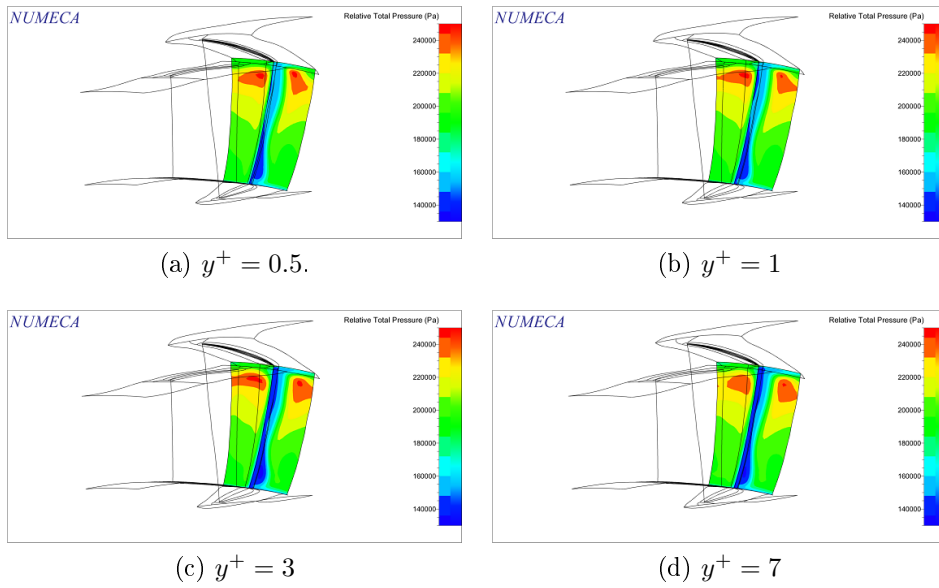


Figure 5.44: Relative Pressure Ratio - Rotor

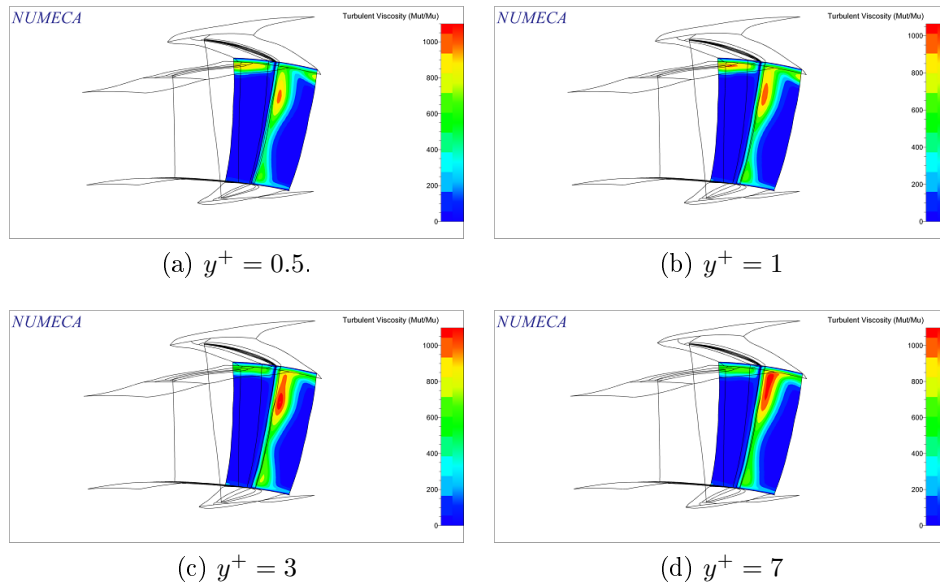


Figure 5.45: Turbulent Viscosity - Rotor

Observations:

- Increasing the meshes elements decrease the area with higher Relative Mach number.
- The area with higher Relative Pressure Ratio changes shape but not dimension.
- Increasing the meshes elements decrease the area with higher Turbulent Viscosity.

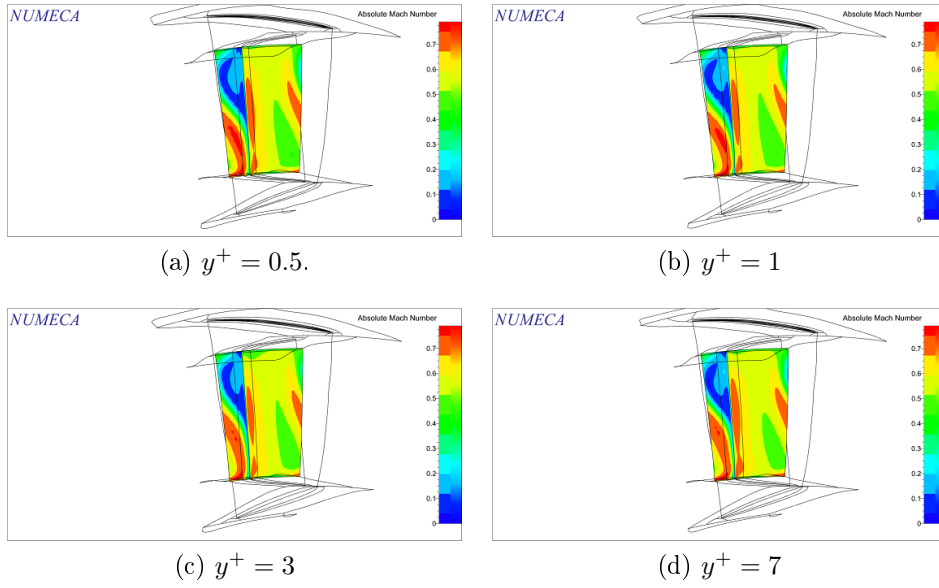


Figure 5.46: Absolute Mach - Stator

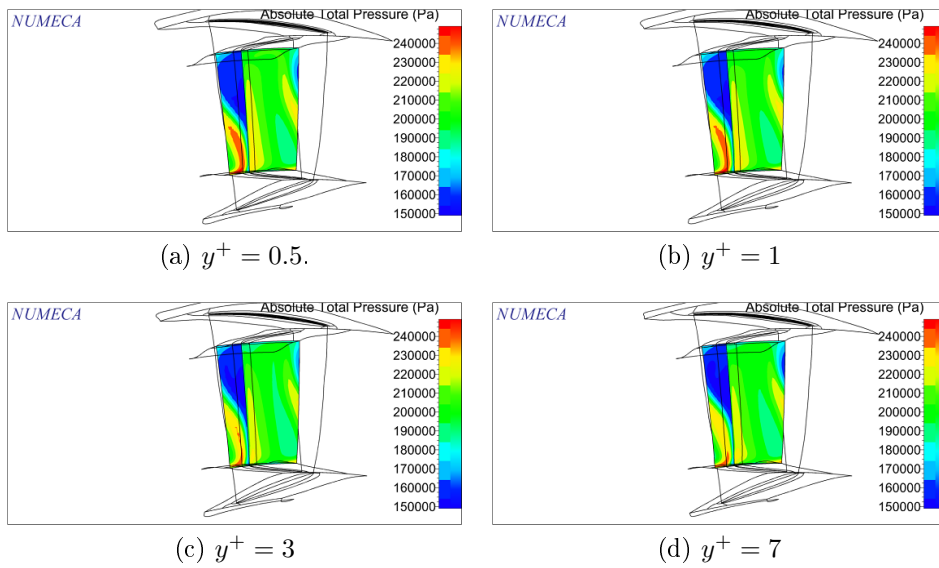


Figure 5.47: Absolute Pressure - Stator

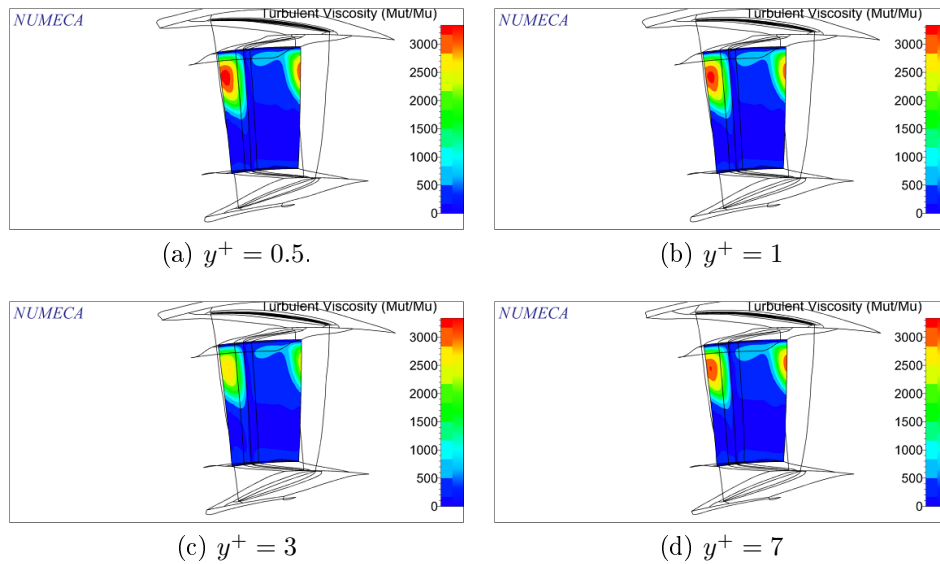


Figure 5.48: Turbulent Viscosity - Stator

Observations:

- Increasing the meshes elements increase the area with higher Absolute Mach number.
- Increasing the meshes elements increase the area with higher Absolute Pressure Ratio.
- Increasing the meshes elements increase the area with higher Turbulent Viscosity.

$y^+ = 0.5$  and  $y^+ = 1$  have similar behavior but the former used a greater number of elements.  $y^+ = 1$  is chosen.

### 5.4.4 Expansion Ratio influence, Blade to Blade

The flow visualizations in plane parallel to x-y are not reported because there are not differences between the meshes.

*Point of Max Efficiency*

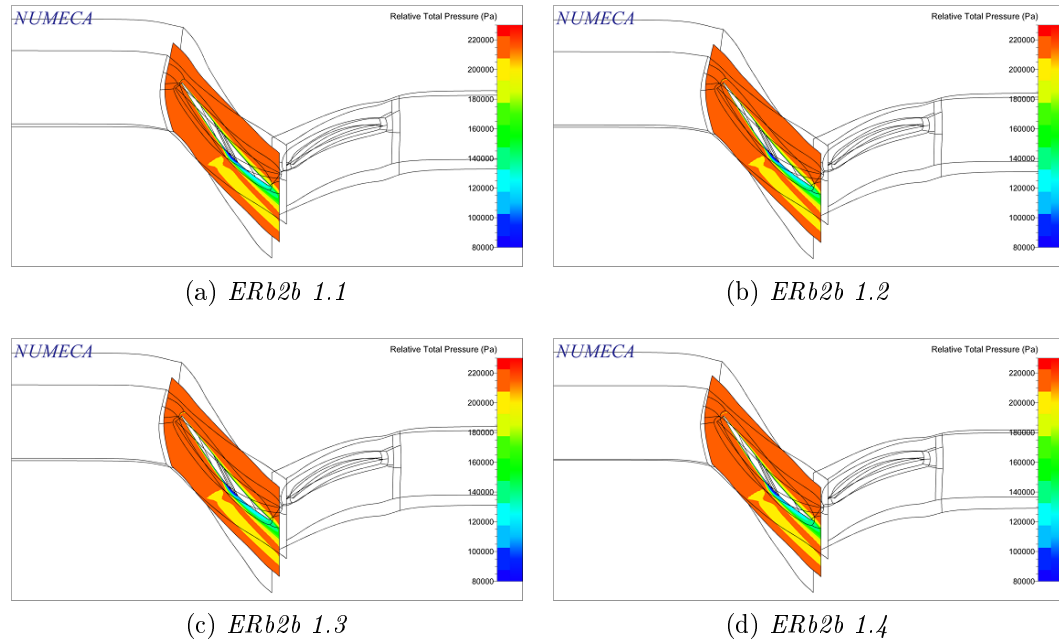


Figure 5.49: Relative Pressure Ratio - Rotor

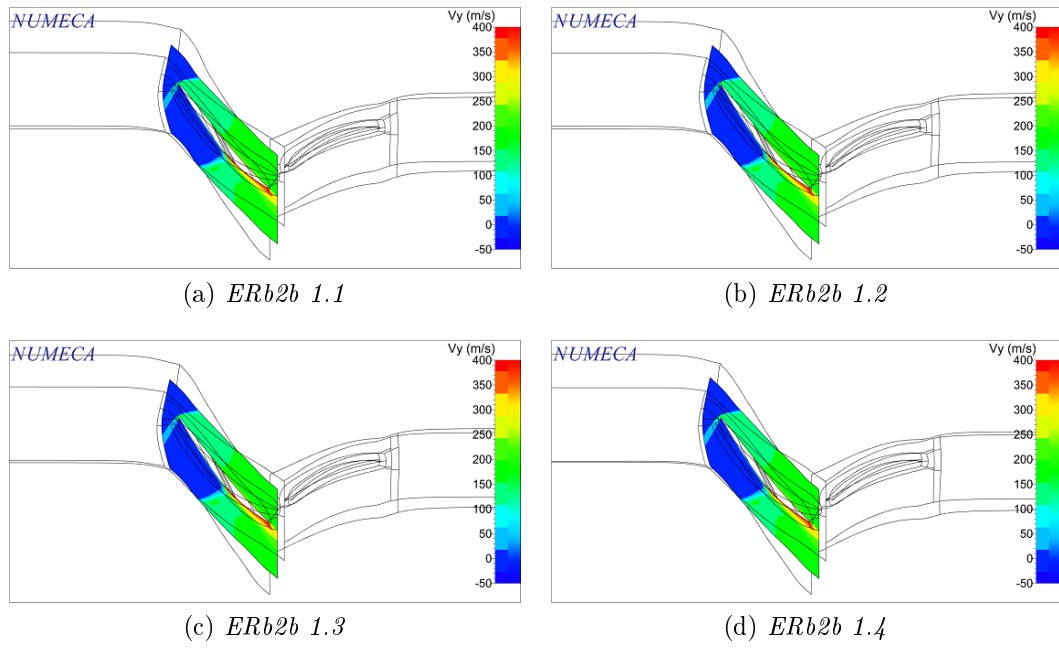


Figure 5.50:  $V_y$  - Rotor

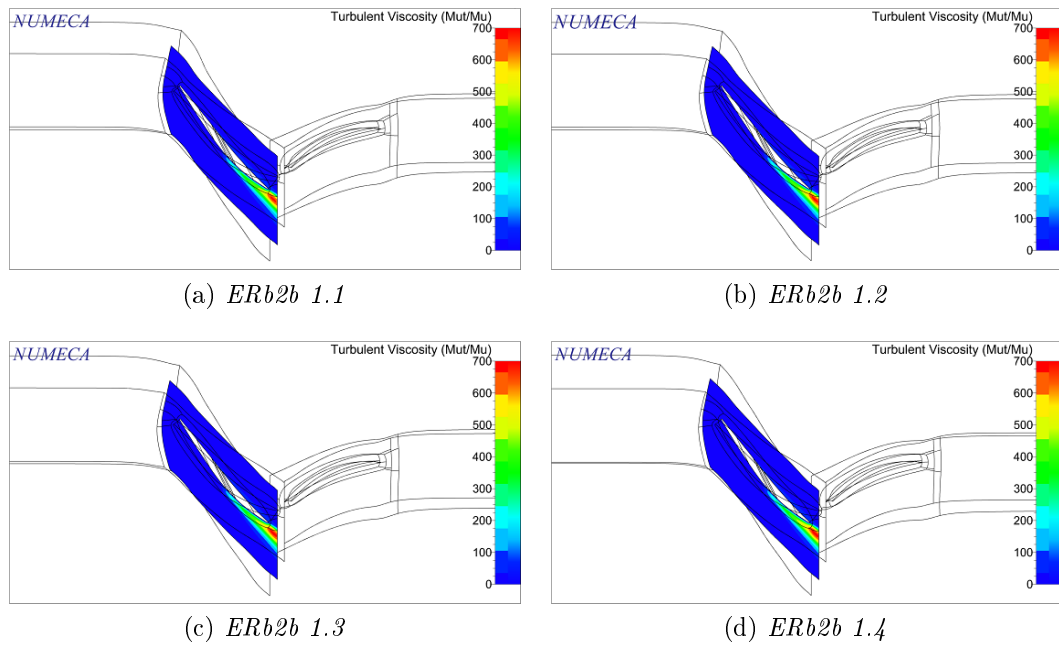


Figure 5.51: Turbulent Viscosity - Rotor

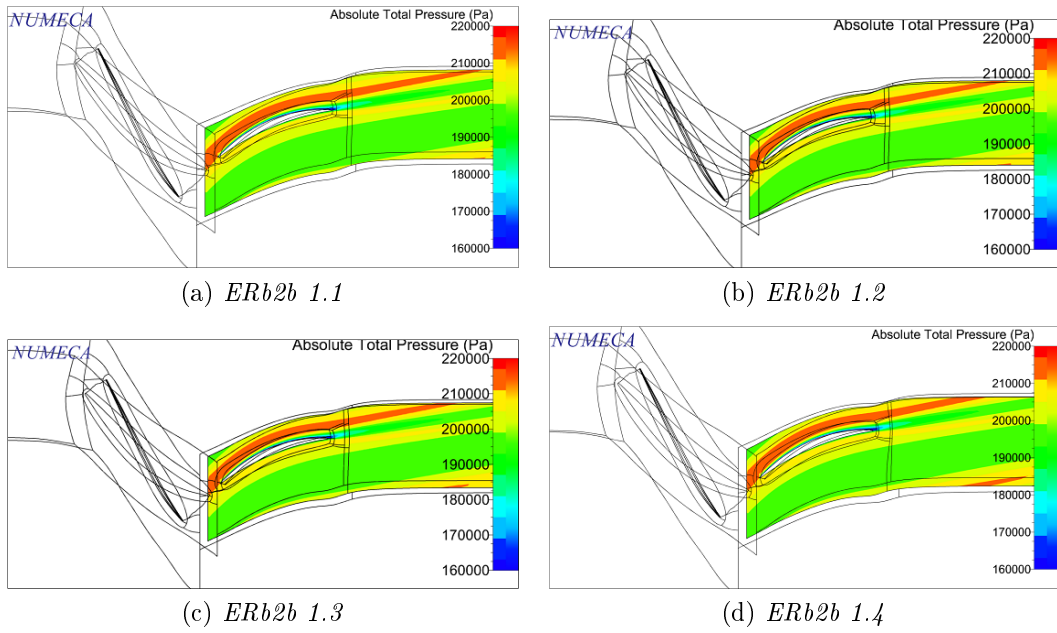


Figure 5.52: Absolute Pressure Ratio - Stator

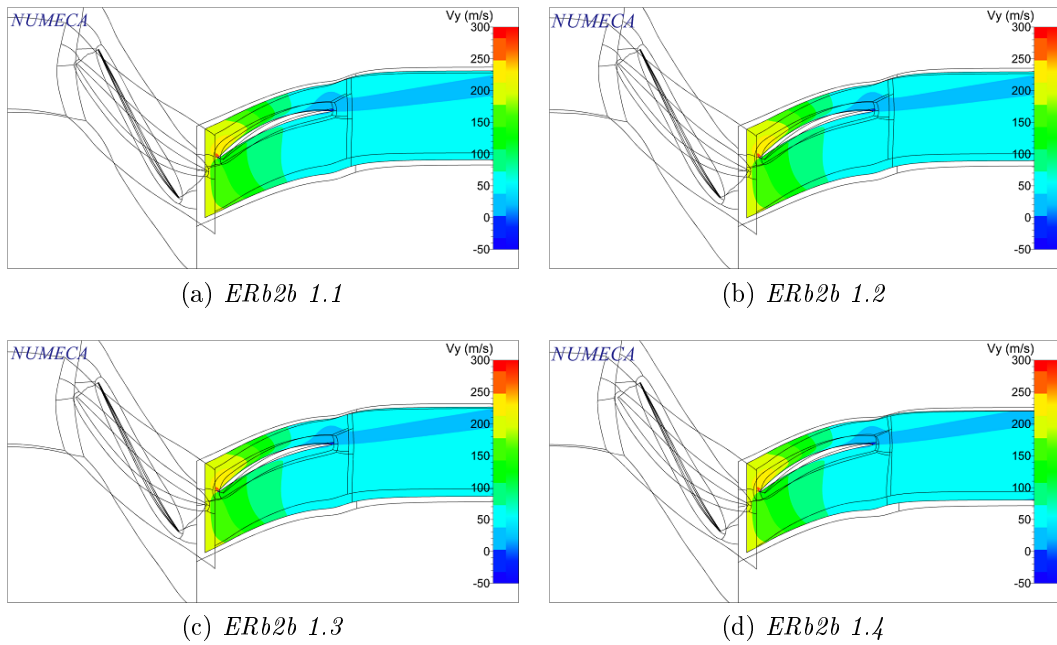


Figure 5.53:  $V_y$  - Stator

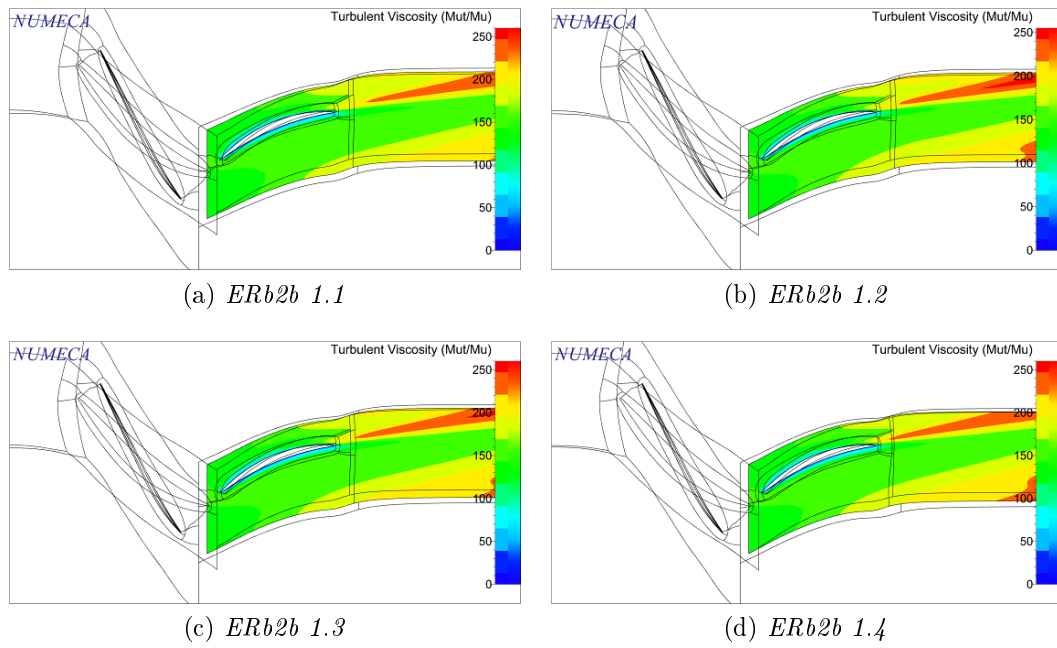


Figure 5.54: Turbulent Viscosity - Stator

It is possible to notice very small different only in Absolute Pressure Ratio and in Turbulent Viscosity on stator, the others graphs are exactly identical. *ERb2b 1.2* is chosen.

### 5.4.5 O layer influence

The flow visualizations in plane parallel to x-y are not reported because there are not differences between the meshes.

*Point of Max Efficiency*

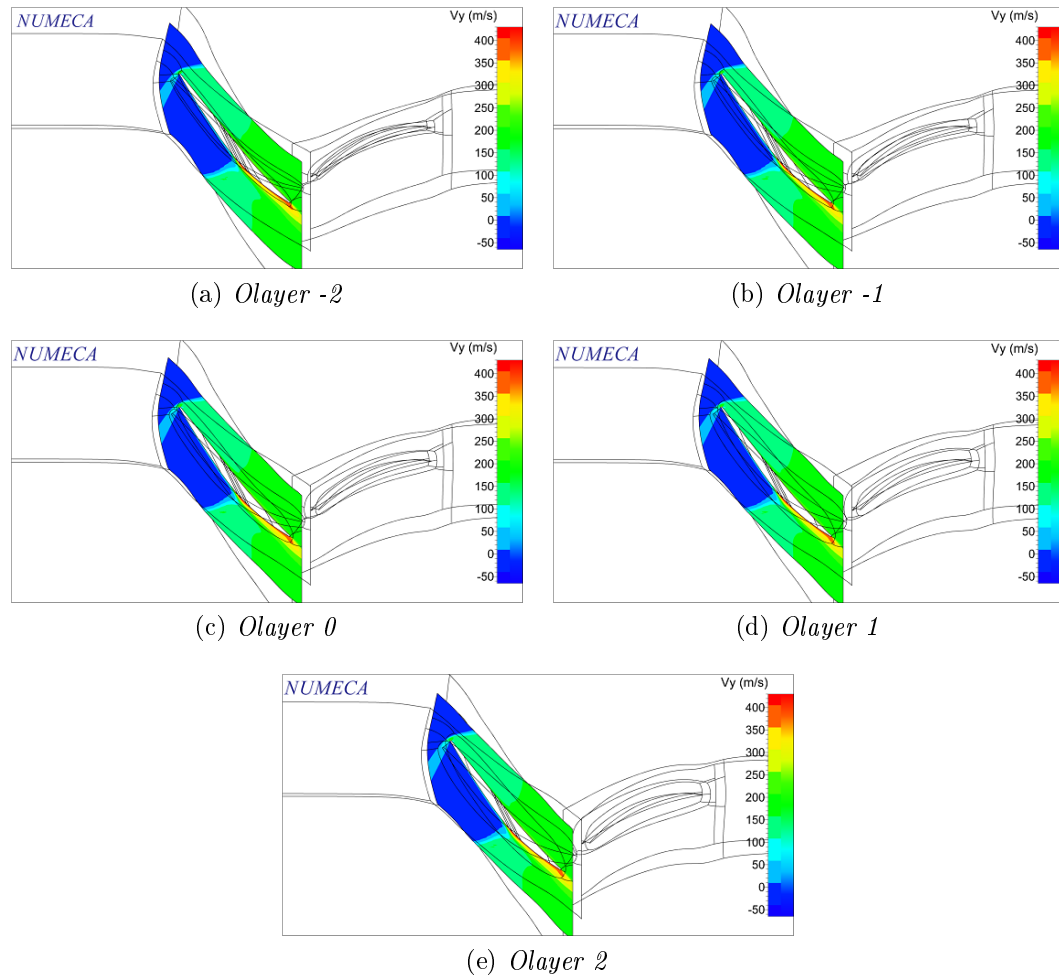


Figure 5.55:  $V_y$  - Rotor

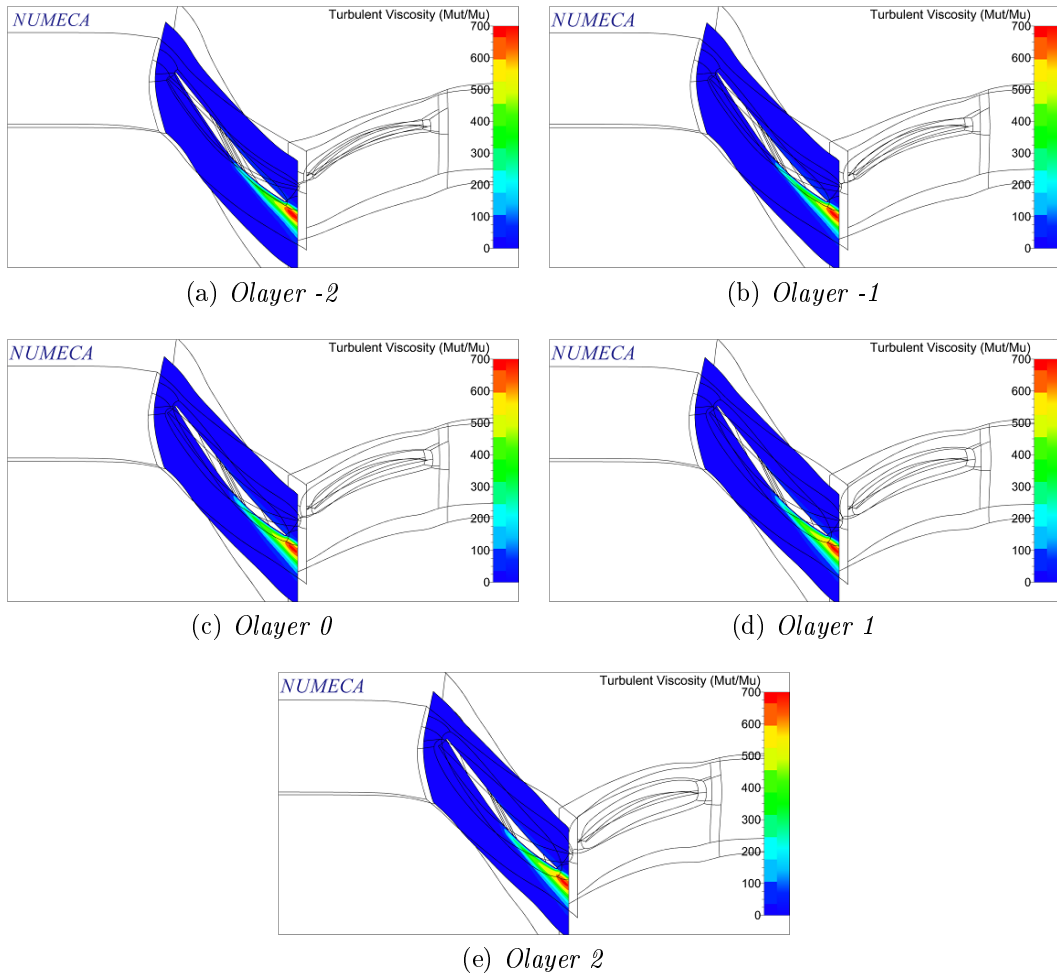


Figure 5.56: Turbulent Viscosity - Rotor

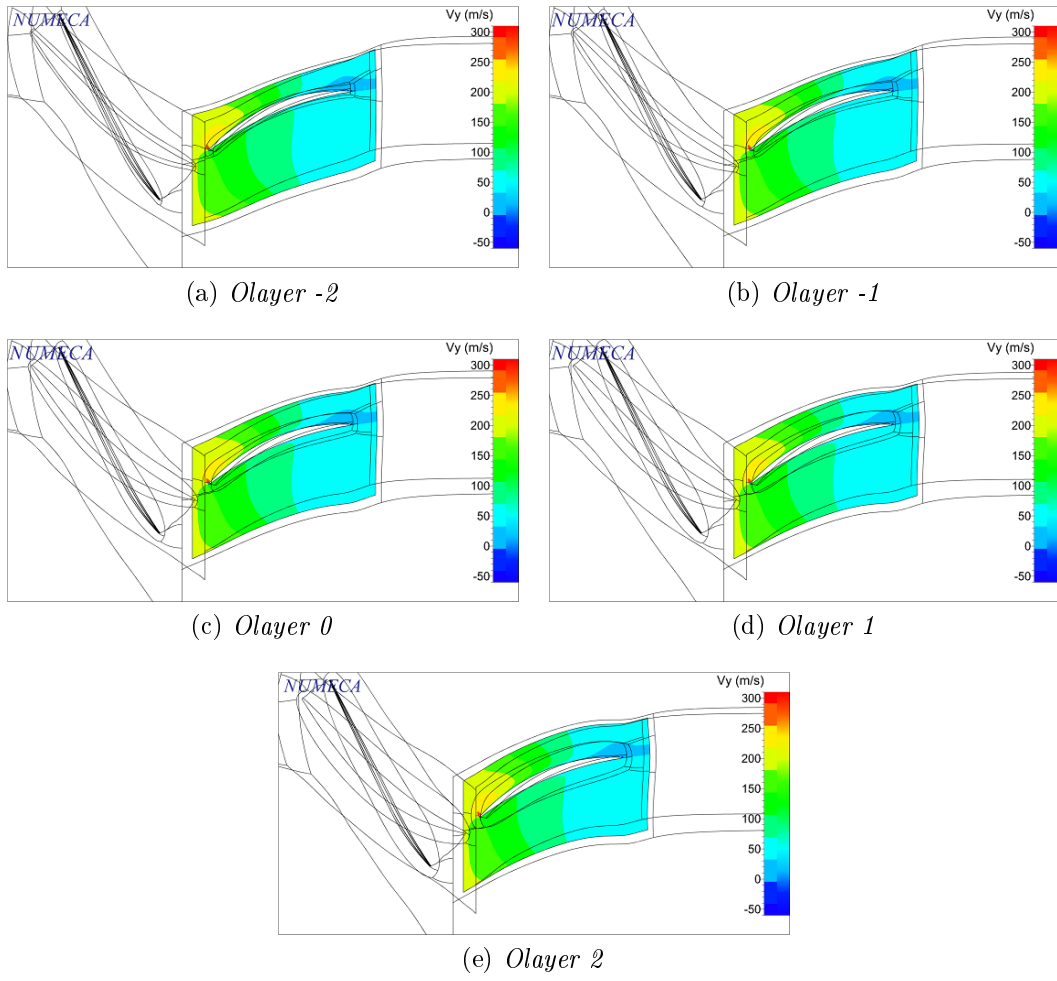


Figure 5.57:  $V_y$  - Stator

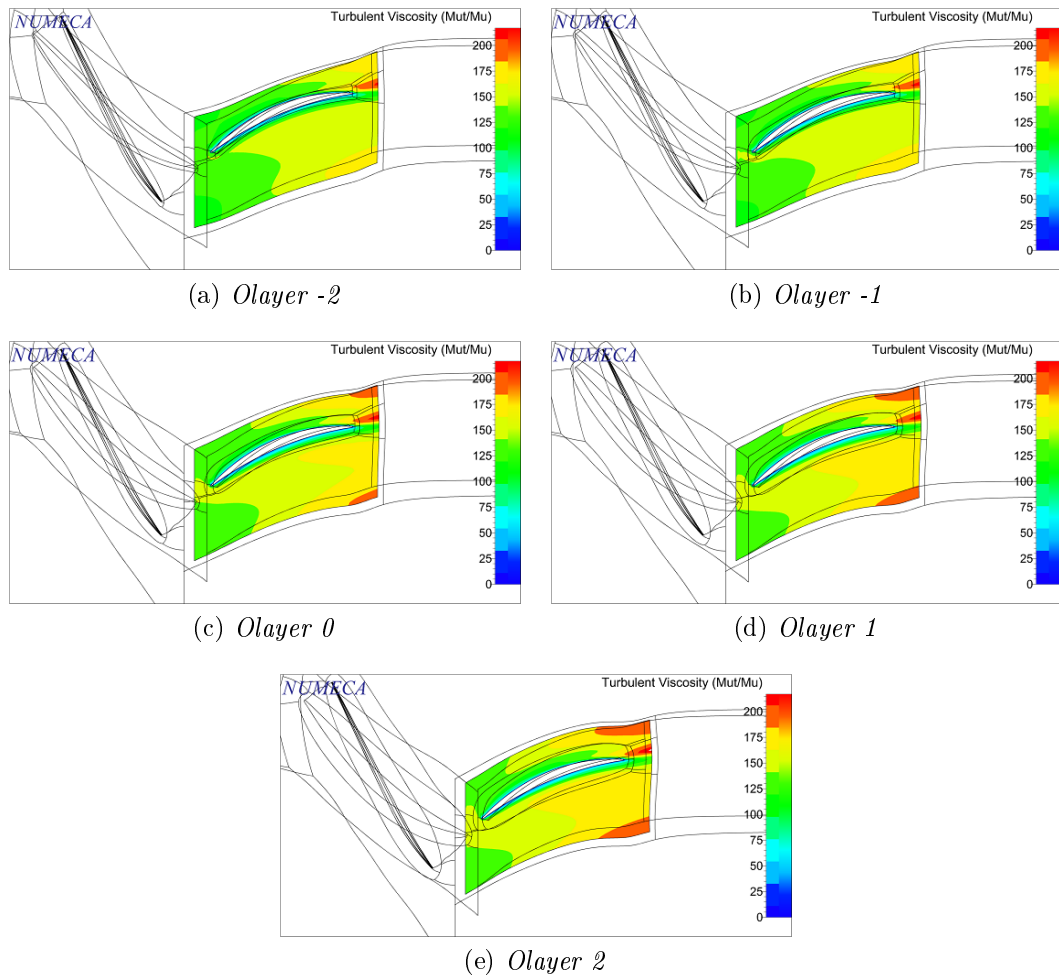


Figure 5.58: Turbulent Viscosity - Stator

The differences are not so evident but it is possible to notice a velocity and turbulent viscosity increase, increasing element number. O-layer 0 is chosen.

## 5.4.6 Mesh Density influence

*Point of Max Efficiency*

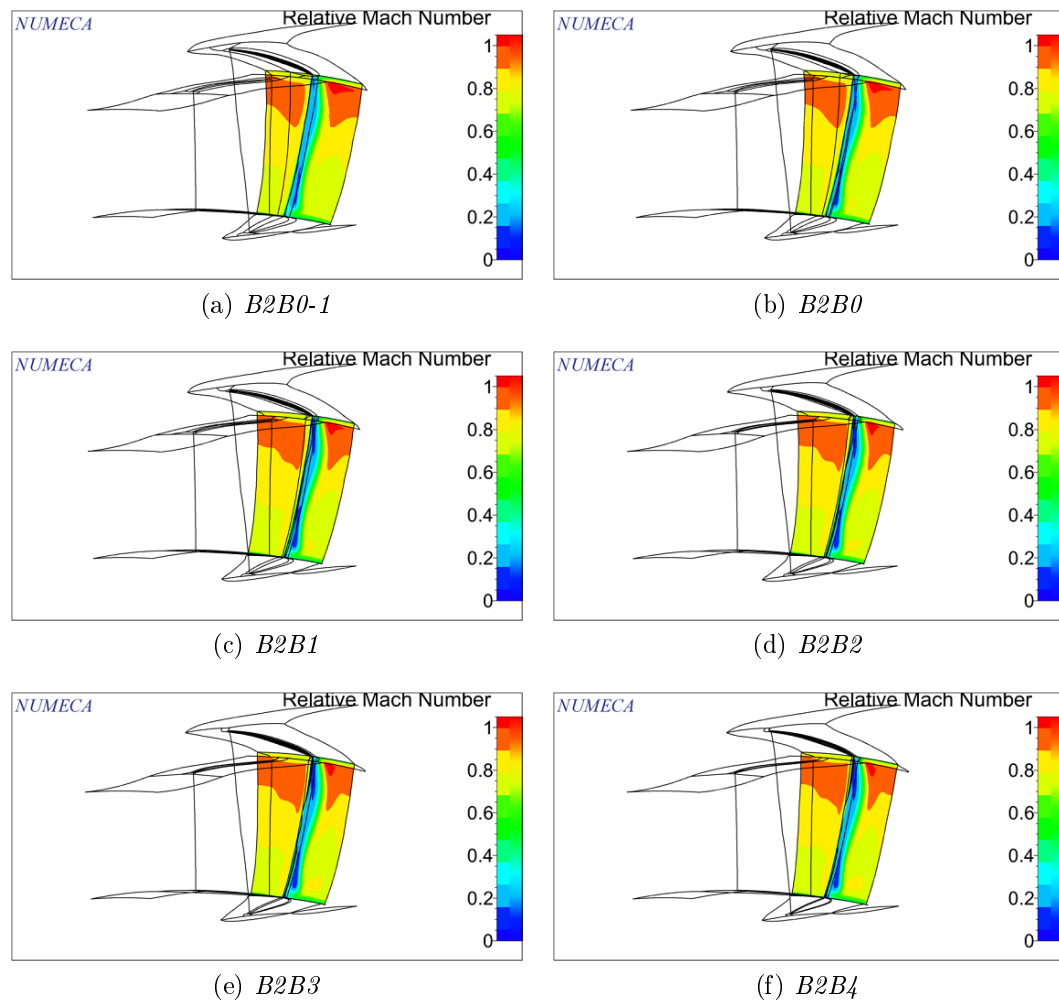


Figure 5.59: Relative Mach - Rotor

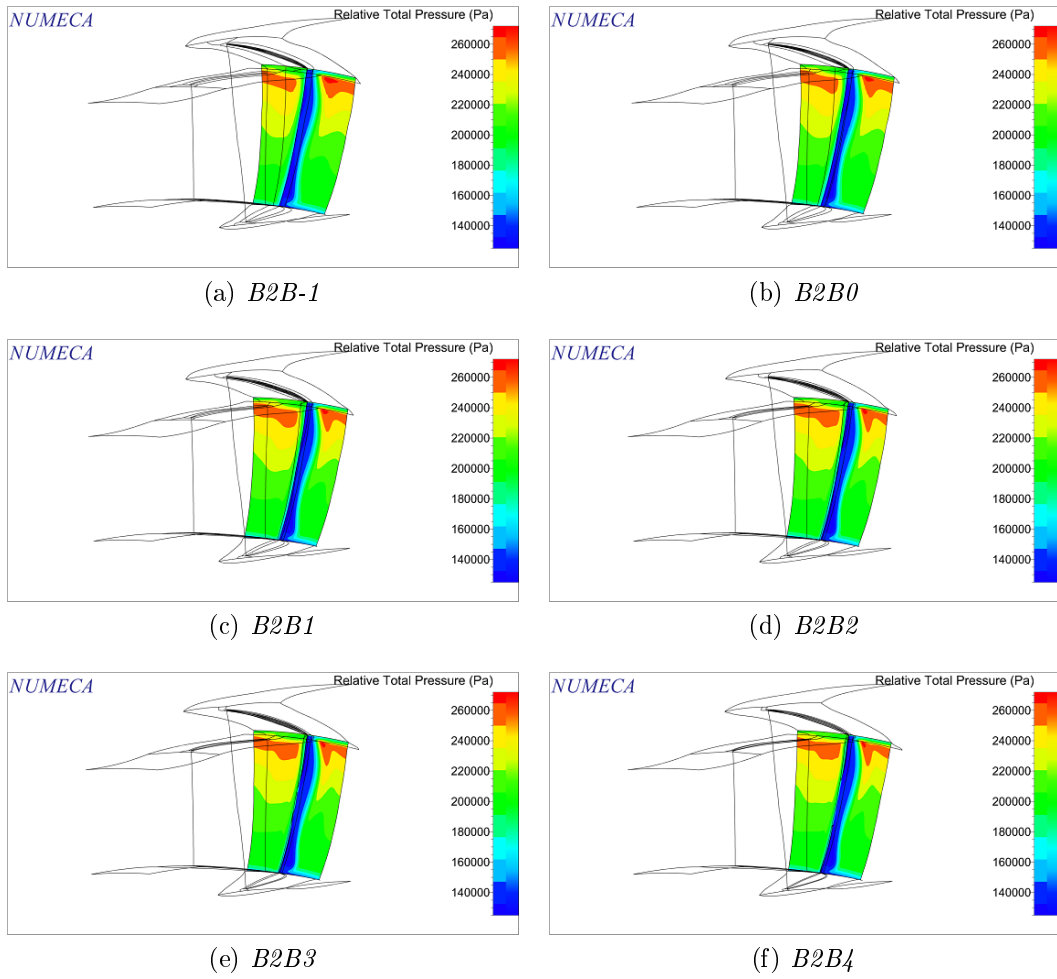


Figure 5.60: Relative Pressure Ratio - Rotor

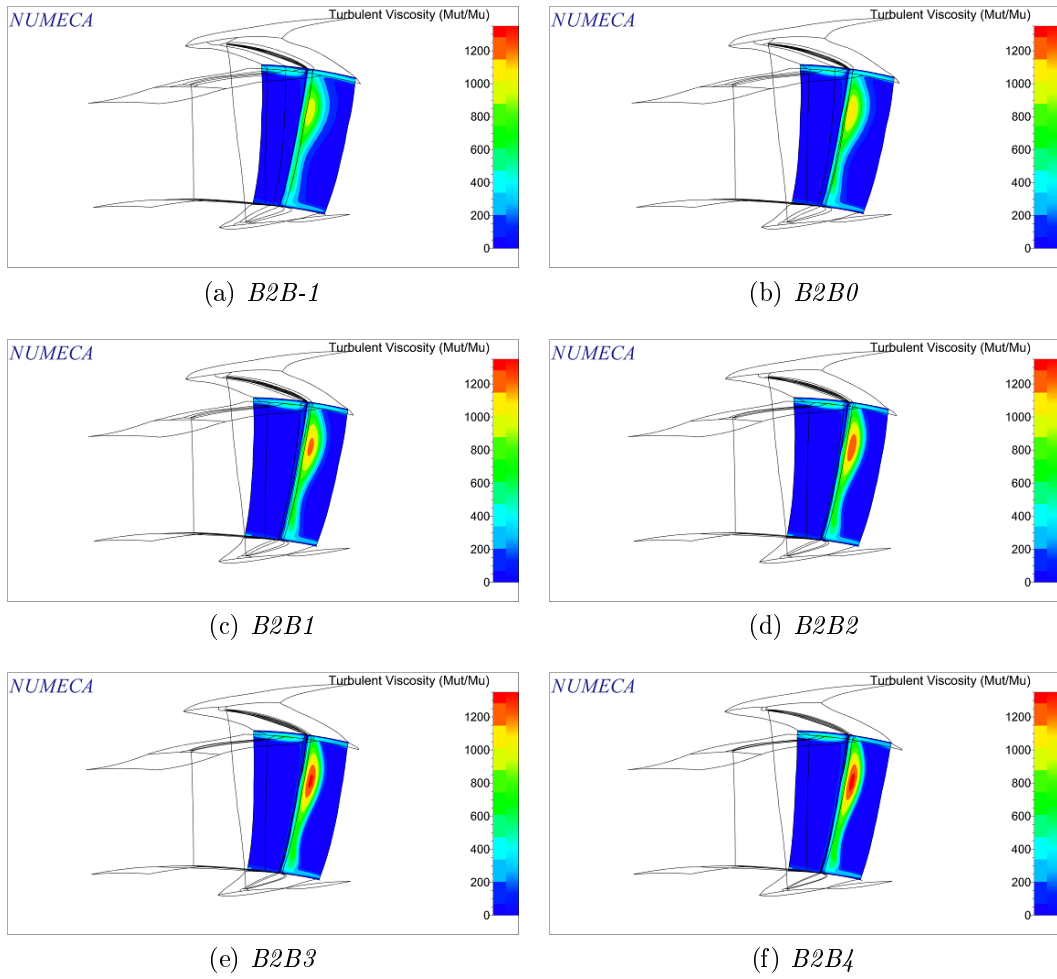


Figure 5.61: Turbulent Viscosity - Rotor

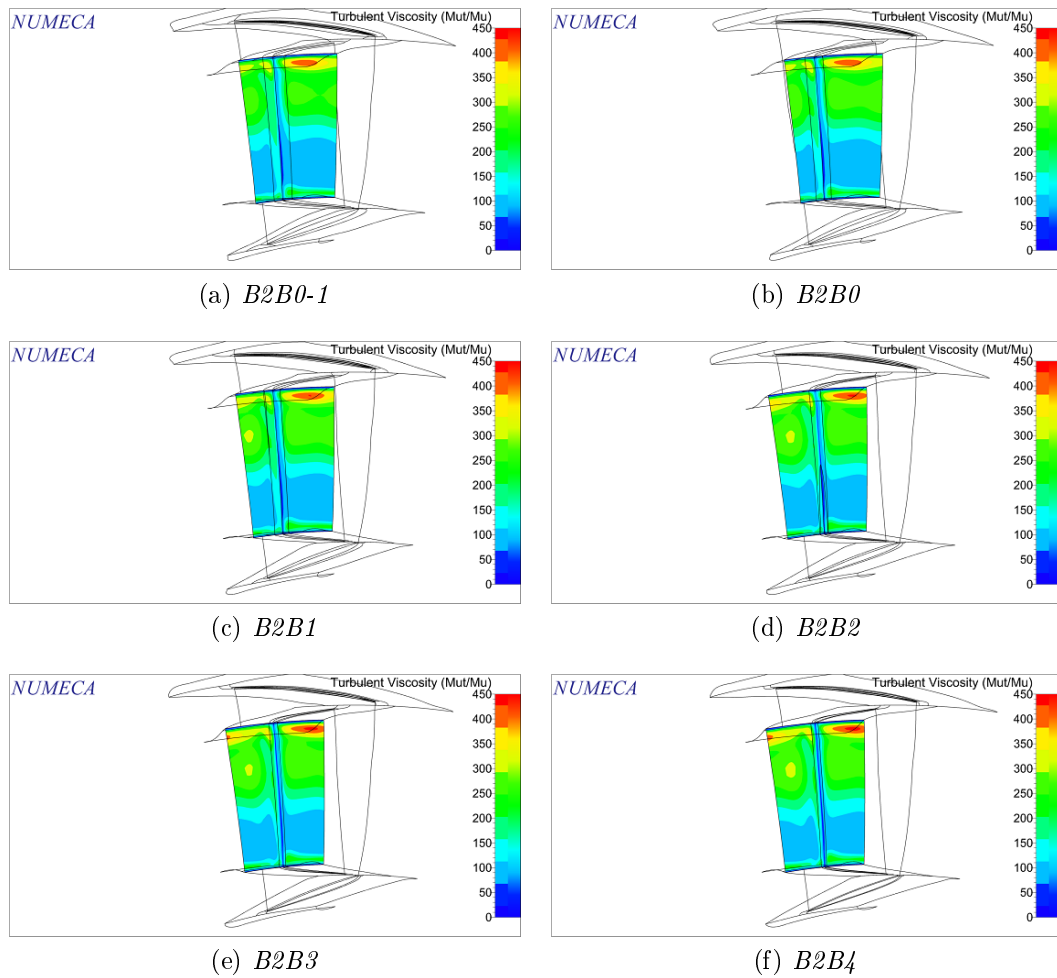


Figure 5.62: Turbulent Viscosity - Stator

Observations:

- Increasing the meshes elements the area with higher Relative Mach number changes shape, moving toward shroud and increase the value at the trailing edge.
- Increasing the meshes elements the area with higher Relative Pressure Ratio changes shape, moving toward shroud.
- Increasing the meshes elements increase the area with higher Turbulent Viscosity both for the stator and the rotor.

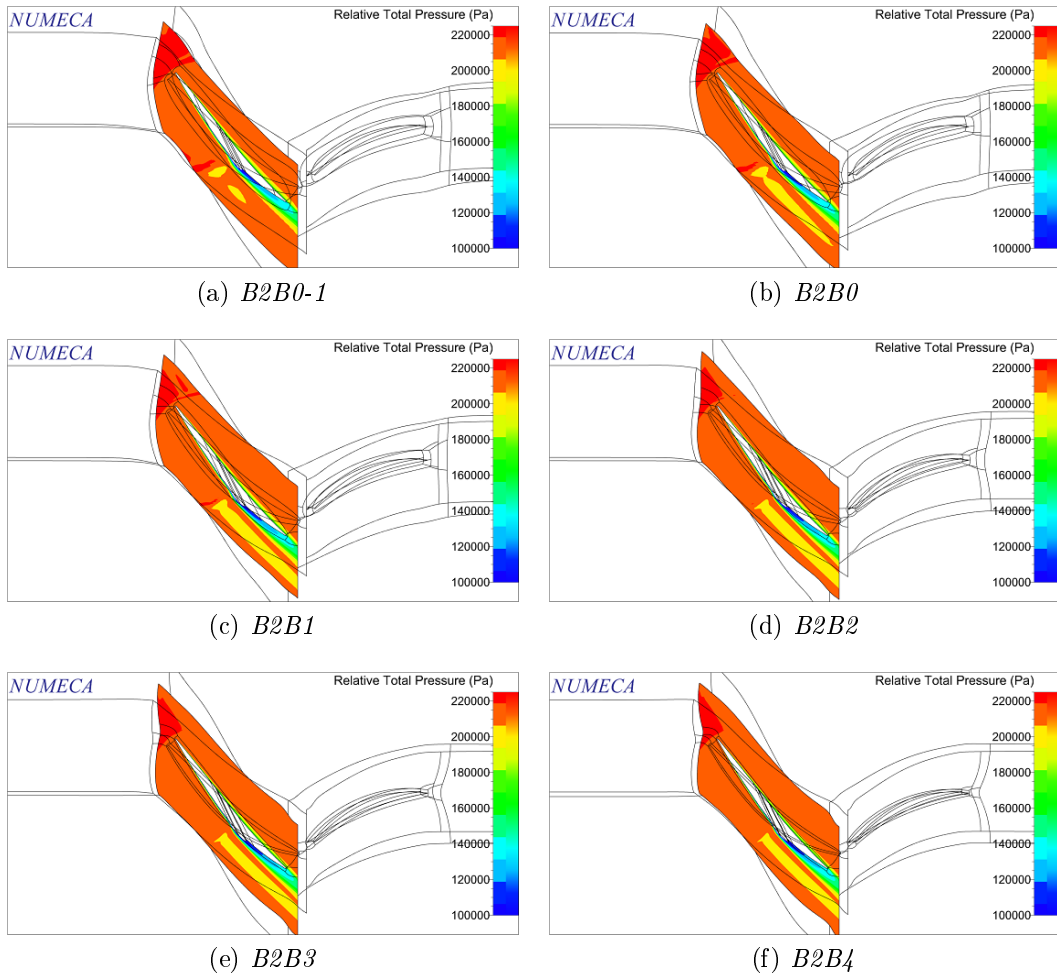


Figure 5.63: Relative Total Pressure - Rotor

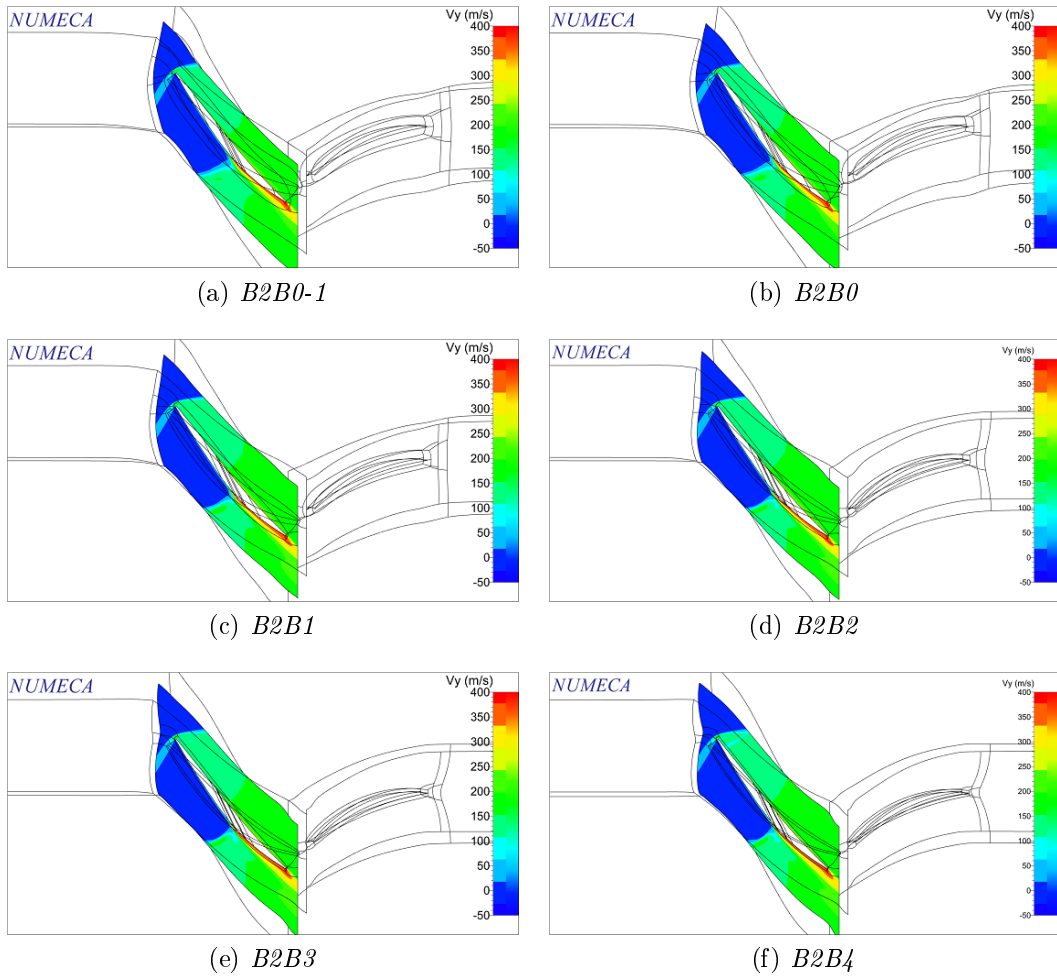


Figure 5.64:  $V_y$  - Rotor

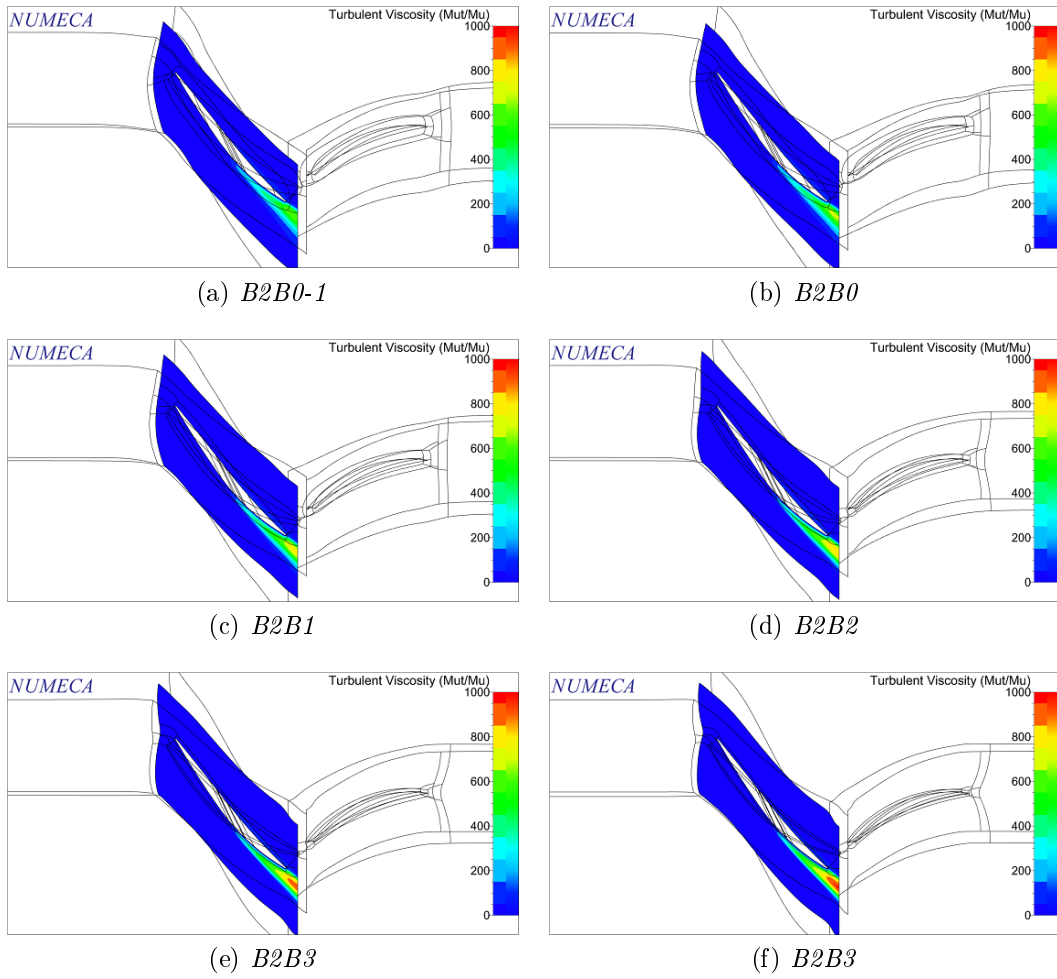


Figure 5.65: Turbulent Viscosity - Rotor

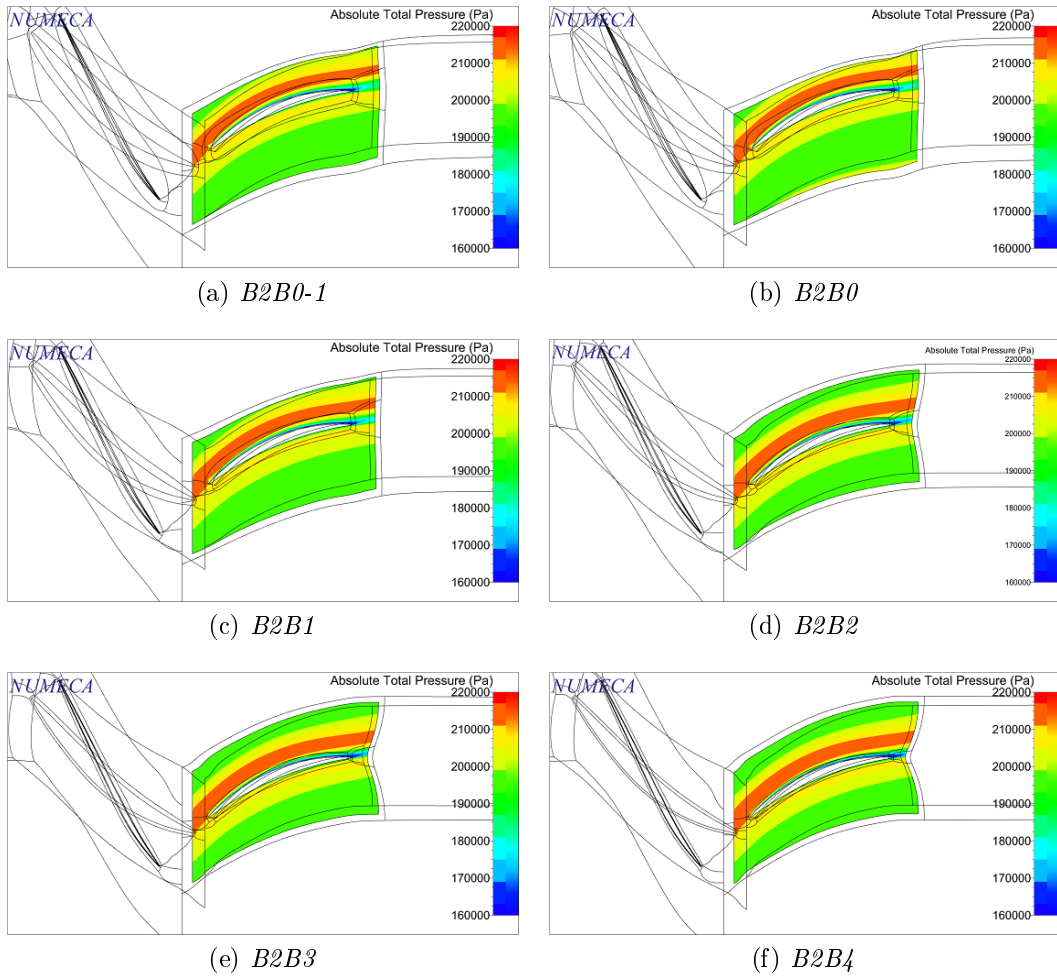


Figure 5.66: Absolute Total Pressure - Stator

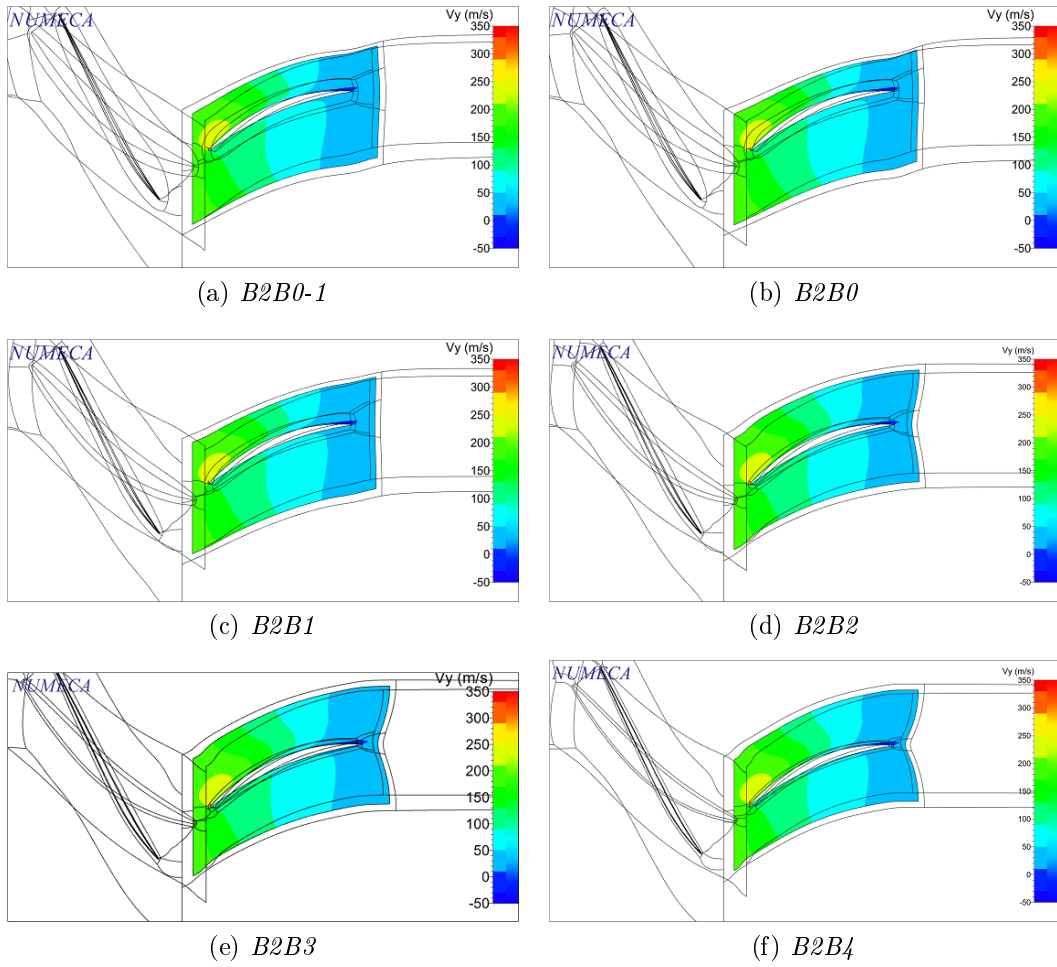


Figure 5.67:  $V_y$  - Stator

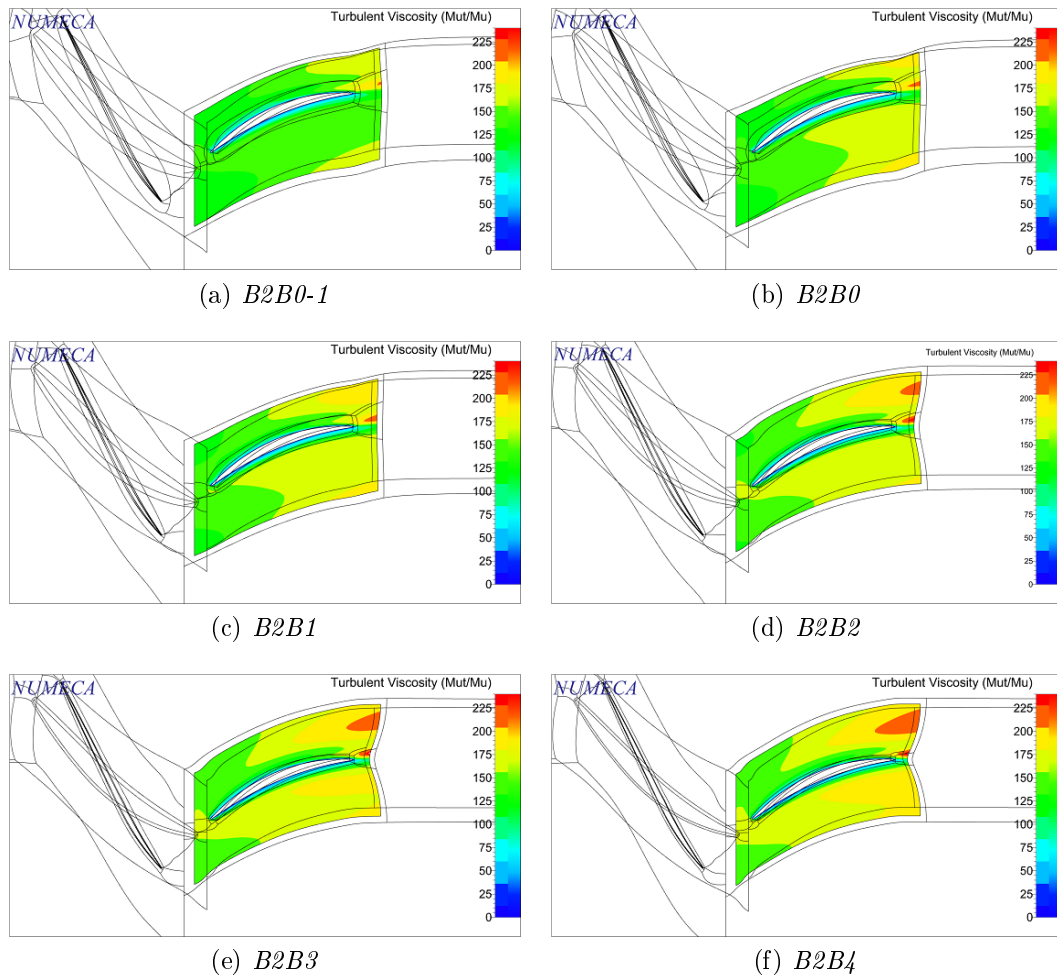


Figure 5.68: Turbulent Viscosity - Stator

Increasing number of element increase respectively the relative total pressure area and the turbulent viscosity in the rotor and the turbulent viscosity in the stator. In the other cases there are not evident differences. The mesh B2B2 is chosen.

## 5.4.7 Turbulence Models

*Max Efficiency Point*

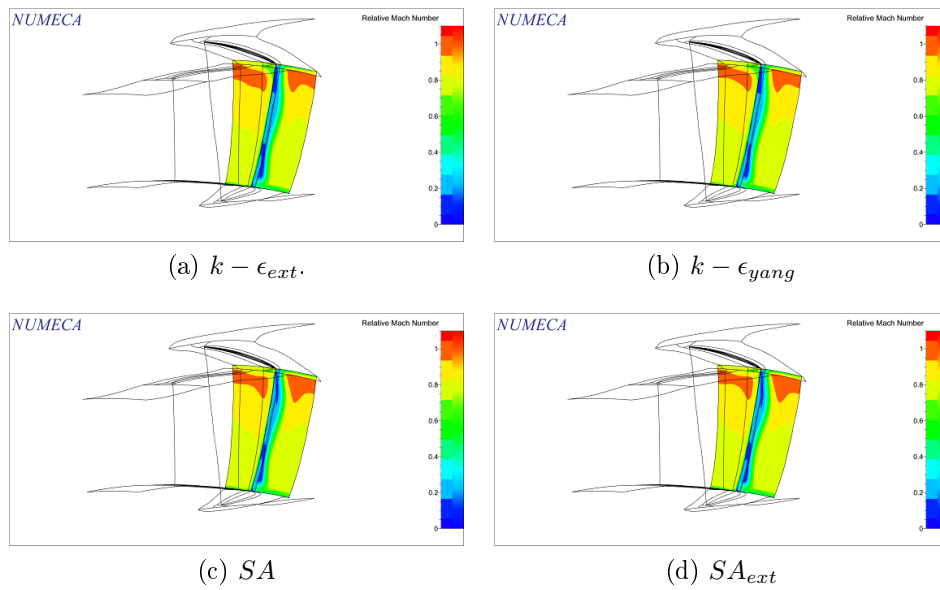


Figure 5.69: Relative Mach - Rotor

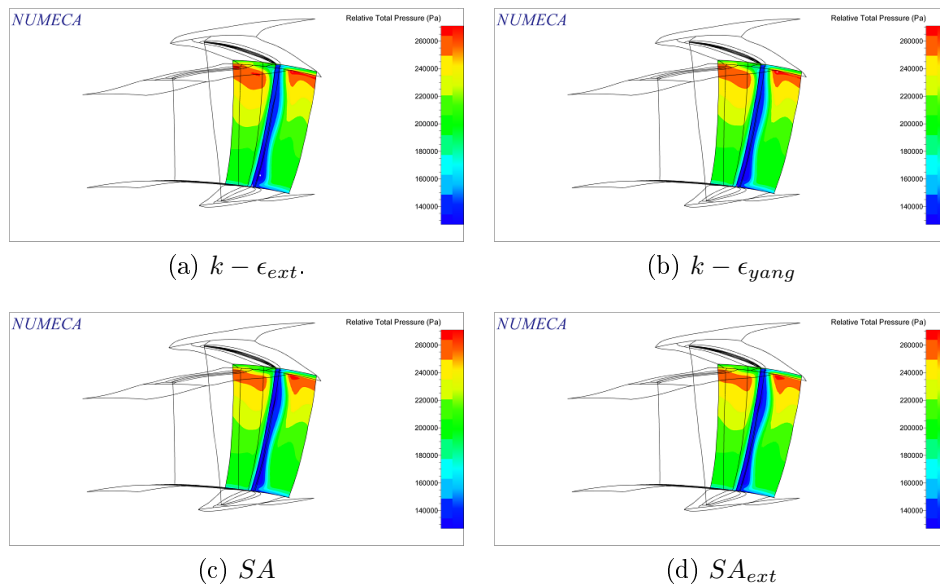


Figure 5.70: Relative Pressure Ratio - Rotor

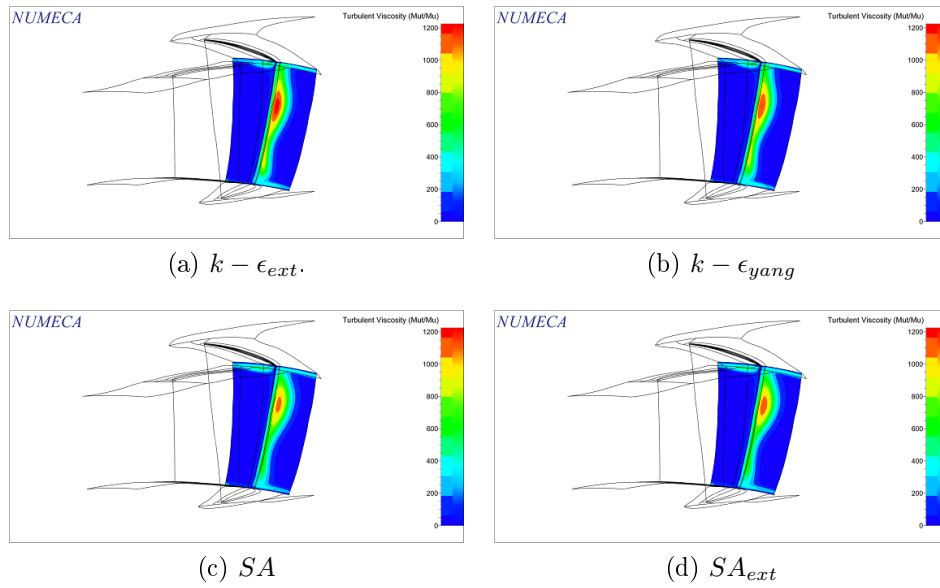


Figure 5.71: Turbulent Viscosity - Rotor

Observations:

- There are small differences in Relative Mach number, it just changes the shape of areas with higher values.
- There are small differences in Relative Pressure Ratio, it just changes shape of areas with higher values.
- Turbulent viscosity in the  $k - \epsilon$  models is higher. In particular moving from the highest,  $k - \epsilon_{ext}$ ,  $k - \epsilon_{yang}$ ,  $SA_{ext}$  and at the end  $SA$ .

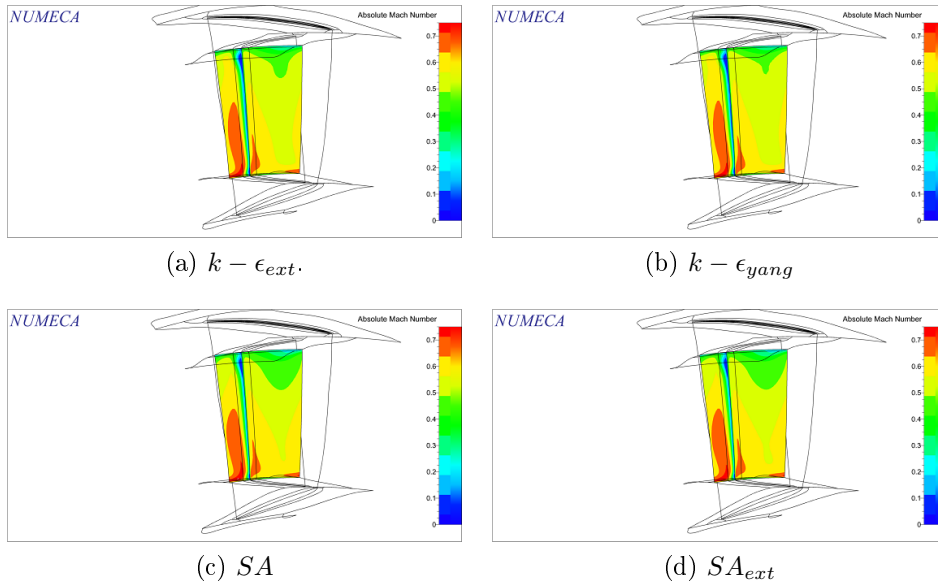


Figure 5.72: Absolute Mach - Stator

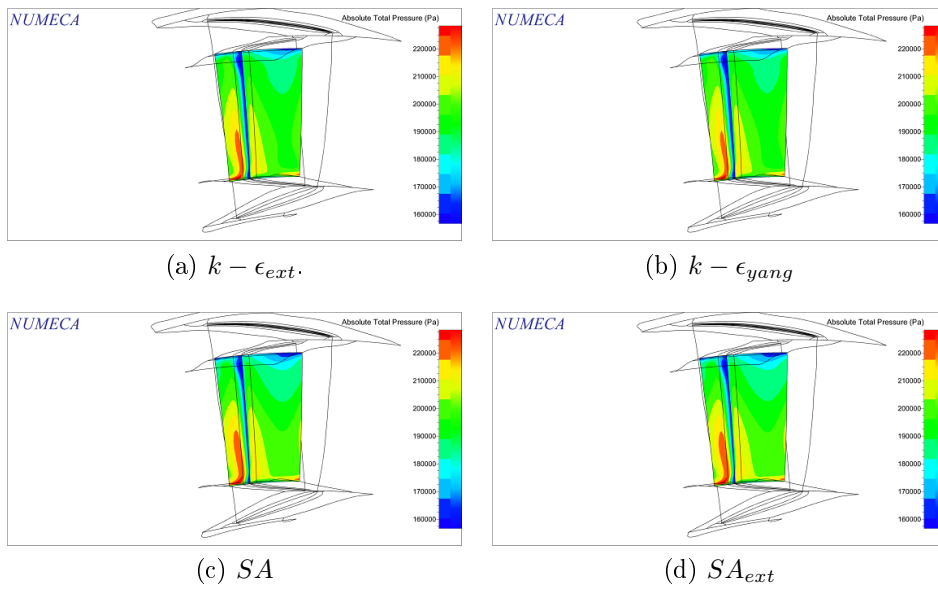


Figure 5.73: Absolute Pressure Ratio - Stator

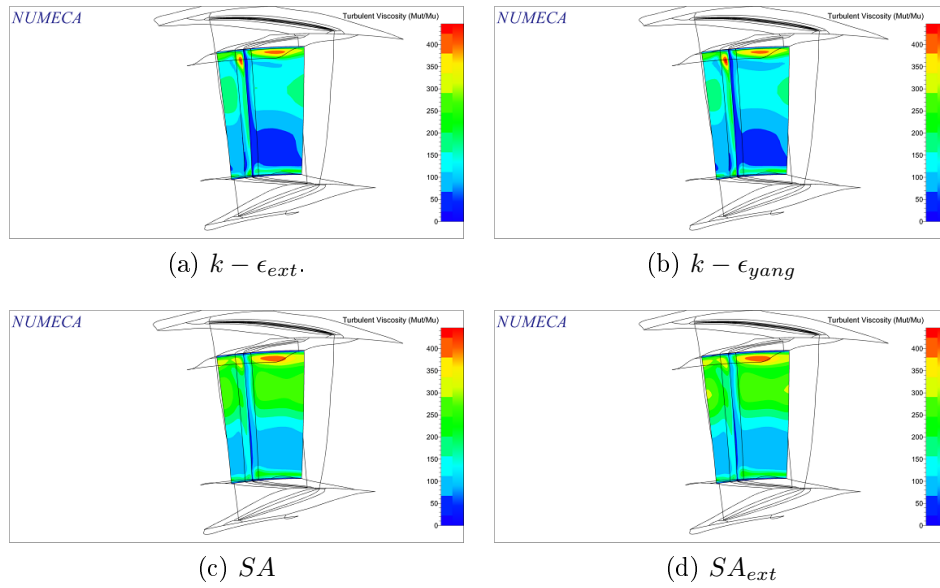


Figure 5.74: Turbulent Viscosity - Stator

Observations:

- The area shapes with different values are different between  $k - \epsilon$  and  $SA$  models.
- There are small differences in Relative Pressure Ratio, change a bit the area shapes with lower values.
- Turbulent viscosity in  $k - \epsilon$  models have higher values only near trailing edge at the top of the figure, in the other parts they are lower.

## Stall Point

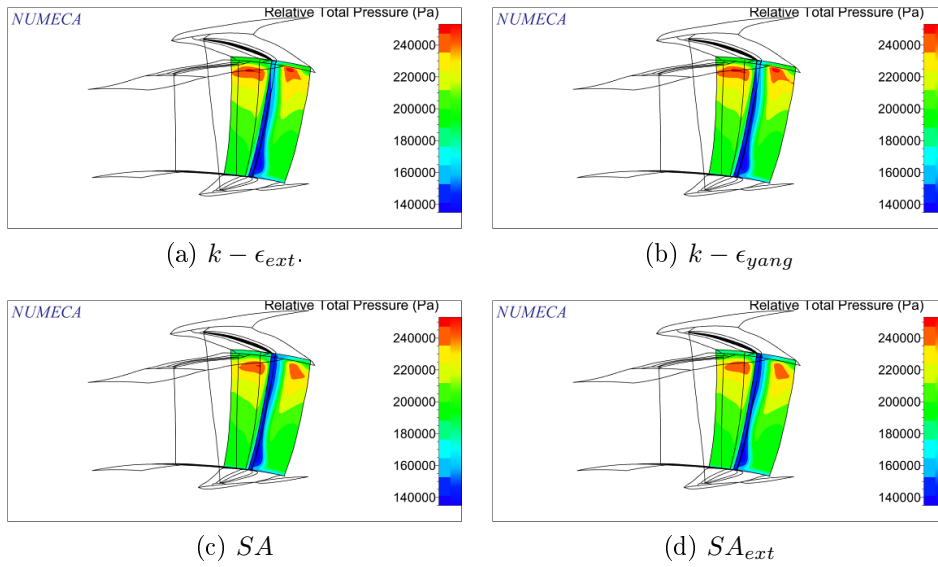


Figure 5.75: Relative Pressure Ratio - Rotor

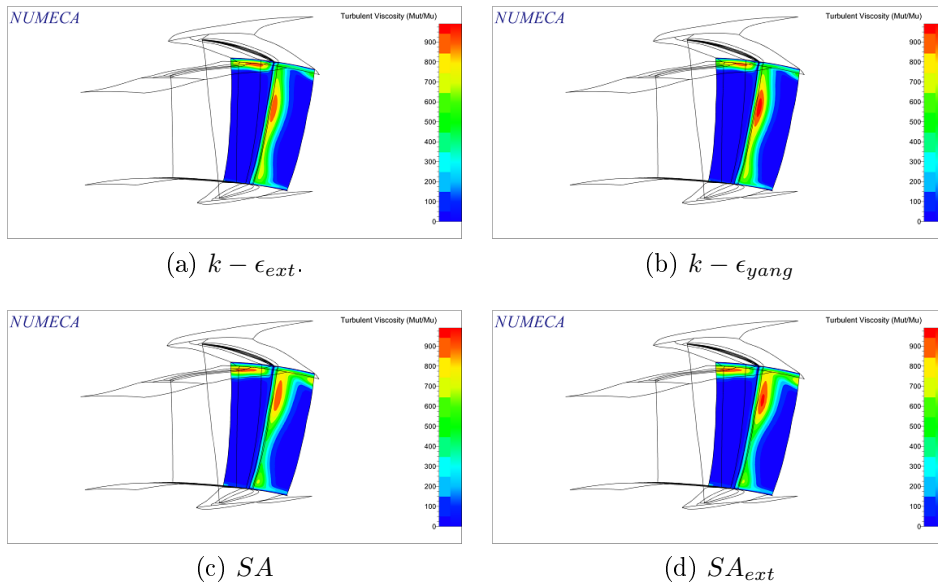


Figure 5.76: Turbulent Viscosity - Rotor

Observations:

- There are small differences in Relative Pressure Ratio, it just changes a bit the area shapes with higher values.
- The area with higher values of Turbulent viscosity in the  $SA$  models are nearer the top that the  $k - \epsilon$  models.  $SA_{ext}$  has higher values than  $SA$  and  $k - \epsilon_{yang}$  higher than  $k - \epsilon_{ext}$ .

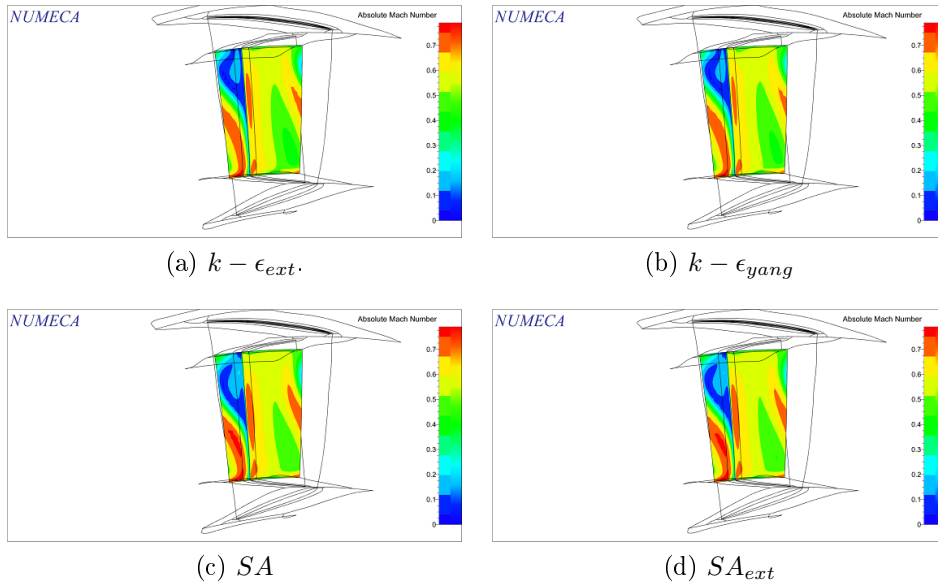


Figure 5.77: Absolute Mach - Stator

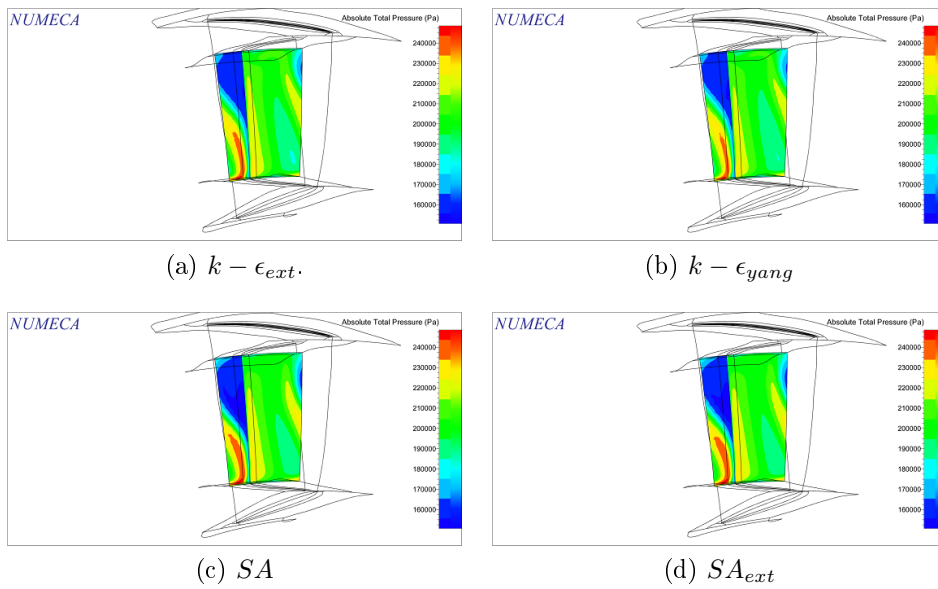


Figure 5.78: Absolute Pressure Ratio - Stator

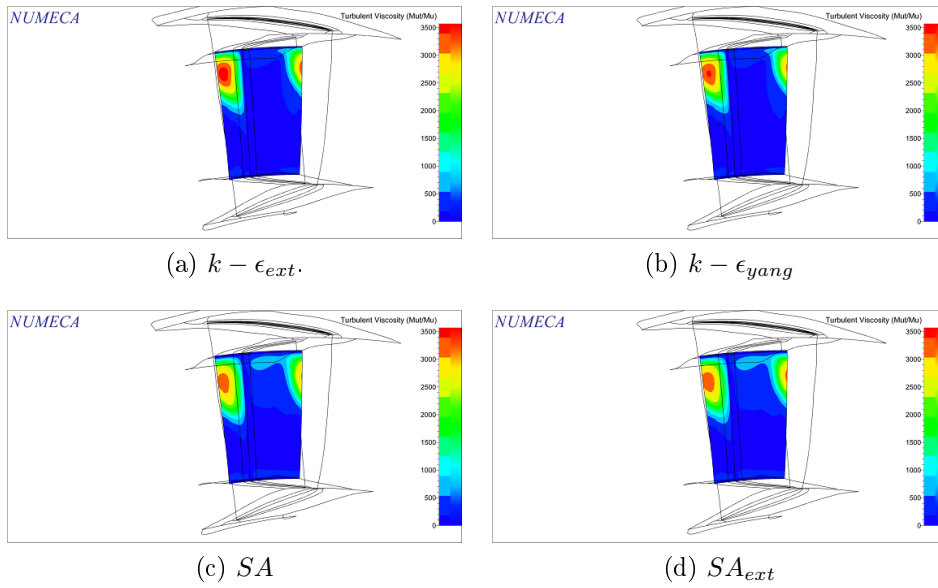


Figure 5.79: Turbulent Viscosity - Stator

Observations:

- The shapes are similar, but SA models have higher values in the area with the highest values in Absolute Mach number.
- The shapes are similar, but the SA models have higher value than the  $k - \epsilon$  models.
- The  $k - \epsilon$  models have higher values than the  $SA_{ext}$  in Turbulent Viscosity.

## 5.4.8 Conclusions

Flow visualization lets understand:

- Increasing mesh elements, increase the area with an higher Mach number.
- Increasing mesh elements, increase the area with an higher Total Pressure.
- In the 72% of the cases increasing mesh elements, increase the area with higher Turbulent Viscosity. In the remaining cases it decreases.

Each turbulent models has also a different calculation time, they are reported in Figure (5.80) normalized with SA'one.

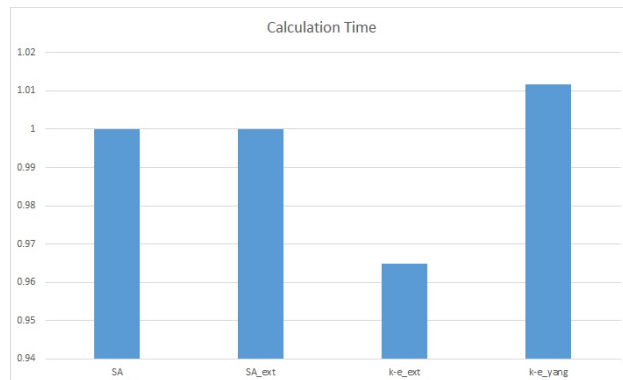


Figure 5.80: Calculation Time

The shortest calculation time is not enough to use  $k - \epsilon_{ext}$ . In the analysis was noticed that it is like a worst mesh compared to Spalart-Allmaras.

Finally the best choices are:

- Expansion Ratio: 1.2
- Max Aspect Ratio: 500
- $y^+$ : 1
- Expansion Ratio for b2b: 1.2
- O-layer: 0
- Mesh Density: B2B2
- Turbulence Models: Spalart-Allmaras

# Chapter 6

## Optimization Projects

### 6.1 Parametric Model

The optimization process is performed with IOSO. It needs a parametric model of the project studied. It is created, using Autoblade. The stage 37 is imported from Autogrid to Autoblade, at the beginning 5 sections are considered both for the rotor and the stator.

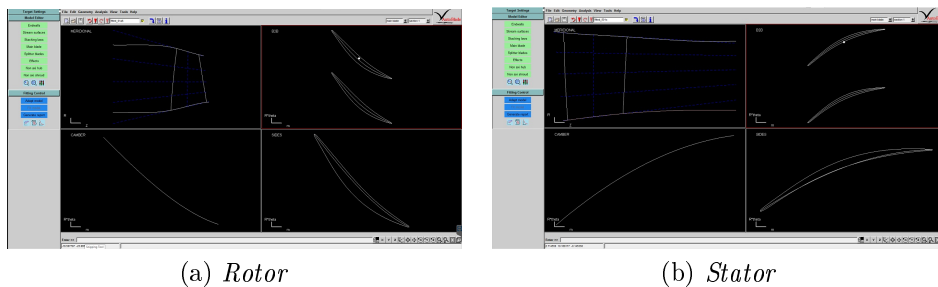


Figure 6.1

From the left column different approximations can be set:

1. Endwalls: hub and shroud endwall approximations, each one has different number of parameters. B-spline and Bezier are used.

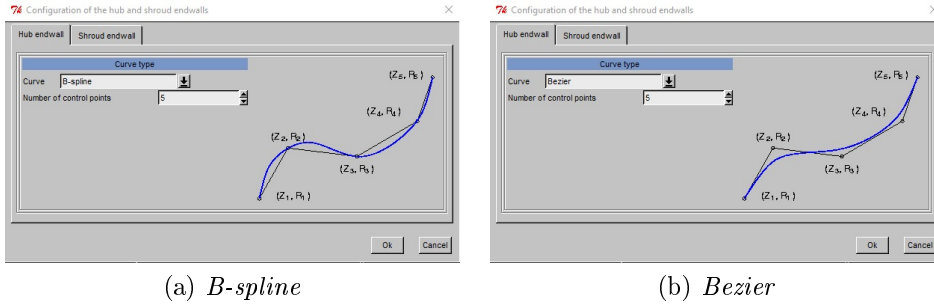


Figure 6.2

- Stream surfaces: in the section "Spanwise locations" section locations can be changed. In "Surface setup" the Stream surface type can be chosen, Planar-axial and Conical are compared.

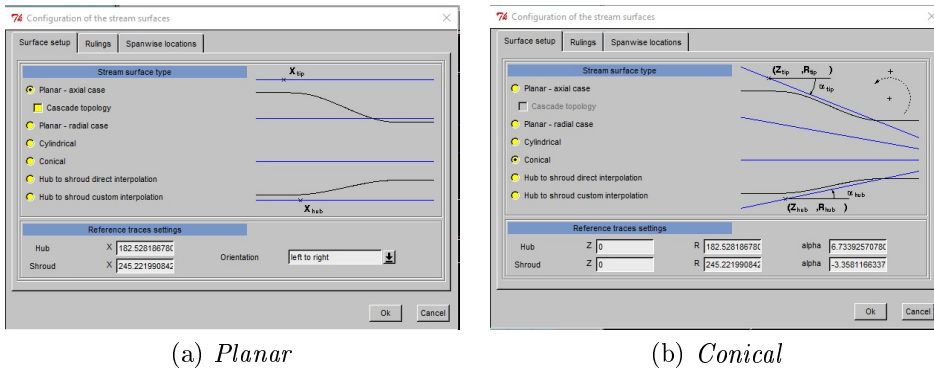


Figure 6.3

- Stacking laws: for axial compressor stacking point is located in the centre of gravity. For "Meridional location" two curve types are set, simple Bezier and Bezier (n parameters), the latter has a bigger number of parameters. Also for "Tangential location" these two approximations are used.

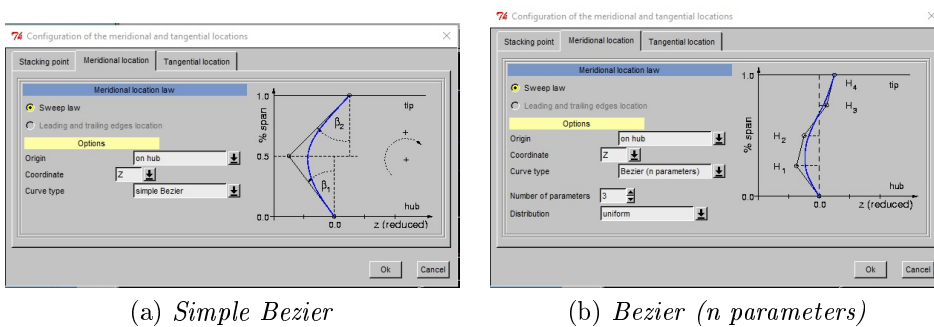


Figure 6.4

- Main blade: In "Costruction plane" two Reference length can be chosen Meridional chord based or True Chord based. To approximate the Camber curve, it is possible to choose Simple Bezier or Bezier. "Side curves" will be analyzed later.

When the model is created it is fitted, in the first iteration a Coarse accuracy is used and in the second a Fine one is used. The first and fifth stator section error, approximation and a leading edge zoom are showed.

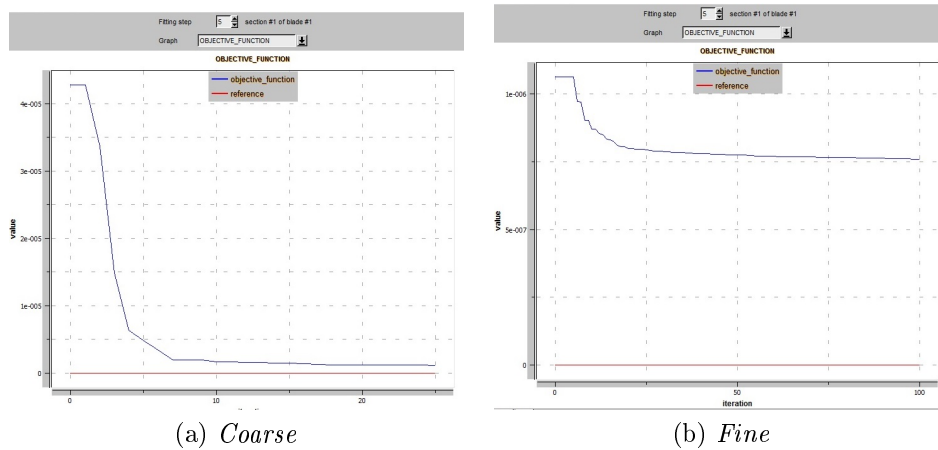


Figure 6.5: 1st section Error

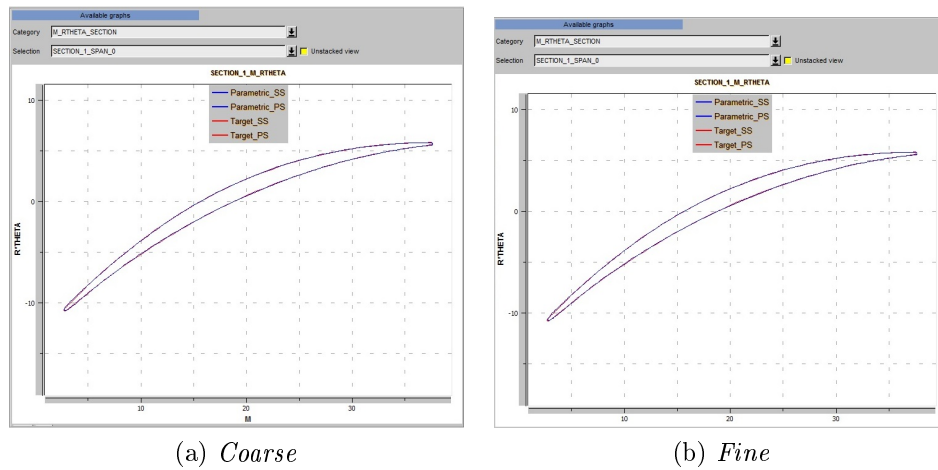
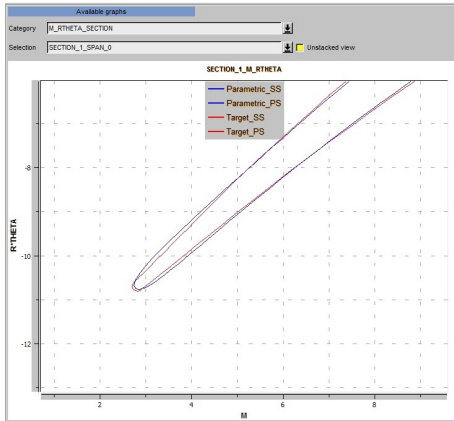
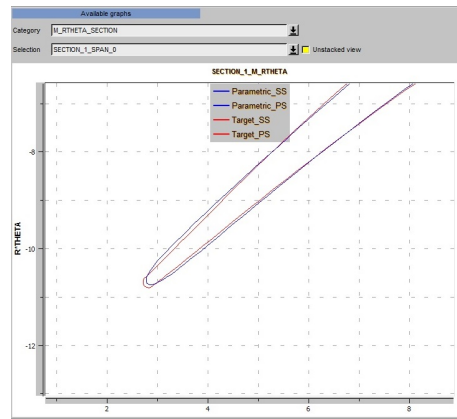


Figure 6.6: 1st section Profile

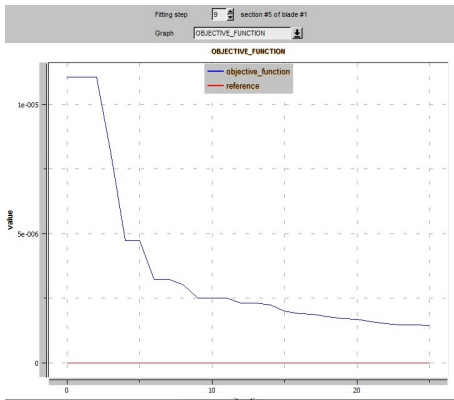


(a) Coarse

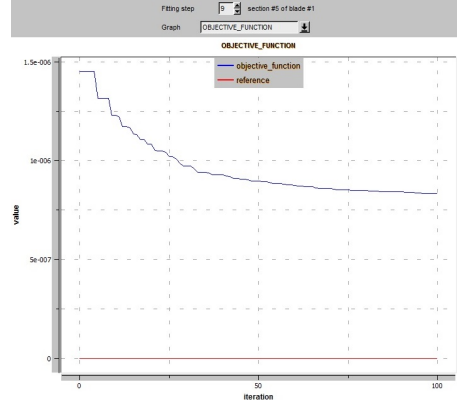


(b) Fine 1st section

Figure 6.7: 1st section Leading edge

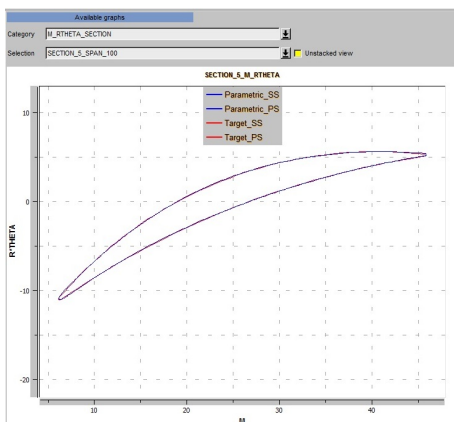


(a) Coarse

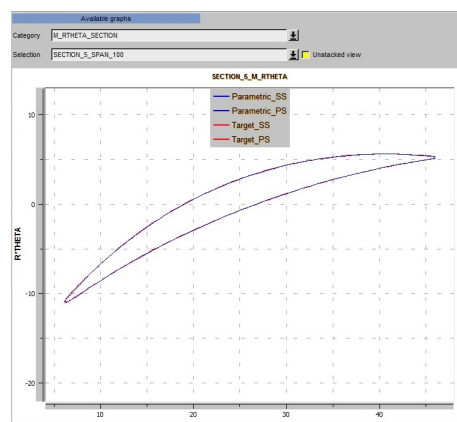


(b) Fine

Figure 6.8: 5th section Error



(a) Coarse



(b) Fine

Figure 6.9: 5th section Profile

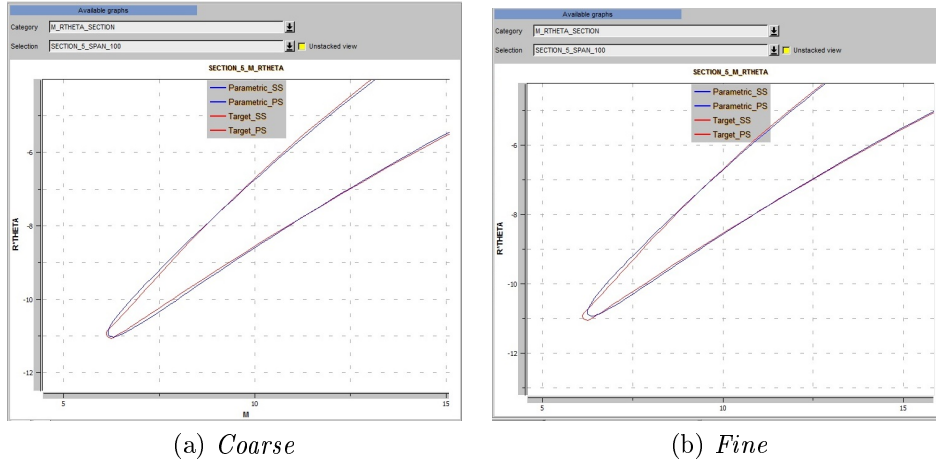


Figure 6.10: 5th section Leading edge

Eight parametric models are created, their performance curve are calculated and compared each other and with the original results.

1. Conical 6 sections Meridional Chord Based, Worst fitting ( $C6M_{WF}$ )
2. Conical 6 sections Meridional Chord Based, Best fitting ( $C6M_{BF}$ )
3. Planar 6 sections Meridional Chord Based, Worst fitting ( $P6M_{WF}$ )
4. Planar 6 sections Meridional Chord Based, Best fitting ( $P6M_{BF}$ )
5. Conical 6 sections True Chord Based, Worst fitting ( $C6T_{WF}$ )
6. Conical 6 sections True Chord Based, Best fitting ( $C6T_{BF}$ )
7. Planar 6 sections True Chord Based, Worst fitting ( $P6T_{WF}$ )
8. Planar 6 sections True Chord Based, Best fitting ( $P6T_{BF}$ )

Worst fitting refers to the first of the two approximation options showed before.

Best fitting refers to the second option.

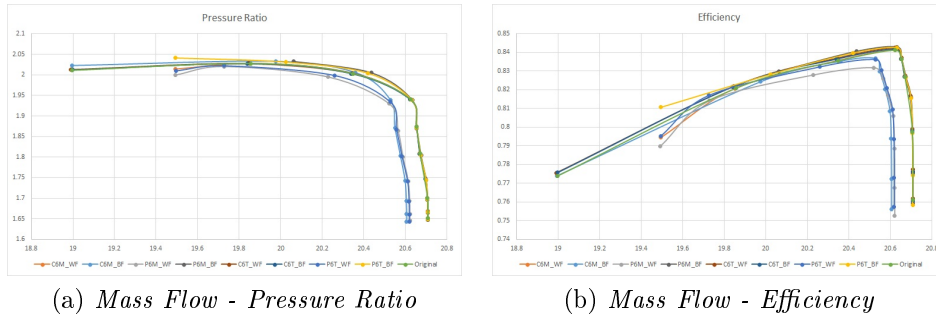


Figure 6.11

The best two parametric models are  $C6T_{WF}$  and  $C6T_{BF}$ . The former is chosen because it uses lower number of parameters. The influence of the others parameters is now studied.

In Main Blade the Camber curve can be approximated with Bezier and B-spline.

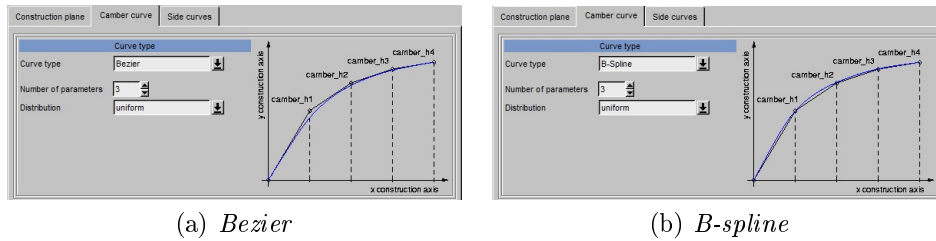


Figure 6.12

In Side curves it is possible to set two kind of Construction mode: legacy and regular.



Figure 6.13

In the previous analysis was set the option for side curves like in Figure (6.14). A Stretching factor equal to 1 (uniform) and 2 or 3 Number of intermediate control points both for Suction and Pressure side curve are compared.

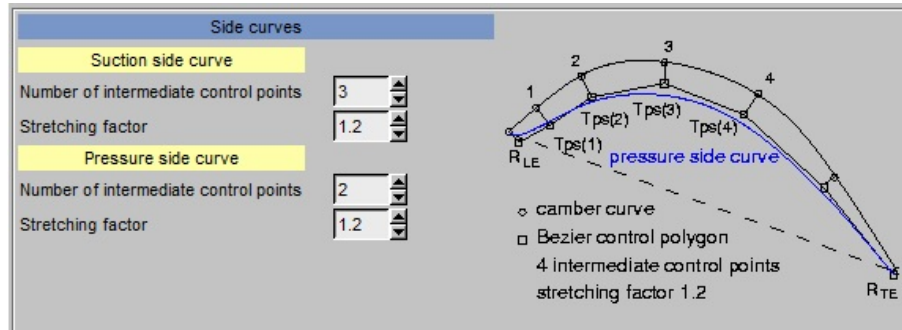


Figure 6.14: Side curves

Now six cases are analyzed.

1. Case 1: Legacy, Bezier for camber. 2 points for PS and SS.
2. Case 2: Legacy, Bezier for camber. 3 points for PS and SS.
3. Case 3: Legacy, B-spline for camber. 2 points for PS and SS.
4. Case 4: Legacy, B-spline for camber. 3 points for PS and SS.
5. Case 5: Regular, Bezier for camber. 2 points for PS and SS.
6. Case 6: Regular, Bezier for camber. 3 points for PS and SS.

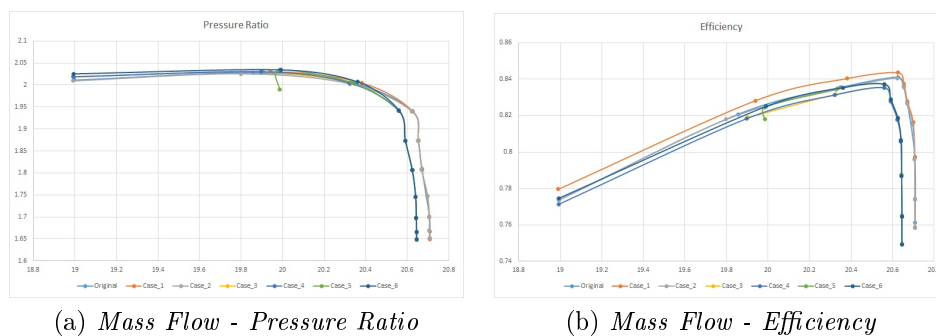


Figure 6.15

The Case 2 is the best one and as expected it is better than  $C6T_{WF}$ .

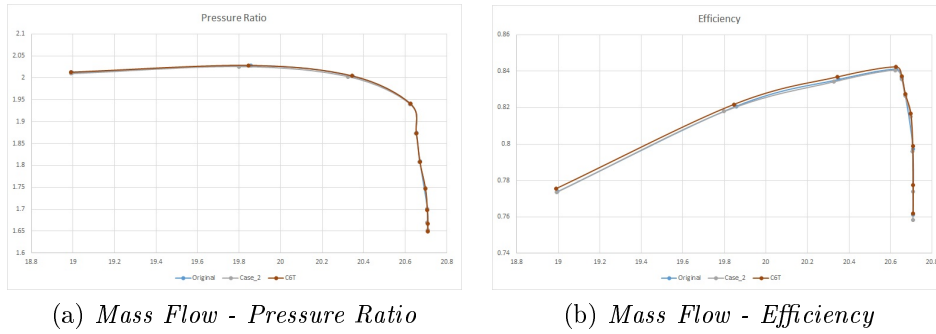


Figure 6.16

To reduce the parameter numbers now 5 rotor sections and 3 stator sections are considered, this variant is indicated as Final. As expected the approximation is a bit worse but the parameters number used is smaller.

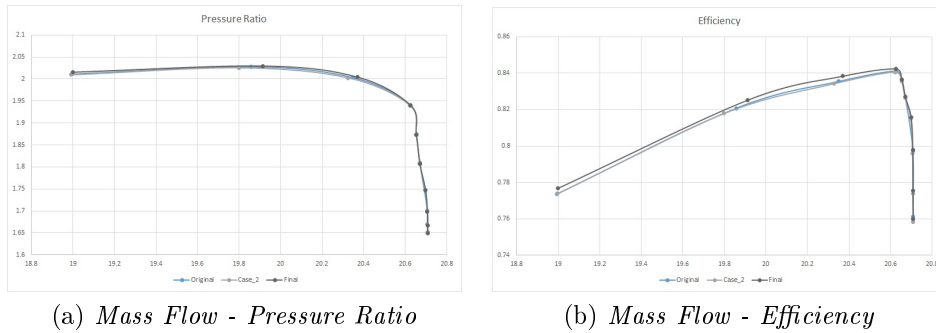


Figure 6.17

A list of all parameters can be obtained at the end of each fitting model. It is possible to change the reference, that is the step of each iteration, the lower and the upper bond for each parameter.

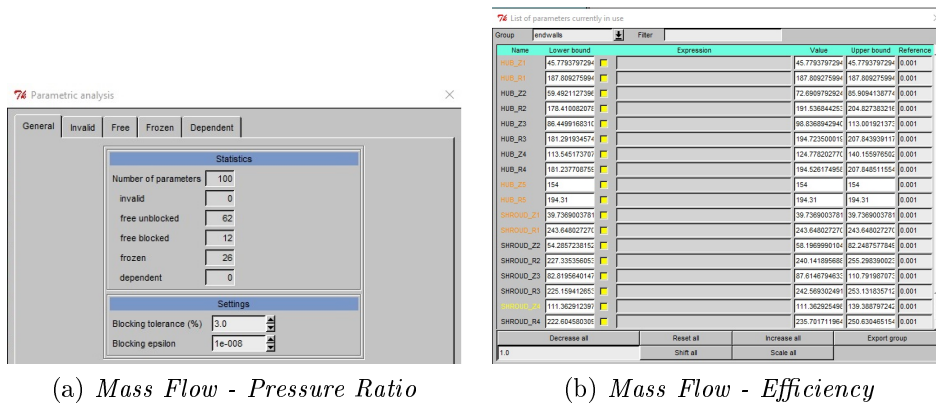


Figure 6.18

From this list a text file can be created and opened in IOSO. In section Project

Setting the parameters, that can be changed during the optimization, are defined as variables. Some parameters as hub and shroud coordinates are frozen. The geometric variables selected are called Input Parameters in section Task Section, they are 117.

In Project Setting the chock point, the work point and the stall point total pressure ratio, efficiency, mass flow, power and alpha are define as Output Parameters in the Task Section. Some limitations are imposed, for example that the max efficiency can not be lower than its initial value.

In Synthetic Parameters are defined parameters that depend on other variables, for example the stall margin.

In section Initial Points the initial geometric parameters values are set.

In section Algorithm solution and constrain accuracy are set.

Input Parameters					
No.	ID	Name	Model	Type	Definition
1	IV1	Rot_S1_chamber_chord	Model	Dependent	56.729763382257
2	IV1	Rot_S1_chamber_gamma	Model	Independent	-45.51026074-dV1+28.51026074
3	IV1	Rot_S1_chamber_h1	Model	Independent	-9.20868923-dV1+2.791319077
4	IV1	Rot_S1_chamber_h2	Model	Independent	-14.5515404-dV1+2.551540401
5	IV1	Rot_S1_le_radius	Model	Dependent	0.2574972865273
6	IV1	Rot_S1_te_radius	Model	Dependent	0.19296415796241
7	IV1	Rot_S1_le_wedge_angle	Model	Dependent	24.9852603727873
8	IV1	Rot_S1_ss_1	Model	Dependent	0.00279521434369127
9	IV1	Rot_S1_ss_2	Model	Dependent	0.059609944056682
10	IV1	Rot_S1_ss_3	Model	Dependent	0
11	IV1	Rot_S1_ss_1	Model	Dependent	-0.068678403317391
12	IV1	Rot_S1_ss_2	Model	Dependent	0.190108408199627
13	IV1	Rot_S1_ss_3	Model	Dependent	0
14	IV1	Rot_S2_chamber_chord	Model	Dependent	56.2509188755224
15	IV1	Rot_S2_chamber_gamma	Model	Independent	-54.14894241-dV1+34.14894241
16	IV1	Rot_S2_chamber_h1	Model	Independent	-8.577193028-dV1+3.422808972
17	IV1	Rot_S2_chamber_h2	Model	Independent	-12.17267814-dV1+0.172678142
18	IV1	Rot_S2_le_radius	Model	Dependent	0.20186392395472
19	IV1	Rot_S2_te_radius	Model	Dependent	0.170244295291216
20	IV1	Rot_S2_le_wedge_angle	Model	Dependent	22.63849263469125
21	IV1	Rot_S2_ss_1	Model	Dependent	-0.008827762573599
22	IV1	Rot_S2_ss_2	Model	Dependent	0.0750024593275762
23	IV1	Rot_S2_ss_3	Model	Dependent	0
24	IV1	Rot_S2_ss_1	Model	Dependent	-0.0429088186363083
25	IV1	Rot_S2_ss_2	Model	Dependent	0.135760019129266
26	IV1	Rot_S2_ss_3	Model	Dependent	0
27	IV1	Rot_S3_chamber_chord	Model	Dependent	56.0896395897672
28	IV1	Rot_S3_chamber_gamma	Model	Independent	-59.41532701-dV1+39.41532701
29	IV1	Rot_S3_chamber_h1	Model	Independent	-7.445236959-dV1+4.554763042
30	IV1	Rot_S3_chamber_h2	Model	Independent	-11.30149683-dV1+0.698503168
31	IV1	Rot_S3_le_radius	Model	Dependent	0.167088165962501
32	IV1	Rot_S3_te_radius	Model	Dependent	0.152604536320104
33	IV1	Rot_S3_le_wedge_angle	Model	Dependent	20.3188035644292
34	IV1	Rot_S3_ss_1	Model	Dependent	-0.0124300274788574
35	IV1	Rot_S3_ss_2	Model	Dependent	0.063839594423549
36	IV1	Rot_S3_ss_3	Model	Dependent	0
37	IV1	Rot_S3_ss_1	Model	Dependent	-0.0464654002497453
38	IV1	Rot_S3_ss_2	Model	Dependent	0.114191448462439
39	IV1	Rot_S3_ss_3	Model	Dependent	0
40	IV1	Rot_S4_chamber_chord	Model	Dependent	56.1551574786753
41	IV1	Rot_S4_chamber_gamma	Model	Independent	-64.51516327-dV1+44.51516327
42	IV1	Rot_S4_chamber_h1	Model	Independent	-6.221871849-dV1+5.778128151
43	IV1	Rot_S4_chamber_h2	Model	Independent	-10.56815931-dV1+1.431840695
44	IV1	Rot_S4_le_radius	Model	Dependent	0.125794432189891
45	IV1	Rot_S4_te_radius	Model	Dependent	0.129172957138669
46	IV1	Rot_S4_le_wedge_angle	Model	Dependent	17.5387199093395
47	IV1	Rot_S4_ss_1	Model	Dependent	-0.012596329151143
48	IV1	Rot_S4_ss_2	Model	Dependent	0.063779393961641
49	IV1	Rot_S4_ss_3	Model	Dependent	0

(a) Input Parameters

Output Parameters						
No.	ID	Name	Model	Objective	Constraint	Range
1	RS1	Choke_TPR	Model	No control	No bounds	
2	RS2	Choke_power	Model	No control	No bounds	
3	RS3	Choke_eff	Model	No control	No bounds	
4	RS4	Choke_mass	Model	No control	Upper and lower bounds	19.99946-rS4<21.6439
5	RS5	Choke_alpha	Model	No control	No bounds	
6	RS6	Work_TPR	Model	No control	Upper and lower bounds	1.847656-rS6<1.961944
7	RS7	Work_power	Model	No control	No bounds	
8	RS8	Work_eff	Model	Maximize	Lower bound	0.7927845-rS8
9	RS9	Work_mass	Model	No control	Upper and lower bounds	19.93156-rS9<21.16444
10	RS10	Work_alpha	Model	No control	Upper and lower bounds	-1.9315-rS10<18.0635
11	RS11	Stall_TPR	Model	No control	Lower bound	1.966093-rS11
12	RS12	Stall_power	Model	No control	No bounds	
13	RS13	Stall_eff	Model	No control	Lower bound	0.777195-rS13
14	RS14	Stall_mass	Model	No control	Lower bound	19.1672-rS14
15	RS15	Stall_alpha	Model	No control	No bounds	

(b) Output Parameters

Figure 6.19

Now different tasks are created with different range of Input and Output Parameters. The objective of IOSO is to find the max efficiency in the working point. Five cases are considered:

- Task 1: change only thickness in a small range.

Task 1		
	Rotor	Stator
<i>Camber</i>	0	0
<i>SuctionSide</i>	3*5	3*3
<i>PressureSide</i>	3*5	3*3
<i>Lean</i>	0	0
<i>Sweep</i>	0	0

In total there are 48 variables plus the outlet pressure at rotor.

$$G_{choke} = \pm 3\%$$

$$G_{work} = \pm 3\%, TPR_{work} = \pm 3\%, \eta_{work} \geq -5\%, \alpha_{work} = \pm 10^\circ$$

$$G_{stall} \geq -3\%, TPR_{work} \geq -3\%, \eta_{work} \geq -5\%$$

- Task 2: change only the stagger angle in a small range.

Task 2		
	Rotor	Stator
<i>Camber</i>	3*5	3*3
<i>SuctionSide</i>	0	0
<i>PressureSide</i>	0	0
<i>Lean</i>	0	0
<i>Sweep</i>	0	0

In total there are 24 variables plus the outlet pressure at rotor.

$$G_{choke} = \pm 3\%$$

$$G_{work} = \pm 3\%, TPR_{work} = \pm 3\%, \eta_{work} \geq -5\%, \alpha_{work} = \pm 10^\circ$$

$$G_{stall} \geq -3\%, TPR_{work} \geq -3\%, \eta_{work} \geq -5\%$$

- Task 3: change only the stagger angle in a wide range.

Task 3

---

	<b>Rotor</b>	<b>Stator</b>
<i>Camber</i>	3*5	3*3
<i>SuctionSide</i>	0	0
<i>PressureSide</i>	0	0
<i>Lean</i>	0	0
<i>Sweep</i>	0	0

In total there are 24 variables plus the outlet pressure at rotor.

$$G_{choke} = \pm 1\%$$

$$G_{work} = \pm 0.5\%, TPR_{work} = \pm 0.5\%, \eta_{work} \geq -1\%, \alpha_{work} = \pm 2.5^\circ$$

$$G_{stall} \geq -0.5\%, TPR_{work} \geq -0.5\%, \eta_{work} \geq -1\%$$

- Task 4: change the stagger angle, the thickness and the chords.

Task 4

---

	<b>Rotor</b>	<b>Stator</b>
<i>Camber</i>	3*5	3*3
<i>SuctionSide</i>	3*5	3*3
<i>PressureSide</i>	3*5	3*3
<i>Lean</i>	0	0
<i>Sweep</i>	0	0
<i>Chords</i>	5	3

In total there are 80 variables plus the outlet pressure at rotor.

$$G_{choke} = \pm 1\%$$

$$G_{work} = \pm 0.5\%, TPR_{work} = \pm 0.5\%, \eta_{work} \geq -1\%, \alpha_{work} = \pm 2.5^\circ$$

$$G_{stall} \geq -0.5\%, TPR_{work} \geq -0.5\%, \eta_{work} \geq -1\%$$

- Task 5: change the stagger angle, the thickness, the sweep, the lean and the chords.

### Task 5

	Rotor	Stator
<i>Camber</i>	3*5	3*3
<i>SuctionSide</i>	3*5	3*3
<i>PressureSide</i>	3*5	3*3
<i>Lean</i>	2	2
<i>Sweep</i>	2	2
<i>Chords</i>	5	3

In total there are 88 variables plus the outlet pressure at rotor.

$$G_{choke} = \pm 1\%$$

$$G_{work} = \pm 0.5\%, TPR_{work} = \pm 0.5\%, \eta_{work} \geq -1\%, \alpha_{work} = \pm 2.5\%$$

$$G_{stall} \geq -0.5\%, TPR_{work} \geq -0.5\%, \eta_{work} \geq -1\%$$

In Results the evolutions of each parameters can be monitored, in graphs like in Figure.

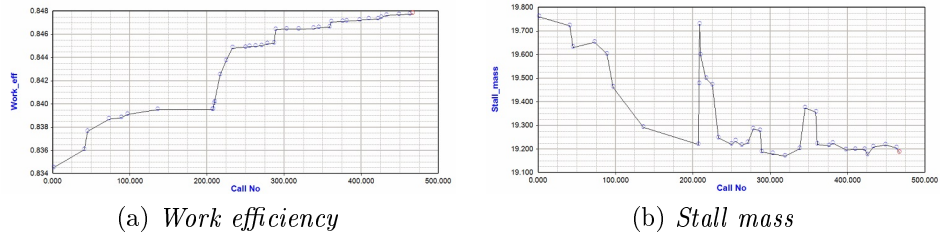


Figure 6.20

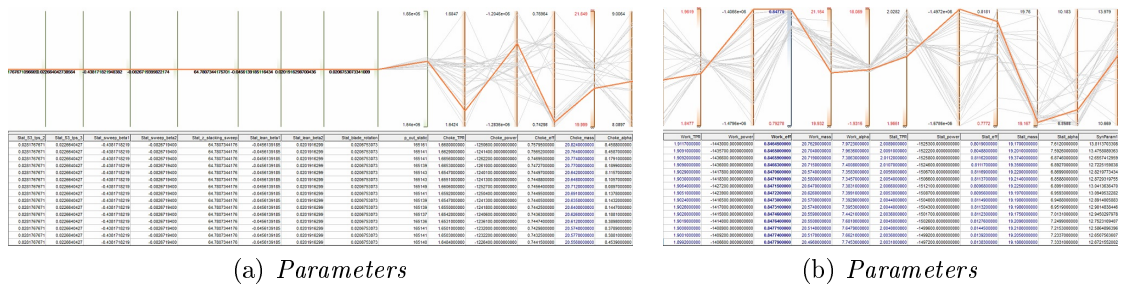


Figure 6.21

## 6.2 Strength on the Rotor Blade

An other restriction has to be added. The optimized blade can work at strength due to pressure field and the rotational velocity?

To calculate the strength on blade a project on Ansys APDL is created and the results are compared with the experimental data from Nasa report.

Starting from seven sections the geometrical model is created. The first step is to create line that connect them, then areas from lines and volumes from areas. So there are six blocks each consisting of 3 volumes, to describe the leading edge, the trailing edge and the the central part. In this way a bigger number of elements is set in the first two volumes. Element SOLID185 is used, for the three-dimensional modeling of solid structures. The element is defined by eight nodes with three degrees of freedom at each node: translations in the nodal x, y, and z directions. The element has plasticity, stress stiffening, large deflection, and large strain capabilities [28].

The blade is in Maraging steel 200, these steels are known for possessing superior strength and toughness without losing malleability, although they cannot hold a good cutting edge. Aging refers to the extended heat-treatment process. These steels are a special class of low-carbon ultra-high-strength steels that derive their strength not from carbon, but from precipitation of intermetallic compounds. The principal alloying element is 15 to 25 nickel mass concentration. Secondary alloying elements, which include cobalt, molybdenum, and titanium, are added to produce intermetallic precipitates. The number indicates the approximate nominal tensile strength in thousands of pounds per square inch [27].

After that, it is possible to apply the pressure field, taken from Numeca CFView and the rotational velocity from NASA report.

The pressure field is showed in Figure (6.22).

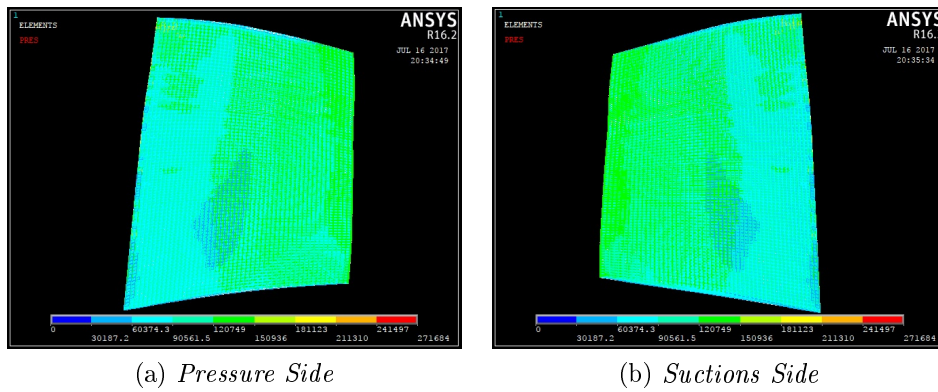


Figure 6.22: Pressure Field

The deformed shape, compared with the tip undeformed edge is showed in Figure (6.23).

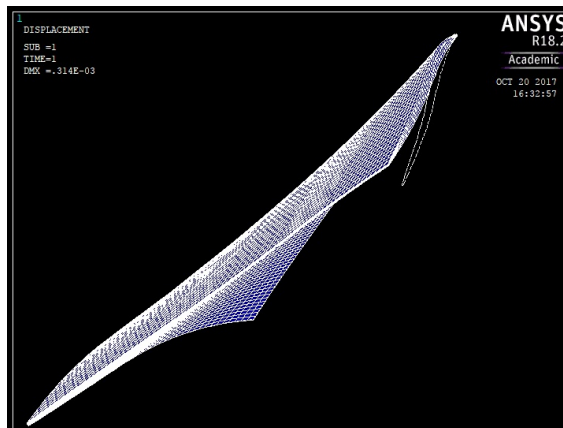
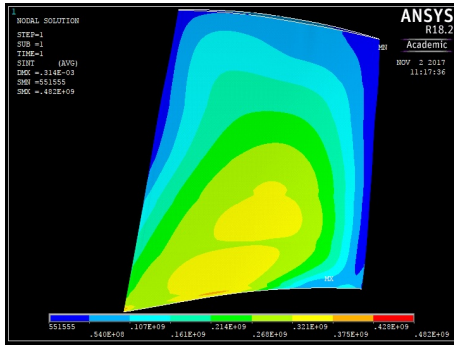
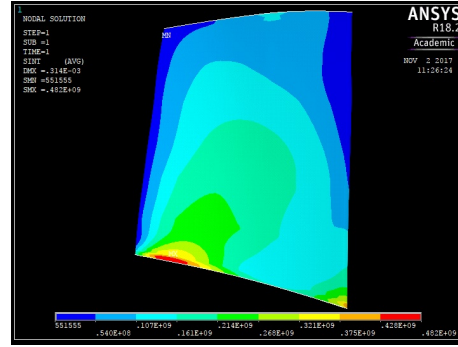


Figure 6.23: Deformed Shape

The max strength obtained is equal to the experimental data. In Figure it is possible to see the strength (6.24, 6.25) and the displacement field (6.26).

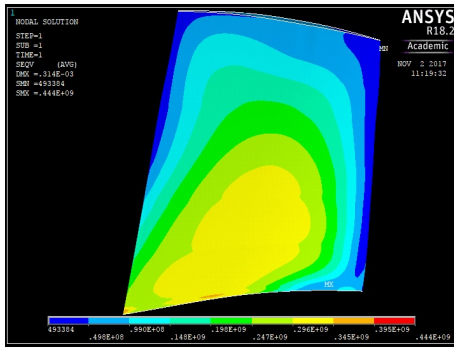


(a) Pressure Side

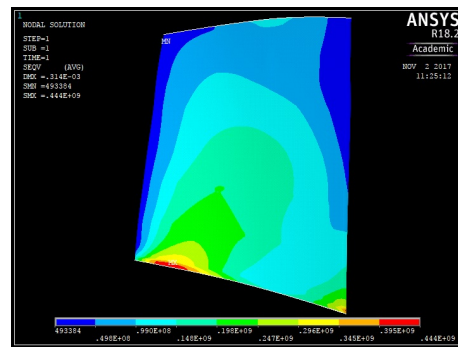


(b) Suctions Side

Figure 6.24: Strength Field - Stress Intensity

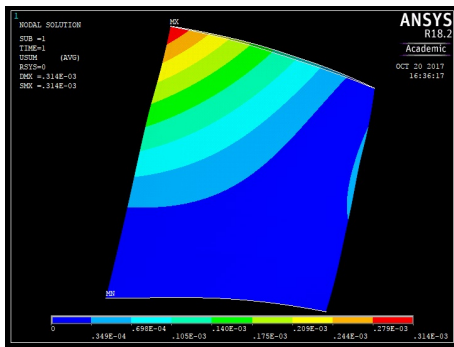


(a) Pressure Side

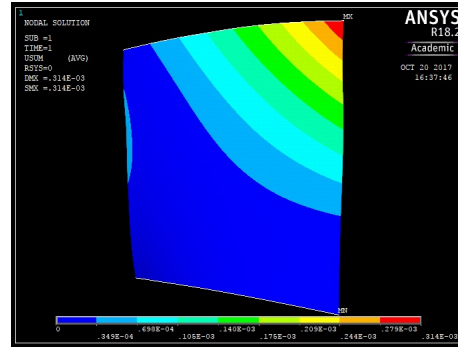


(b) Suctions Side

Figure 6.25: Strength Field - Von Mises



(a) Pressure Side



(b) Suctions Side

Figure 6.26: Displacement Field

Now the Task 6 on IOSO is created, constrain due to strength and mass are added to Task 5.

# Chapter 7

## Optimization Process

### 7.1 IOSO program

The common operations to develop a project is shown in figure:

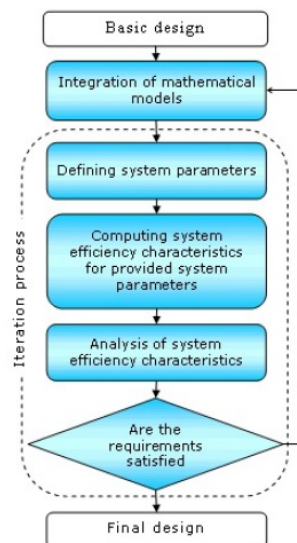


Figure 7.1

IOSO lets easily integrate the required mathematical models into a single analysis block and automate the search for alternative optimal technical solutions. IOSO algorithm allows:

- To find non standard solutions with high efficiency
- To make sure that the project is exploited as much as possible

- To increase system quality and reliability

It is possible to solve single- and multiple-objective optimization tasks. In both cases the number of independent variables can not exceed 100, the number of optimization criteria can not exceed 20 and the number of inequality constraints can not exceed 100 [29].

IOSO is based on the concept of Robust Design Optimization with which it is possible to find an optimal technical solution. IOSO (Indirect Optimization based on Self-Organization) implements the evolutionary response surface strategy, that is different from the traditional approach of nonlinear programming and the traditional response surface methodology.

The optimization problem is solved using stochastic formulation directly when at each iteration the probability parameters are evaluated. The high efficiency of the Robust Design Optimization is due to the highly efficient capabilities of the developed stochastic optimization algorithms, which reliably work also if high level of noise is present in responses.

It is possible to perform a Multilevel Robust Design Optimization and a Multiobjective Robust Design Optimization separately and simultaneously. The former uses mathematical models of various fidelity during the solution process, the latter solves the multiobjective (dozens of objective functions) multidimensional (hundred of design variables) nonlinear optimization problems.

Two different kind of optimization criteria can be consider (Figure 7.2).

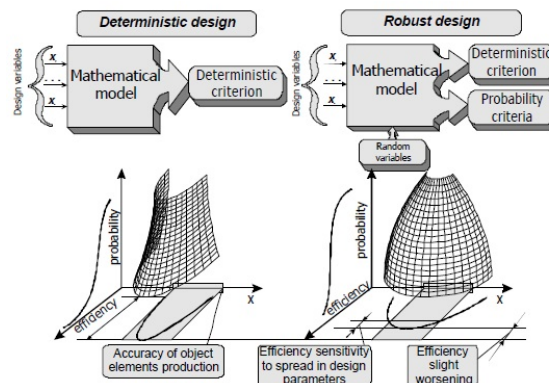


Figure 7.2: Robust design optimization essence

Deterministic criterion, in which an ideal efficiency can be achieved if it is possible to have absolutely precise practical replication of the preset parameters of the system under consideration. The other criteria are probabilistic, for example mean value of the efficiency, total probability of assuring the present constrain, variance of efficiency and so on. These criteria can contradicting each other, so different criteria are used (multiobjective optimization problem).

One of the main problem of RDO is how to evaluate the probability criteria and constraints of variables. It can be done with Monte Carlo simulation, that required a large number of sampling points or with some approximation techniques (Taylor's series and so on) but they take a long time to get a high accuracy of the probability indices because they are very sensitive to topological peculiarities of objective functions and constrains. IOSO is insensitive to them (smooth, non-differentiable, stochastic, with multiple optima, with the portions of the design space where objective function and constraints could not be evaluated at all, with the objective function and constraints dependent on mixed variables, etc.) because it uses response surface methodology. So Monte Carlo simulation can be used with tens or hundred sampling point.

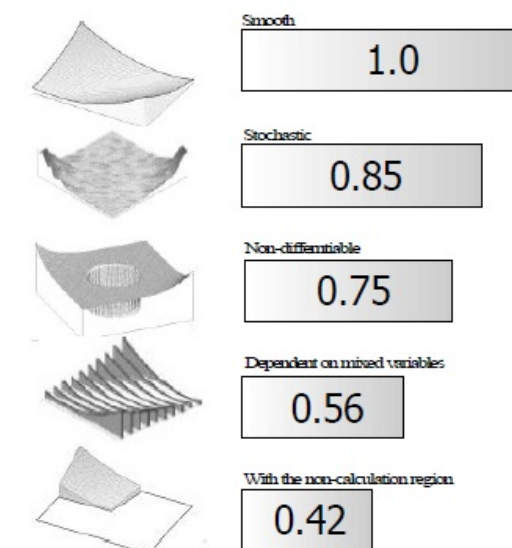


Figure 7.3: IOSO algorithms efficiency for different objective functions

The final design is found with Pareto analysis. Solving the multiobjective optimization problem it is possible to find the Pareto set, it is made with the Multiobjective

Robust Design Optimization algorithms. Let consider the multiobjective robust design optimization of the multistage axial flow compressor.

Purpose	To insure the maximum efficiency and maximum implementation probability under preset level of production technology.
Setting features	140 independent variables (flow-path geometry); two objectives; three nonlinear constraints (mass flow, pressure ratio, surge margin).
Optimization process features	Object under study – quasi-3D mathematical model. Implementation probability was calculated as the probability of assuring the preset constraints.

Figure 7.4: Brief description of the compressor robust design optimization problem

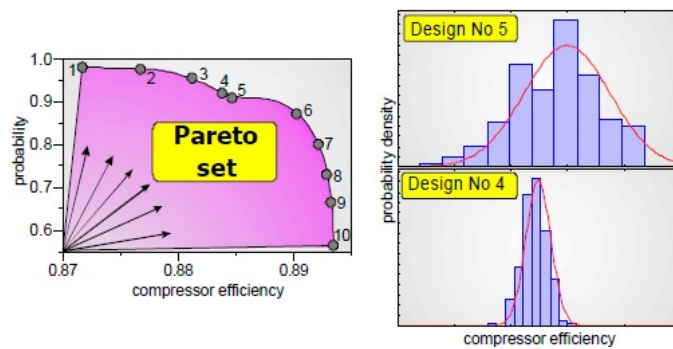


Figure 7.5: Results of compressor multicriteria robust design optimization

There is a compromise area between the ideal (deterministic) compressor efficiency and the implementation probability. In general, designer can select any solution from the obtained set. In this case the design No 4 was selected as the final design. The total number of mathematical calls was 25000, working with 140 independent variables. It is possible to use more accurate mathematical model thank to multilevel RDO procedure. It uses mathematical models of various fidelity during the solution process and a switch between them. In this way the time in which the high fidelity (true) models is reduced with the same accuracy of the resulting solution [30].

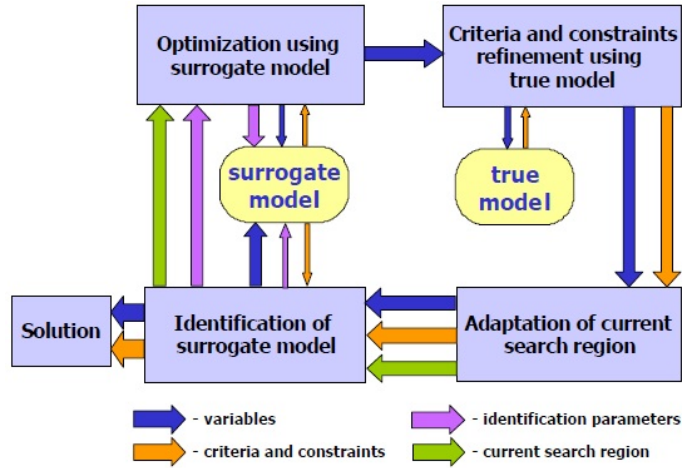


Figure 7.6: Multilevel optimization scheme

## 7.2 Optimization Results

Now the performance curves of each task are analyzed, focusing in percentage differences with Original value. The max efficiency is always higher than Original case. An important value to consider is also Stall Margin. In Original case it is 11.335%.

Task 1

	Mass Flow	Pressure Ratio	Efficiency
<i>ChokePoint</i>	-0.0193	0.0727	-1.474
	-0.0241	0.0470	-0.918
	-0.0242	-0.271	-0.218
	-0.00484	-0.401	-0.146
<i>WorkPoint</i>	-0.0921	-0.484	0.0154
	-0.712	-0.619	-0.227
	-1.375	-0.735	-0.565
<i>StallPoint</i>	2.653	0.149	5.133

The left curve goes down-right. Go to right, it is due to a mass flow reduction. Go down, it is due to a pressure ratio reduction.

The right curve goes right and almost down. Only in the working point and the stall point, efficiency is higher than Original case.

Stall Margin is 10.197%.

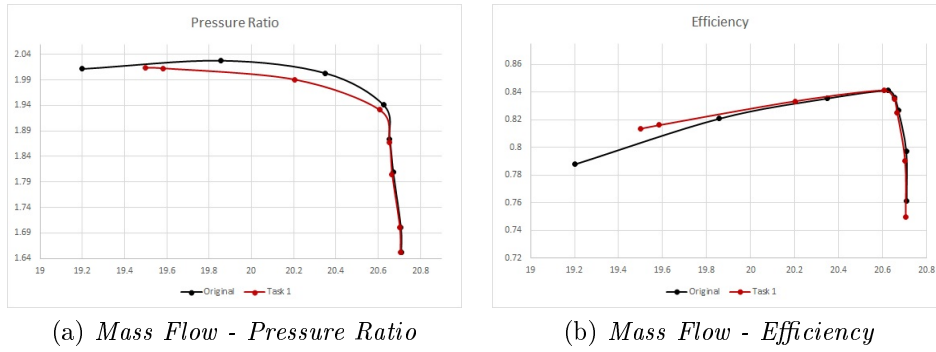


Figure 7.7: Performance Curve

Task 2

	Mass Flow	Pressure Ratio	Efficiency
<i>ChokePoint</i>	-0.0289	0.399	-2.603
	-0.0289	0.476	-1.618
	-0.00484	0.0608	-0.0568
	0	0.0789	0.0658
<i>WorkPoint</i>	0.00970	0.0824	0.247
	0.305	0.0898	0.705
	1.007	0.207	1.435
<i>StallPoint</i>	2.653	0.666	3.180

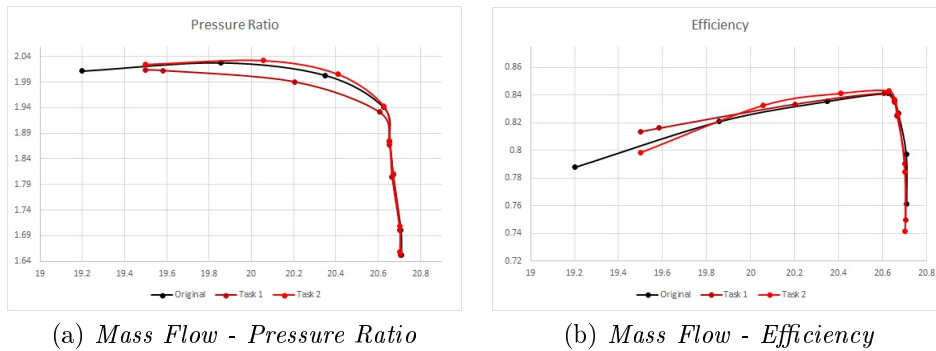


Figure 7.8: Performance Curve

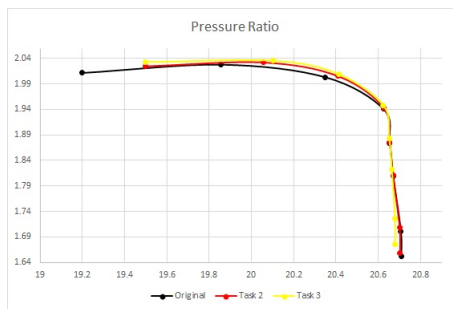
Unlike previous task, the left curve goes up-right. It is due to an increase of the pressure ratio.

The right curve goes up-right too. Only in the first 3 point there is an efficiency decrease. The working point efficiency is higher than previous task.

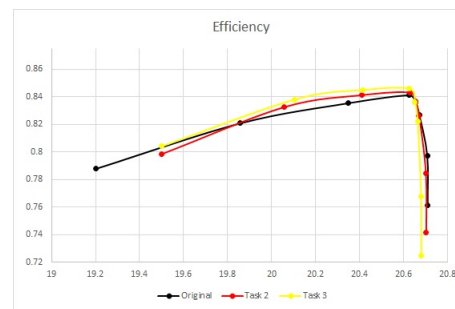
Stall Margin is 10.251%.

### Task 3

	<b>Mass Flow</b>	<b>Pressure Ratio</b>	<b>Efficiency</b>
<i>ChokePoint</i>	-0.140	1.471	-4.757
	-0.135	1.447	-3.696
	-0.0339	0.674	-0.548
	-0.00968	0.495	-0.0143
<i>WorkPoint</i>	-0.00485	0.371	0.587
	0.314	0.289	1.147
	1.244	0.379	2.102
<i>StallPoint</i>	2.648	1.079	3.895



(a) *Mass Flow - Pressure Ratio*



(b) *Mass Flow - Efficiency*

Figure 7.9: Performance Curve

The behavior is similar to previous task because the number of variables is the same but output parameters can change in a smaller range. This range is used also in the next tasks, because in each point of the performance curves the percentage change is bigger than the previous task.

Stall Margin is 10.374%.

### Task 4

	Mass Flow	Pressure Ratio	Efficiency
<i>ChokePoint</i>	0.410	0.660	2.771
	0.415	0.770	2.809
	0.566	0.315	3.180
	0.600	0.100	3.097
<i>MaxEfficiency</i>	0.461	-0.0515	2.862
	-0.663	-0.409	1.465
<i>StallPoint</i>	1.557	-0.144	4.644

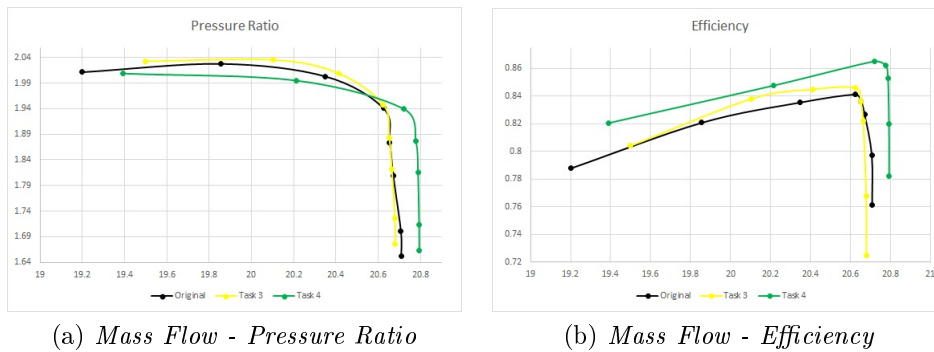


Figure 7.10: Performance Curve

A bigger number of variables are now modified. Unlike previous cases, there is a great mass flow increase also before the working point. The left curve moves right-down, like in the first task, in particular from the working point to stall point (decrease in pressure ratio). The right curves moves right-up, great increase of mass flow and efficiency in each point.

Stall Margin is 10.031%.

### Task 5

	Mass Flow	Pressure Ratio	Efficiency
<i>ChokePoint</i>	0.415	0.666	2.834
	0.420	0.776	2.863
	0.571	0.315	3.226
	0.605	0.0896	3.128
<i>MaxEfficiency</i>	0.441	-0.0618	3.059
	-0.894	-0.494	1.242
<i>StallPoint</i>	1.557	-0.129	4.660

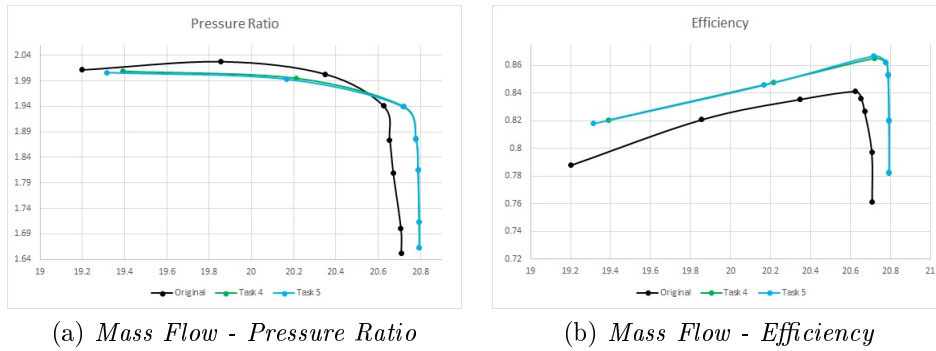


Figure 7.11: Performance Curve

8 more variables are used respect to the previous task. The behavior is almost equal to the previous task, the percentage changes are a bit bigger than Task 4. The work point efficiency is 3.059% higher that original task.

Stall Margin is 10.037%.

### Task 6

	Mass Flow	Pressure Ratio	Efficiency
<i>ChokePoint</i>	0.377	0.745	2.954
	0.381	0.876	2.990
	0.527	0.420	3.471
	0.542	0.175	3.520
<i>MaxEfficiency</i>	0.315	-0.0412	3.445
	-0.462	-0.319	2.437
<i>StallPoint</i>	1.427	-0.144	5.411

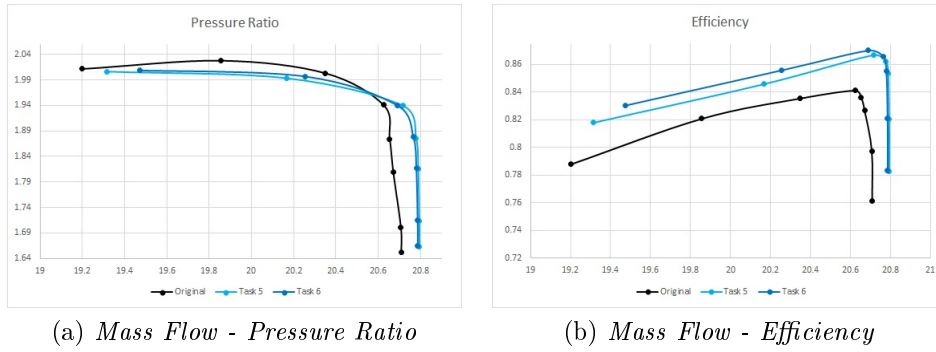


Figure 7.12: Performance Curve

The behavior is similar to previous tasks, but there is a smaller increment in mass flow, a smaller decrease in pressure ratio and a great increase in efficiency. The work point efficiency is 3.445% higher than original task.

Stall Margin is 10.001%.

The optimized performance curves of Mass Flow-Pressure Ratio tends to move right (increase of the mass flow), down decrease of the pressure ratio. The curves of Mass Flow-Efficiency tends to move right-up, increase of the mass flow and the efficiency.

## 7.3 Post optimization considerations

Let's focus on Work point. The Efficiency, Mass Flow and Pressure Ratio change are compared for each Task.

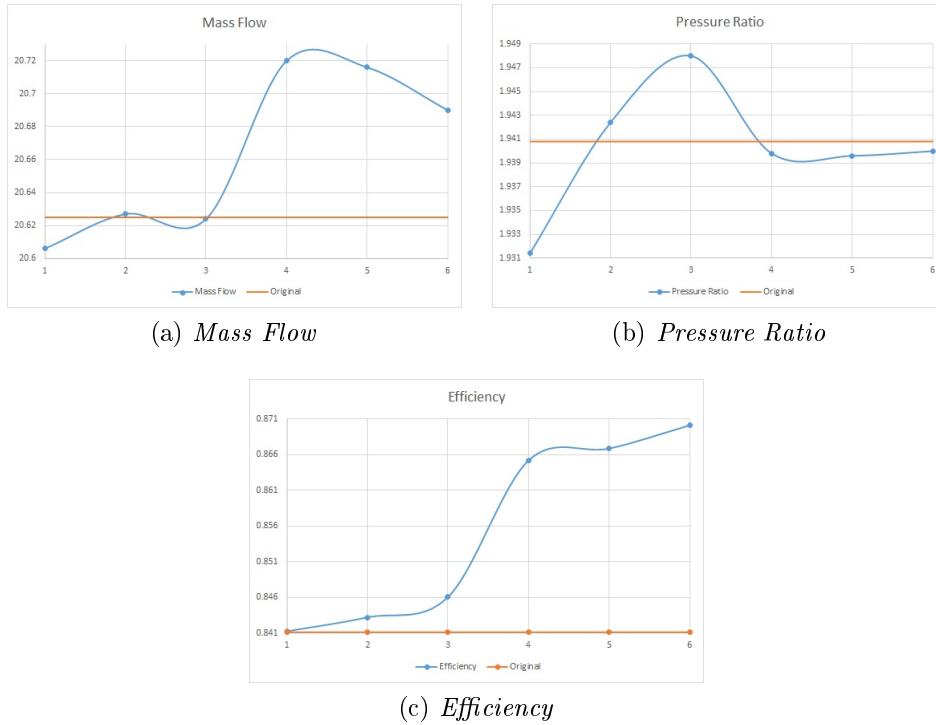


Figure 7.13: Work Point

Using a cluster of 9 CPUs, the calculation time for each iteration is 50 minutes, it is possible to calculate (time in hours):

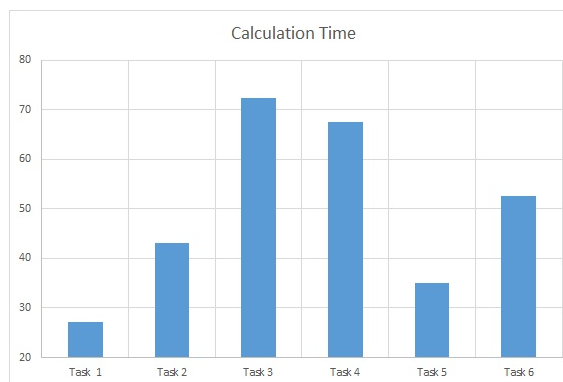


Figure 7.14: Calculation Time

An analysis similar to the Chapter 4 one is conducted on the working point for each task. Starting from the radial distribution:

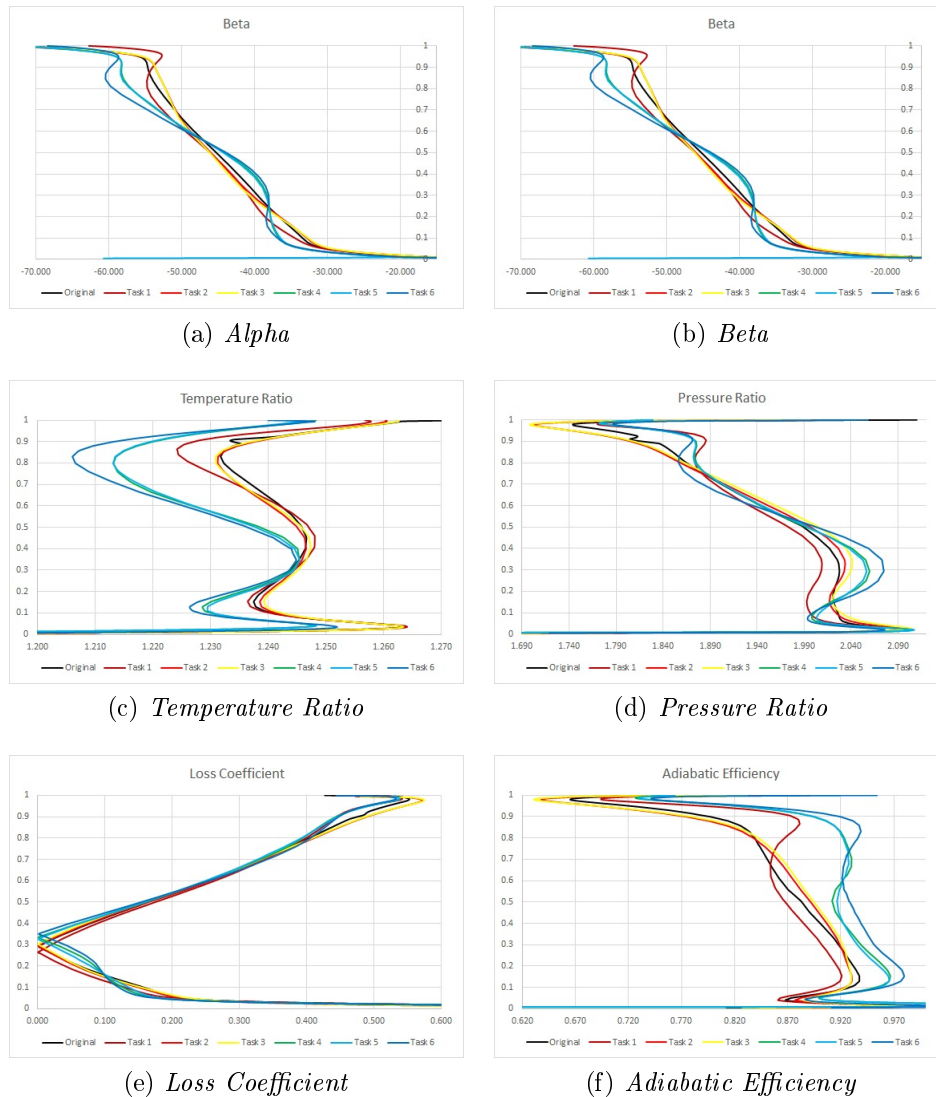


Figure 7.15: Radial Distribution

Both for alpha e beta it is possible to individuate two groups of curves. One made of the last three tasks, the other from the remaining curves. The former, in particular has lower value of alpha and beta near the tip; the latter has a quite linear trend. This splitting in two group can be noticed also in other distribution. The former presents lower value in temperature ratio and higher value in pressure ratio at 0.3 and 0.9 of the blade.

Loss coefficient tends to move slightly upward in the blade moving from task 1 to task 6.

The former group has higher value of adiabatic efficiency in all the distribution.

Now the flow visualization is evaluated:

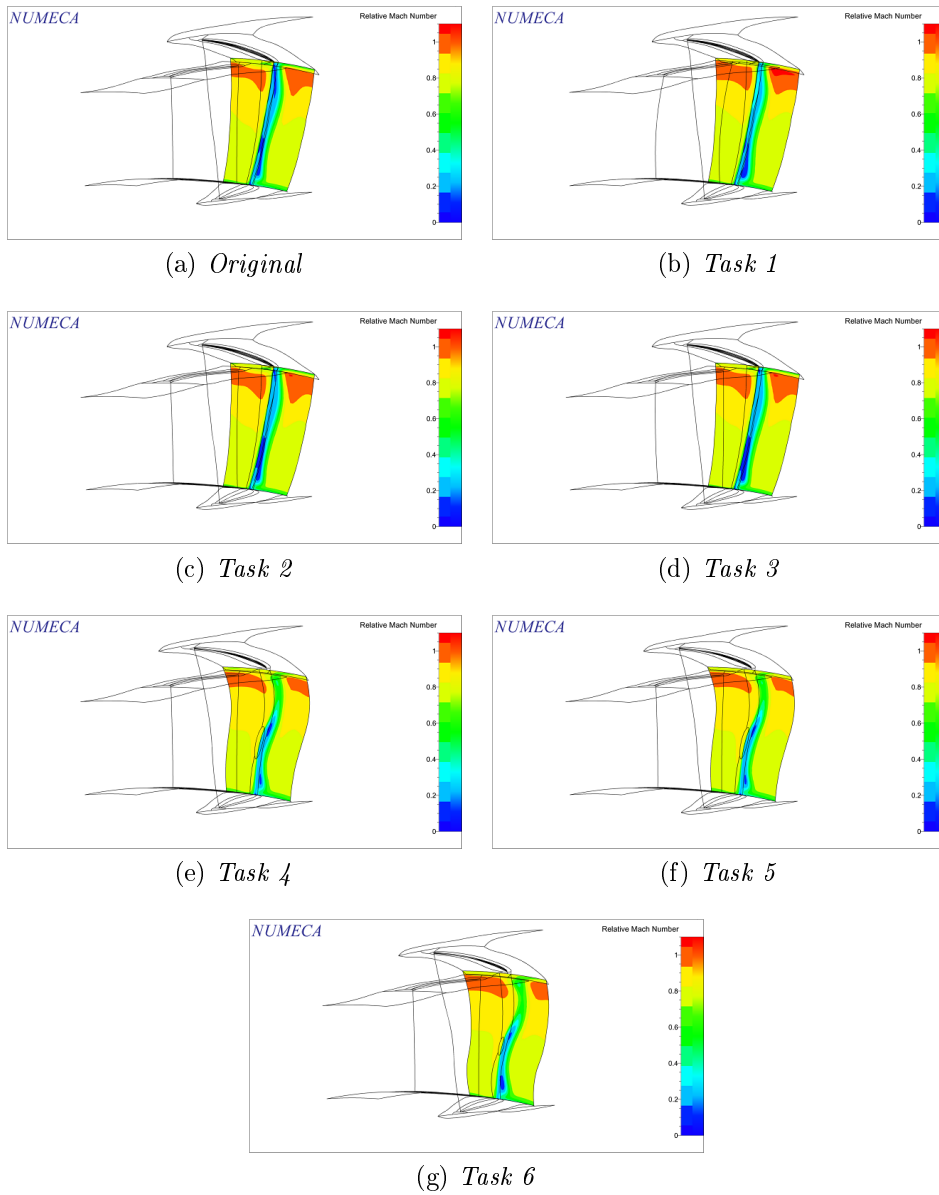


Figure 7.16: Relative Mach - Rotor

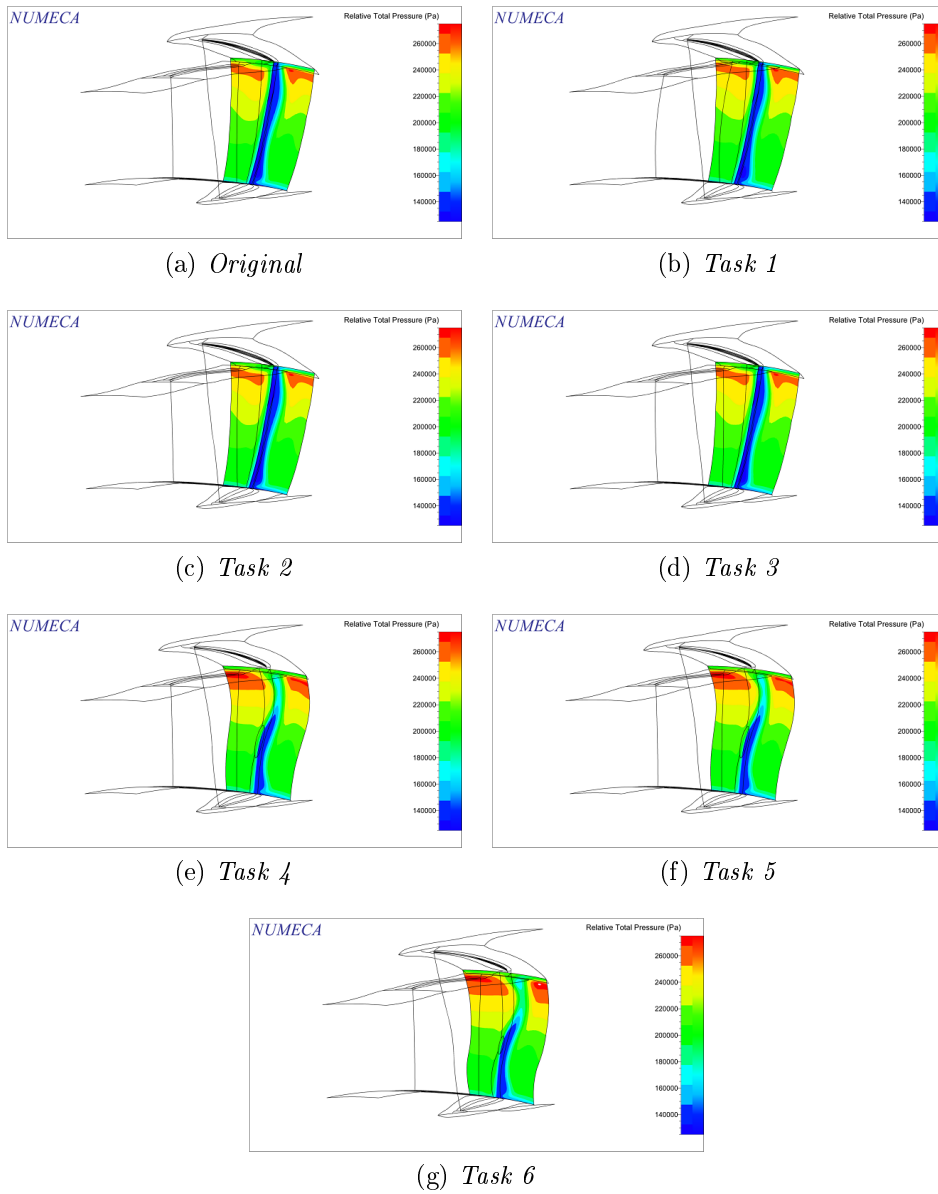


Figure 7.17: Relative Total Pressure - Rotor

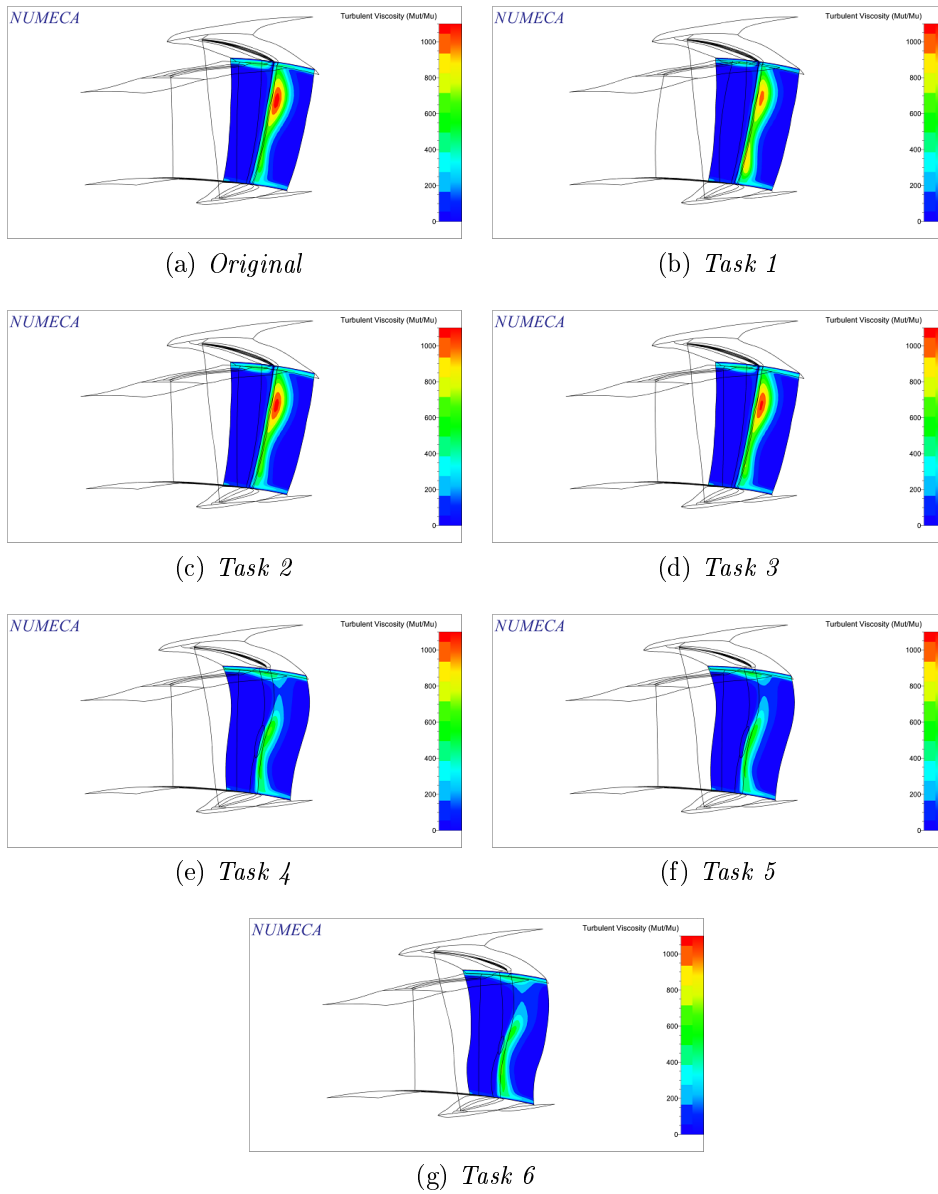


Figure 7.18: Turbulent Viscosity - Rotor

Rotor: both relative mach and relative total pressure tends to increase, turbulent viscosity tends to reduce moving from Original to Task 6.

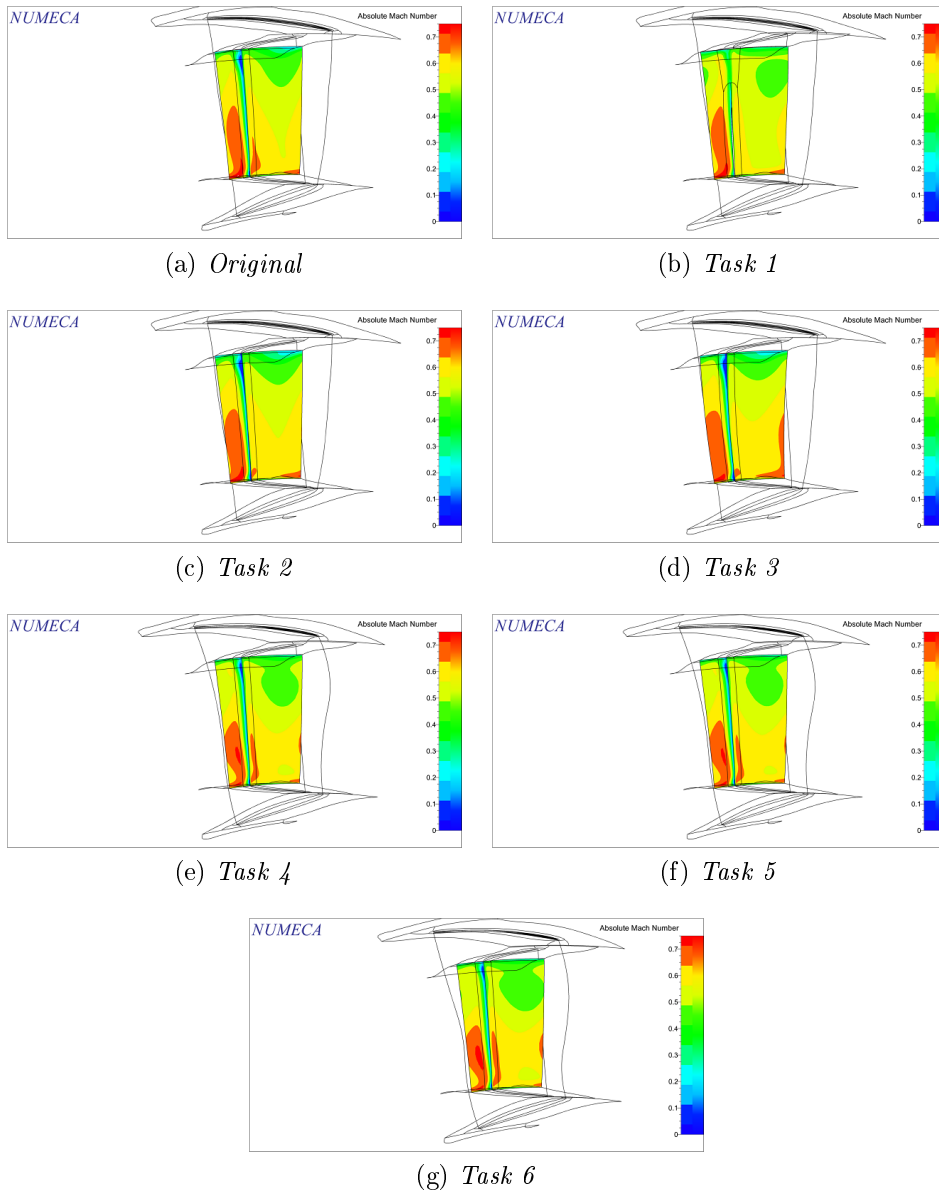


Figure 7.19: Absolute Mach - Stator

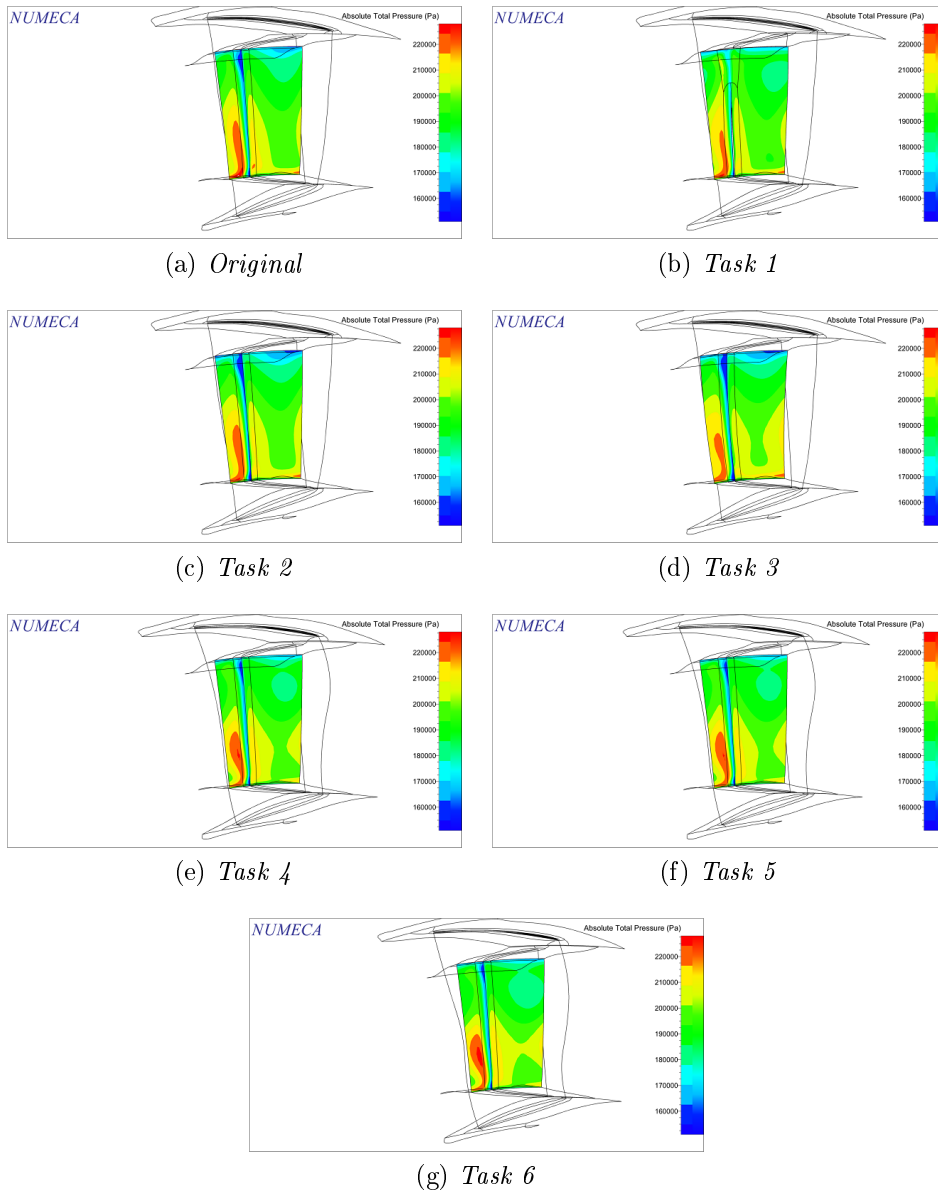


Figure 7.20: Absolute Total Pressure - Stator

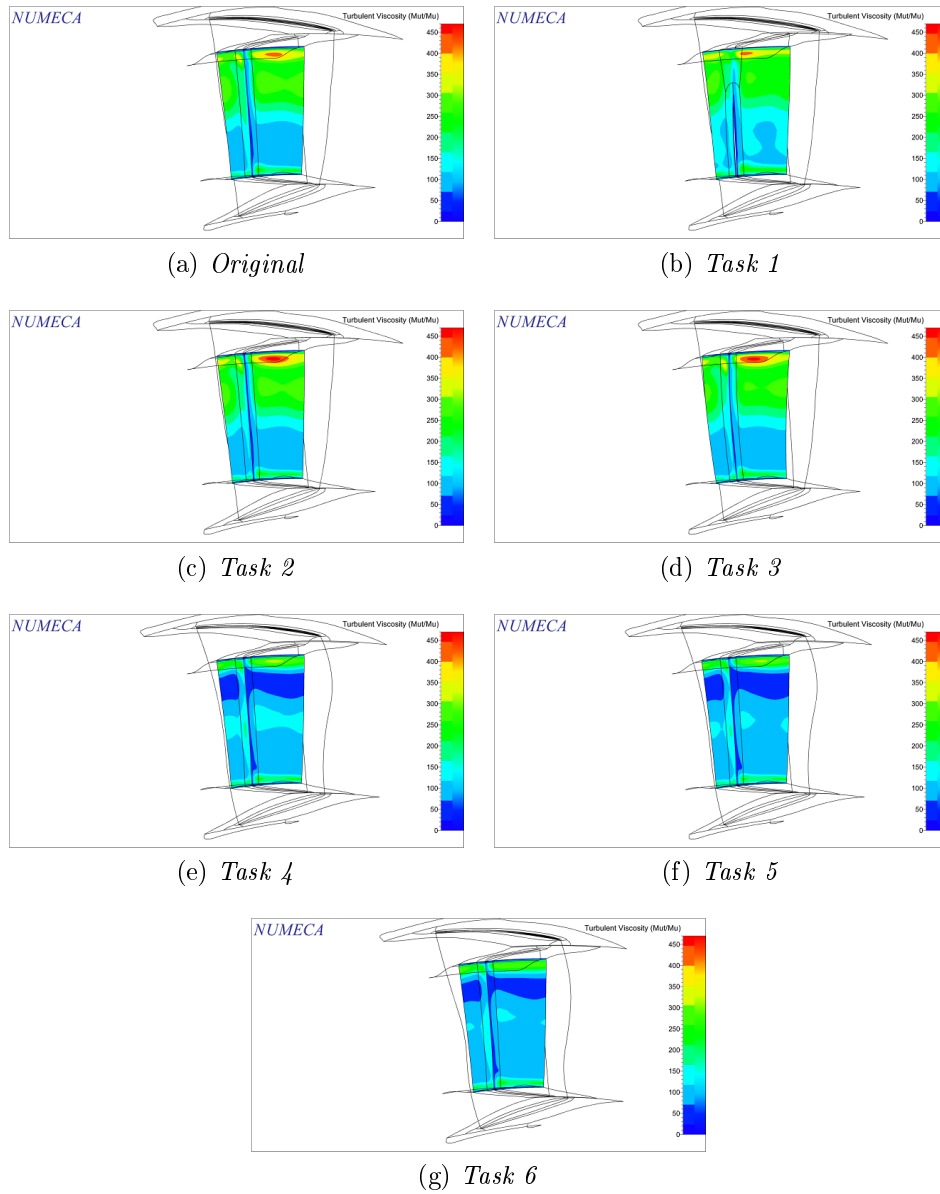


Figure 7.21: Turbulent Viscosity - Stator

Stator: both absolute Mach number and absolute total pressure tend to increase, turbulent viscosity tends to decrease moving from Original to Task 6.

Relative Mach is considered in a blade to blade view, a plane parallel to y-z at the hub is considered.

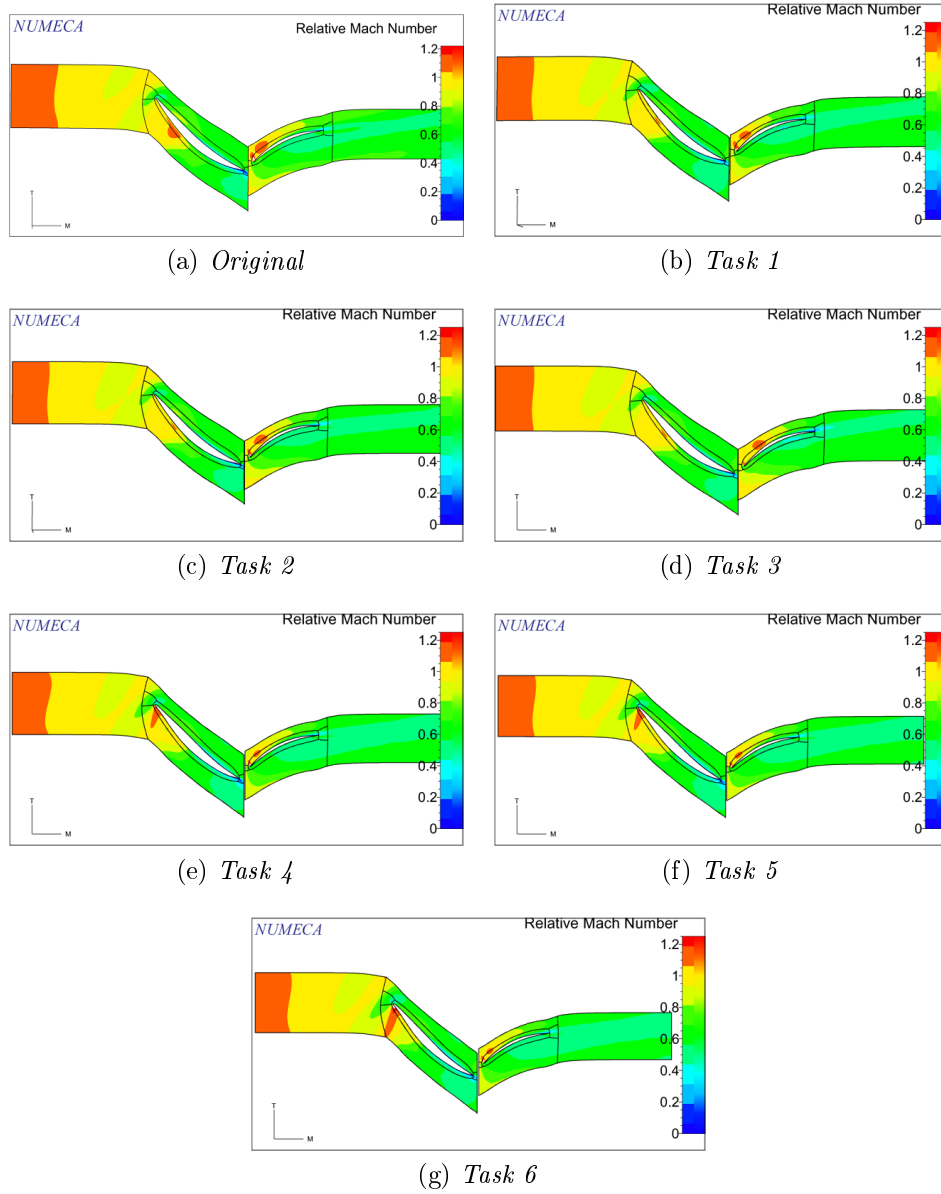


Figure 7.22: Relative Mach

Relative Mach on Meridional Average View:

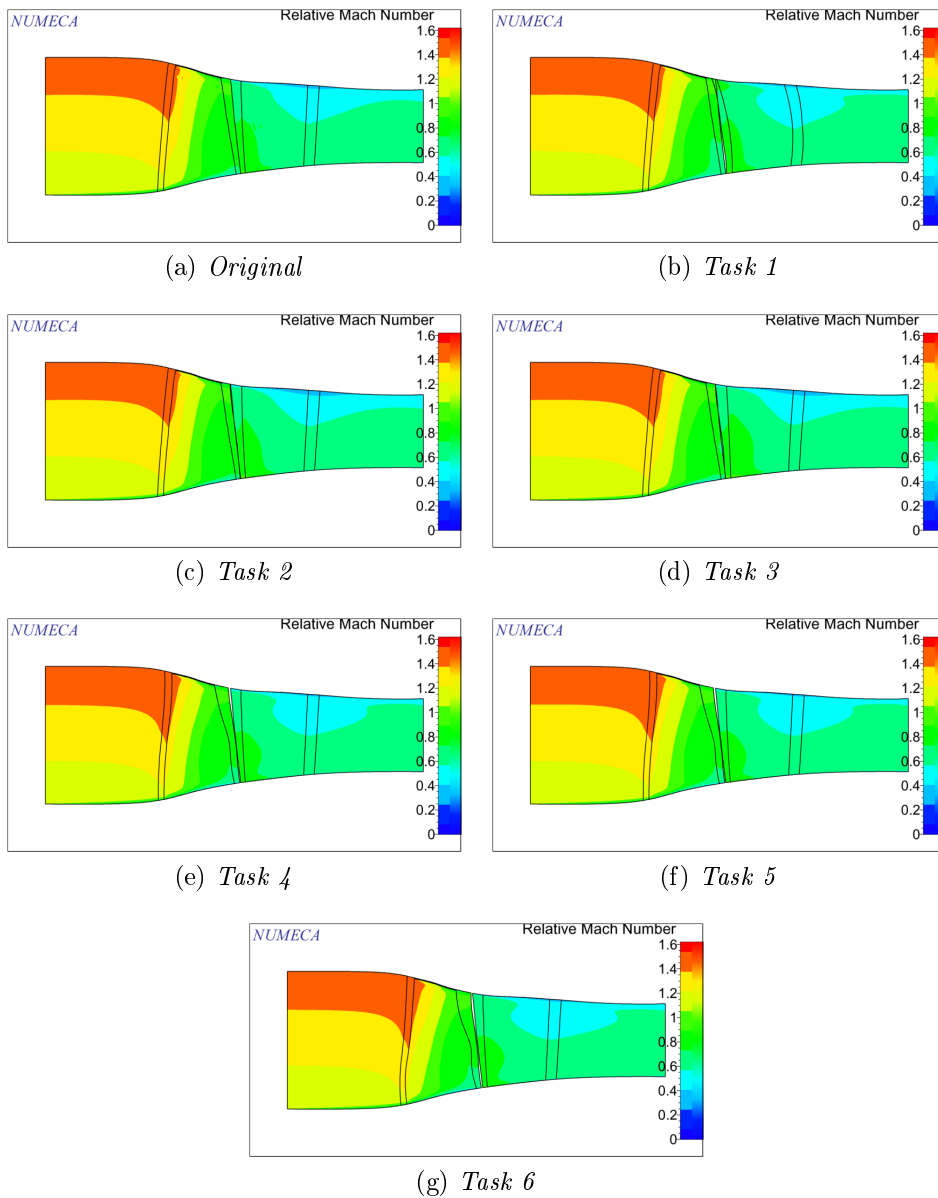
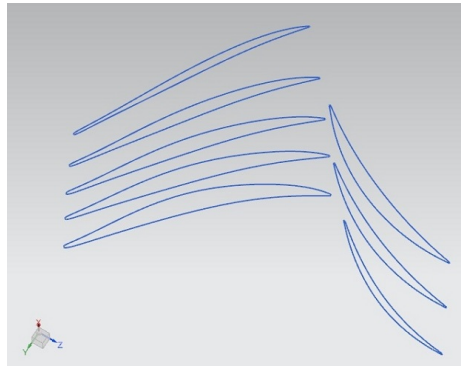
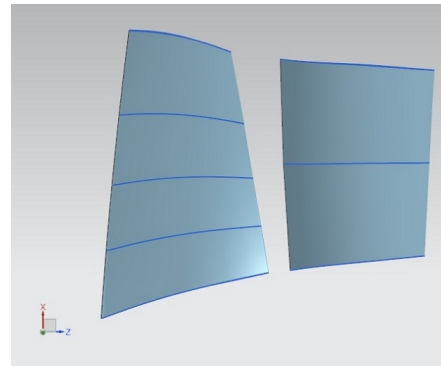


Figure 7.23: Relative Mach

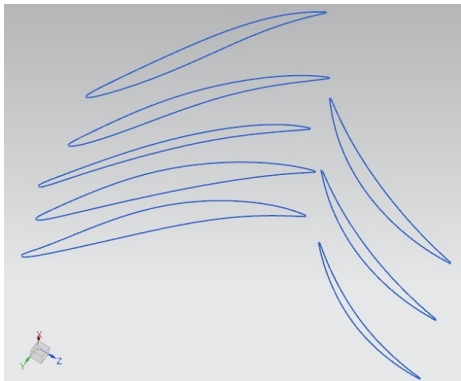
Using NX rotor and stator blade are built and compared.



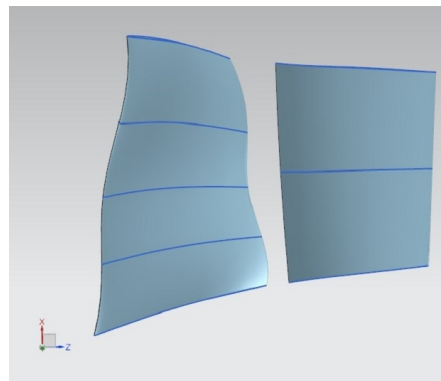
(a) *Original - Profiles*



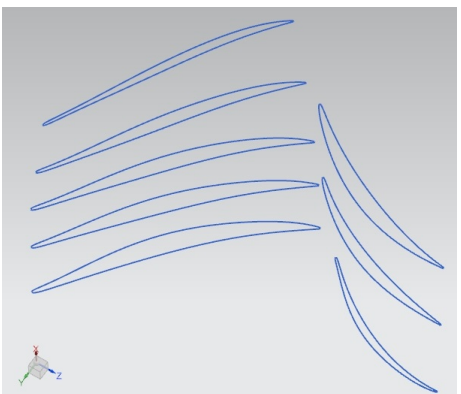
(b) *Original - Blades*



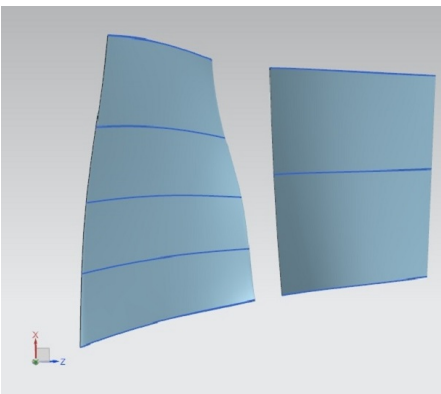
(c) *Task 1 - Profiles*



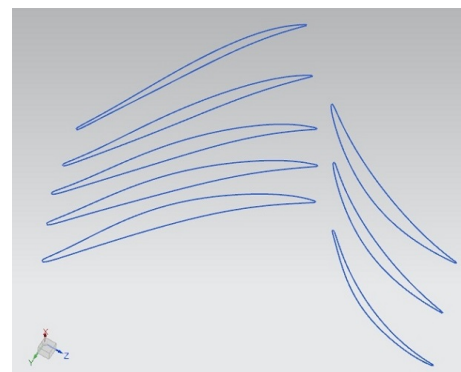
(d) *Task 1 - Blades*



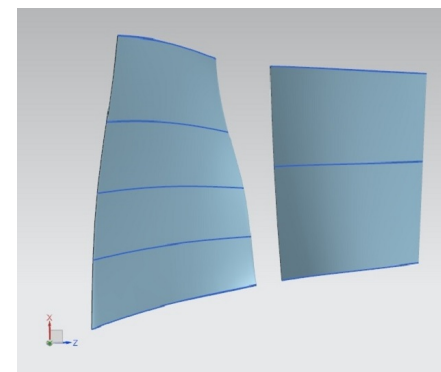
(e) *Task 2 - Profiles*



(f) *Task 2 - Blades*



(g) *Task 3 - Profiles*



(h) *Task 3 - Blades*

Figure 7.24: Rotor and Stator Blades

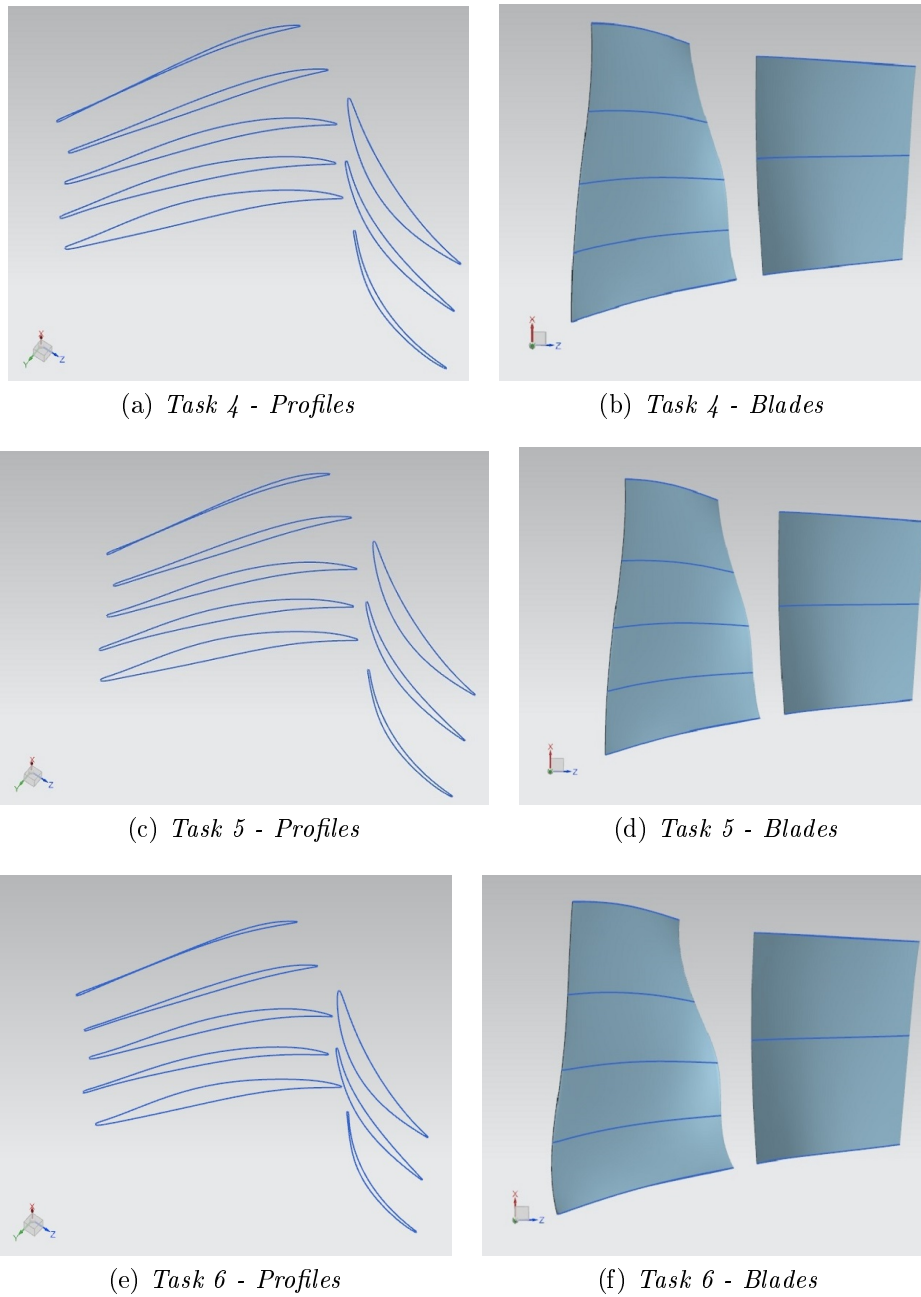


Figure 7.25: Rotor and Stator Blades

The thinner profiles, both for rotor and stator, tend to become thinner and thinner in optimization process. In the original blade, in particular in rotor, profiles leading and trailing edge can be connected with a straight lines; this lines become wavy in the optimization.

# Chapter 8

## Conclusion

The goal of the work has been achieved. In the last task in the working point an efficiency increase of 3.4% is obtained with a mass flow increase of 0.315%, a very small reduction in pressure ratio and an adiabatic efficiency increase.

Both in rotor and stator there is an increase of Mach and Total pressure, respectively relative and absolute; in spite of Turbulent Viscosity tends to decrease.

An aeroelastic analysis is the last step to complete the optimization process of a stage.

The same procedure can be applied to the whole compressor stages [31] and to the turbine stages.

A possible application of this kind of study is to optimized an aircraft engine that has fulfilled its initial mission so that it can be used for driving gas-compressor units or generators. In this way it is possible to keep the parts which are the most expensive in manufacturing, shafts and wheels of compressors [32].

# Bibliography

- [1] Budugur Lakshminarayana - Fluid Dynamics and Heat Transfer of Turbomachinery, John Wiley & Sons, Inc. (1996). p. 70-72.
- [2] Joachim Kurzke - Aero-engine design: from state of the art turbofans towards innovative architectures (2008). p.24.
- [3] Joachim Kurzke - Aero-engine design: from state of the art turbofans towards innovative architectures (2008). p.37-41.
- [4] Agard Advisory Report 355 - CFD Validation for Propulsion System Components (1998). p.4.
- [5] Numeca Online Documentation Platform - FINE/Turbo, Theory Guide, Fluid Models.
- [6] Numeca Online Documentation Platform - FINE/Turbo, Theory Guide, Euler and Navier-Stokes Equations, Navier-Stokes Equations, General Navier-Stokes Equations.
- [7] Numeca Online Documentation Platform - FINE/Turbo, Theory Guide, Euler and Navier-Stokes Equations, Navier-Stokes Equations, Time Averaging of Navier-Stokes Equations.
- [8] Numeca Online Documentation Platform - FINE/Turbo, Theory Guide, Euler and Navier-Stokes Equations, Navier-Stokes Equations, Treatment of Turbulence in the RANS Equations.

- [9] Numeca Online Documentation Platform - FINE/Turbo, Theory Guide, Euler and Navier-Stokes Equations, Navier-Stokes Equations, Formulation in Rotating Frame for the Relative Velocity.
- [10] Numeca Online Documentation Platform - FINE/Turbo, Theory Guide, Boundary Conditions, Inlet Boundary Conditions, Cylindrical Inlet Boundary Conditions.
- [11] Numeca Online Documentation Platform - FINE/Turbo, Theory Guide, Boundary Conditions, Outlet Boundary Conditions, Outlet Boundary Conditions for Subsonic Flow, Pressure imposed.
- [12] Numeca Online Documentation Platform - FINE/Turbo, Theory Guide, Boundary Conditions, Outlet Boundary Conditions, Outlet Boundary Conditions for Subsonic Flow, Mass Flow imposed.
- [13] Numeca Online Documentation Platform - FINE/Turbo, Theory Guide, Boundary Conditions, Solid Wall Boundary Conditions, Navier-Stokes Walls, Adiabatic Walls.
- [14] Numeca Online Documentation Platform - FINE/Turbo, Theory Guide, Numerical Schemes, Discretization and Solution Theory, Spatial Discretization, Viscous Fluxes.
- [15] Numeca Online Documentation Platform - FINE/Turbo, Theory Guide, Numerical Schemes, Discretization and Solution Theory, Spatial Discretization, Inviscid Fluxes.
- [16] Numeca Online Documentation Platform - FINE/Turbo, Theory Guide, Numerical Schemes, Discretization and Solution Theory, Time Discretization Multistage Runge-Kutta.
- [17] <https://www.sharcnet.ca/Software/Fluent6/html/ug/node1011.htm>

- [18] Numeca Online Documentation Platform - FINE/Turbo, Theory Guide, Numerical Schemes, Discretization and Solution Theory, Multigrid Strategy.
- [19] Numeca Online Documentation Platform - FINE/Turbo, Theory Guide, Numerical Schemes, Discretization and Solution Theory, Full Multigrid Strategy.
- [20] Numeca Online Documentation Platform - FINE/Turbo, Theory Guide, Numerical Schemes, Discretization and Solution Theory, Implicit residual smoothing.
- [21] Numeca Online Documentation Platform - FINE/Turbo, Theory Guide, Dedicated Turbomachinery Models, Rotor/Stator Interaction.
- [22] Numeca Online Documentation Platform - FINE/Turbo, Theory Guide, Dedicated Turbomachinery Models, Rotor/Stator Interaction, Full Non-matching Technique for Mixing Planes.
- [23] Numeca Online Documentation Platform - FINE/Turbo, Theory Guide, Turbulence Models, Linear Eddy Viscosity Turbulence Models.
- [24] Numeca Online Documentation Platform - FINE/Turbo, Theory Guide, Turbulence Models, Linear Eddy Viscosity Turbulence Models, Spalart-Allmaras Model
- [25] Stephen B. Pope - Turbulent Flows, Cambridge University Press (2000). p.373-375.
- [26] Numeca Online Documentation Platform - FINE/Turbo, Theory Guide, Turbulence Models, Linear Eddy Viscosity Turbulence Models, k- $\epsilon$  Turbulence Models.
- [27] Degarmo, E. Paul; Black, J. T.; Kohser, Ronald A. (2003), Materials and Processes in Manufacturing (9th ed.), Wiley, p. 119.
- [28] Ansys help. ([http : //www.ansys.stuba.sk/html/lem55/chapter4/ES4 – 185.htm](http://www.ansys.stuba.sk/html/lem55/chapter4/ES4-185.htm)).

- [29] IOSO help, 2016. p.1-2.
- [30] Igor N. Egorov, Gennadiy V. Kretinin, Igor A. Leshchenko - Robust Design Optimization Strategy of IOSO Technology (2002).
- [31] Evgenii Goryachkin, Grigorii Popov, Oleg Baturin, Daria Kolmakova - Three-stage low pressure compressor modernization by means of optimization methods (2015).
- [32] Popov G., Goryachkin E., Kolmakova D., Novikova Y. - Multicriteria optimization of axial low pressure compressor of gas turbine power plant (2016), p-1-2